

Experiments and Comparison of Detonation Cell Size Models for Multi-Fuel Mixtures

In blends of hydrogen, methane, and carbon monoxide

Expériences et comparaison des modèles de taille de cellule de détonation pour les mélanges multicombustibles

Dans les mélanges d'hydrogène, de méthane et de monoxyde de carbone

A Thesis Submitted to the Division of Graduate Studies
of the Royal Military College of Canada
by

Ayush Gupta, BEng, rmc
Second Lieutenant

In Partial Fulfillment of the Requirements for the Degree of
Master of Applied Science in Aeronautical Engineering

May, 2025

© This thesis may be used within the Department of National Defence but
copyright for open publication remains the property of the author.

Abstract

The growing interest in hydrogen and alternative fuel blends for aerospace applications and the decomposition of electric vehicle batteries, comprised primarily of hydrogen, methane and carbon monoxide, necessitates a safety analysis of their detonability. Detonation cell size, a key parameter for physical dimensions influenced by pressure, composition, and temperature, lacks a simple predictive method.

This experimental thesis explores the suitability of existing cell size models against a new set of mixture data comprised of different ratios of hydrogen, methane, and carbon monoxide. The purpose is to determine the extent to which these models can accurately be used to gain a first-order prediction for physical applications of new mixtures. The problem is analyzed by first determining the existing cell size data for multi-fuel blends. Experiments were conducted in a 52 mm diameter cylindrical channel at pressures of 20, 50, 100, and 200 kPa, systematically testing a comprehensive range of multi-fuel mixtures to identify cell size from a sooted foil and compare predictive models. The cell size models of Shchelkin and Troshin [1], Gavrikov *et al.* [2], Ng [3], Bakalis *et al.* [4], and Monnier *et al.* [5], which consider chemical parameters like activation energy, induction length, Mach number, and heat release, are tested against the new dataset. Supplementary experiments are conducted in a newly designed rectangular detonation channel at the Royal Military College of Canada.

The experimental data demonstrate that cell size measurements from a given soot foil exhibit considerable variability, and it is therefore more appropriate to use a distribution-based approach to compare the full range of observed values. While one model is not able to accurately predict the detonation cell size for all tested mixtures and pressures, the study finds that Bakalis *et al.*'s [4] artificial neural network model has the least mean error at 43% and may be accurate enough for first-order estimations of untested mixtures. The study also finds that error increases at higher pressures due to limited data availability for the calibration of parameters.

Résumé

L'intérêt croissant pour l'hydrogène et les mélanges de carburants alternatifs pour les applications aérospatiales et la décomposition des batteries de véhicules électriques, composées principalement d'hydrogène, de méthane et de monoxyde de carbone, nécessitent une analyse de la sécurité de leur détonabilité. La taille de la cellule de détonation ; un paramètre clé pour les dimensions physiques influencées par la pression, la composition et la température, n'a pas de méthode prédictive simple.

Cette thèse expérimentale explore l'adéquation des modèles existants de taille de cellule face à un nouvel ensemble de données de mélanges contenant différentes proportions d'hydrogène, de méthane et de monoxyde de carbone. L'objectif est de déterminer dans quelle mesure ces modèles, non calibrés avec ces mélanges, peuvent fournir une première estimation applicable en physique. Le problème est analysé en identifiant d'abord les données existantes sur la taille des cellules pour les mélanges multi-composantes. Des expériences sont menées dans une conduite cylindrique de 52 mm de diamètre à des pressions de 20, 50, 100 et 200 kPa, testant systématiquement une gamme complète de mélanges afin de mesurer la taille des cellules sur une feuille de suie et de comparer les modèles. Les modèles de taille de cellule de Shchelkin et Troshin [1], Gavrikov *et al.* [2], Ng [3], Bakalis *et al.* [4], et Monnier *et al.* [5], qui tiennent en compte des paramètres chimiques tels que l'énergie d'activation, la longueur d'induction, le nombre de Mach et le dégagement de chaleur, sont testés avec le nouvel ensemble de données. Des expériences complémentaires sont réalisées dans une conduite de détonation rectangulaire conçu au Collège militaire royal du Canada.

Les données expérimentales montrent que les mesures de la taille des cellules à partir d'une feuille de suie donnée présentent une variabilité considérable, et qu'il est donc plus approprié d'utiliser une approche basée sur la distribution pour comparer la gamme complète des valeurs observées. Bien qu'un modèle ne soit pas en mesure de prédire avec précision la taille de la cellule de détonation pour tous les mélanges et pressions testés, l'étude révèle que le modèle de réseau neuronal artificiel de Bakalis *et al.* [4] présente l'erreur moyenne la plus faible à 43% et peut être suffisamment précis pour des estimations de premier ordre de mélanges non testés. Elle met également en évidence une augmentation de l'erreur aux pressions élevées en raison du manque de données disponibles pour la calibration des paramètres.

Acknowledgements

I wish to extend my deepest gratitude to the following people and organizations who contributed to making my educational journey both fulfilling and enjoyable.

I would like to thank my supervisor, Shem Lau-Chapdelaine, for his mentorship, guidance, and support during my studies. I appreciate the inspiration and opportunities he gave me throughout my work to progress as an academic and researcher, and develop skills that will aid me throughout my career.

Un grand merci à Ashwin Chinnayya, Vincent Rodriguez et Alexandre Poyet, qui m'ont chaleureusement accueilli à l'École nationale supérieure de mécanique et d'aérotechnique de Poitiers, en France. Leur invitation à collaborer dans leur laboratoire a été une expérience extrêmement enrichissante, et leur soutien constant a été précieux pour faire avancer ma recherche. Leur accueil, leur bienveillance et leur esprit de collaboration ont grandement contribué à la réussite de ce projet, et je leur suis profondément reconnaissant.

I would like to extend my sincere appreciation to the technical staff of the Chemistry and Chemical Engineering, and Mechanical and Aerospace Engineering departments for their invaluable assistance in the development of the RMC Detonation Laboratory. Their expertise, dedication, and hands-on support were instrumental in bringing this facility to life, and their contributions have greatly enhanced the scope of this research.

Special thanks go to my fellow students and professors in the Queen's University–Royal Military College joint research group on detonations. Their expertise, experience, and support helped to broaden my understanding and expand my horizons. I will forever cherish the new friendships formed here.

I owe my successes to the esteemed institutions of the Royal Military College of Canada and the Canadian Armed Forces, whose unwavering support and commitment to lifelong learning have been the cornerstone of my journey. Their dedication to excellence, duty, and leadership empowered me to pursue higher education and shaped the path of my personal and professional growth. I am also profoundly grateful for the incredible friends I have made in my professional career so far, whose shared dedication and sense of purpose have made this journey all the more meaningful.

Finally, I want to thank my family and friends for their unwavering support and belief in me. Their constant encouragement, understanding, and love have been a source of strength, and I am truly grateful to have them by my side as I pursue my ambitions.

The work was funded and supported by Defence Research and Development Canada, the Department of National Defence, and the Natural Sciences and Engineering Research Council of Canada.

Contents

1	Introduction	1
1.1	Background and Motivation	1
1.2	Current Study	7
2	Modeling Background and Details	9
2.1	Detonation Cell Size	9
2.1.1	Factors Affecting Cell Size	11
2.2	Cell Size Models	13
2.2.1	Shchelkin and Troshin (1964) [1]	13
2.2.2	Gavrikov <i>et al.</i> (2000) [2]	13
2.2.3	Ng (2005) [3]	15
2.2.4	Monnier <i>et al.</i> (2023) [5]	16
2.2.5	Bakalis <i>et al.</i> (2023) [4]	18
2.2.6	Other Models Considered	19
3	Experimental Methodology	21
3.1	ENSMA Detonation Channel	21
3.2	RMC Detonation Channel	24
3.3	Detonation Cell Size Measurements	26

3.3.1	Cell Size Statistics	26
3.3.2	Cell Size Measurement Variability	35
4	Results	40
4.1	ENSMA Detonation Channel	40
4.2	RMC Detonation Channel	43
5	Discussion	46
5.1	Experimental Results	46
5.1.1	Kinetic and Thermodynamic Calculations	46
5.1.2	Pressure and Mixture Trends	48
5.1.3	Cell Size Measurement Distribution	52
5.2	Experimental Data Model Comparison	55
5.2.1	Extending Model Comparison to Literature Data	66
5.2.2	Future Work in Statistical Detonation Cell Size Modelling	69
5.3	RMC Detonation Channel	69
6	Conclusions	71
7	Recommendations	73
	References	75
A	Experimental and Literature Data	85
B	RMC Detonation Laboratory	95
B.1	Detonation Channel and Frame	95
B.2	Mixing Panel and Gas Handling	99
B.3	Procedure Checklists	101

List of Figures

1.1	Schematic of production of a detonation cell from a detonation front	3
1.2	Example trace of cells on a soot foil of a $2\text{H}_2 + \text{O}_2 + 3.76\text{N}_2$ detonation at $P_1 = 100 \text{ kPa}$ and $T_1 = 292 \text{ K}$. Detonation propagates left to right.	3
1.3	Diagram of a CJ detonation leaving a pipe into unconfined space, top shows for diameter less than critical, bottom is diameter greater than critical. . .	4
1.4	Experimental cell size measurements for multi-fuel mixtures at all initial P_1 and T_1 from data in Appendix A overlaid on alternative fuel applications comprised of H_2 , CO , and CH_4 with stoichiometric O_2 ; bold numbers correspond to mix labels for present study in Table 3.1.	8
2.1	Schematic of ZND detonation temperature, pressure, and density profile for CJ detonation	10
2.2	Experimental cell width versus initial mixture pressure for stoichiometric hydrogen-oxygen and stoichiometric methane-oxygen, and binary fuel hydrogen-methane-oxygen at different equivalence ratios, and room temperature . . .	12
3.1	Experimental setup of cylindrical detonation channel at ENSMA.	21
3.2	Pressure transducer and shock pin traces for $0.083 \text{ H}_2 + 0.250 \text{ CH}_4 + 0.083 \text{ CO} + 0.583 \text{ O}_2$ (Mix 1) at $P_1 = 50 \text{ kPa}$. Lines correspond to pressure transducers at locations shown in Fig. 3.1.	23
3.3	Comparison of calculated CJ velocity using SDToolBox [61] to experimental average detonation velocities. Pink band indicates $\pm 2\%$ error.	24
3.4	Experimental setup of rectangular detonation channel at RMC	25

3.5	Soot foil with measurement traces for CJ detonation in cylindrical channel for $0.083 \text{ H}_2 + 0.250 \text{ CH}_4 + 0.083 \text{ CO} + 0.583 \text{ O}_2$ (Mix 1) at $P_1 = 49.99 \text{ kPa}$, $T_1 = 18.1 \text{ C}$. Detonation propagates left to right.	27
3.6	Density histogram of experimental cell size measurements and probability density functions for various distributions for $0.083 \text{ H}_2 + 0.250 \text{ CH}_4 + 0.083 \text{ CO} + 0.583 \text{ O}_2$ (Mix 1) at $P_1 = 50 \text{ kPa}$	27
3.7	Original and clipped frequency histogram to remove outliers exceeding $1.5 \times IQR$ and using 10 bins for $0.222 \text{ CH}_4 + 0.222 \text{ CO} + 0.555 \text{ O}_2$ (Mix 7), $P_1 = 100 \text{ kPa}$	30
3.8	Density histogram of experimental cell size measurements and probability density functions for various distributions for $0.333 \text{ H}_2 + 0.111 \text{ CH}_4 + 0.111 \text{ CO} + 0.444 \text{ O}_2$ (Mix 3) at $P_1 = 100 \text{ kPa}$	32
3.9	Relative frequency histogram of differential cell size of two independent measurements by A. Gupta (blue) and A. Poyet (orange) , overlap shown in grey.	36
3.10	Bland-Altman plot comparing average cell size of two independent experimental measurements of A. Gupta and A. Poyet	38
4.1	Soot foil images for CJ detonation in cylindrical channel for $0.083 \text{ H}_2 + 0.250 \text{ CH}_4 + 0.083 \text{ CO} + 0.583 \text{ O}_2$ (Mix 1) at $P_1 = 20.03 \text{ kPa}$, $T_1 = 17.4 \text{ C}$ (top), $0.083 \text{ H}_2 + 0.250 \text{ CH}_4 + 0.083 \text{ CO} + 0.583 \text{ O}_2$ (Mix 1) ($P_1 = 49.90 \text{ kPa}$, $T_1 = 17.2 \text{ C}$) (bottom left); $0.095 \text{ H}_2 + 0.190 \text{ CH}_4 + 0.190 \text{ CO} + 0.524 \text{ O}_2$ (Mix 6) at $P_1 = 20.0 \text{ kPa}$, $T_1 = 18.0 \text{ C}$ (bottom right). Detonation propagates left to right.	41
4.2	Average cell width and histograms showing the relative frequency of cell size measurements (red line is mean, orange is median)	42
4.3	Cell width and detonation velocity of stoichiometric hydrogen/oxygen tests at RMC	44
4.4	Pressure transducer traces for 15 kPa test of $2\text{H}_2 + \text{O}_2$ at RMC rectangular detonation channel. Traces correspond to pressure transducers at locations shown in Fig. 3.4.	44
4.5	Soot foil images for CJ detonation in rectangular RMC channel for stoichiometric hydrogen/oxygen at $P_1 = 14.99 \text{ kPa}$, $T_1 = 20.3 \text{ C}$ (left); $P_1 = 12.52 \text{ kPa}$, $T_1 = 18.5 \text{ C}$ (right). Detonation propagates left to right.	45
5.1	Cell width variation with changing fuel fraction of ternary fuel mixture and pressure for (a) $X_{f,\text{H}_2} = 0.2$ (top) and (b) $X_{f,\text{CH}_4} = 0.2$ (bottom)	50

5.2	Cell width variation with changing fuel fraction of binary CO-CH ₄ mixture at different pressures	52
5.3	ZND temperature profiles for sample mixtures of 2H ₂ +O ₂ , Mix 1, 3, and 5 at $P_1 = 20$ kPa and $P_1 = 200$ kPa, $T_1 = 293$ K using San Diego mechanism [102].	54
5.4	Ternary plot of Δ_i contours using San Diego mechanism [102] and averaged λ/Δ_i (notated numbers) of stoichiometric, undiluted methane, hydrogen, carbon monoxide fuel blends at $P_1=100$ kPa	56
5.5	Correlation between experimental cell width and calculated induction length using San Diego mechanism [102], with line of $\lambda = 20.8\Delta_i$	57
5.6	Relative frequency of percent error of average cell size by model for all experimental test mixtures	58
5.7	Box plot of model accuracy to experimental results by pressure	60
5.8	Distribution of number of cell size measurement tests by initial test pressure for all data in literature and this study, for mixtures comprised of hydrogen, methane, and carbon monoxide with oxygen (Appendix A).	61
5.9	Relative error box plots of experimental measurements for ternary fuel mixtures compared to prediction cell models of 1. Gavrikov <i>et al.</i> [2], 2. Ng [3], 3. Bakalis <i>et al.</i> [4], 4. Monnier <i>et al.</i> [5], $\lambda/\Delta_i = 20.8$ [1]	64
5.10	Relative frequency of percent error by model for all test and literature binary and ternary mixtures comprised of hydrogen, methane, and carbon monoxide	67
5.11	Box plot of model accuracy to experimental and published binary and ternary mixtures comprised of hydrogen, methane, and carbon monoxide by pressure	68
5.12	Initial pressure vs cell width for stoichiometric hydrogen-oxygen mixtures, including literature data and preliminary RMC channel data	70
B.1	CAD model of detonation channel at RMC	96
B.2	CAD model of frame section for detonation channel	97
B.3	CAD model of caddy for detonation channel	98
B.4	Solidworks FEA simulation of RMC detonation channel section with maximum internal loading representing a reflected CJ shock pressure of 3 MPa. .	99
B.5	Mixing panel schematic for RMC detonation channel	100

List of Tables

2.1	Dimensionless coefficients and exponent of the Gavrikov <i>et al.</i> model equation [2]	15
2.2	Dimensionless coefficients of the Ng [3] model equation with $N = 3$	16
3.1	Composition by mole fraction of binary and ternary mixtures tested	22
3.2	Pressure transducer and shock pin results for 0.083 H ₂ +0.250 CH ₄ +0.083 CO+0.583 O ₂ (Mix 1) at $P_1=50$ kPa, calculation of detonation velocity.	24
3.3	χ^2 goodness-of-fit test for measured experimental cell size histograms compared to statistical distributions. Bolded values indicate significant $p\text{-val} \geq 0.05$	31
3.4	Quantitative histogram statistics for the multifuel experimental mixtures from Table 4.2 for a logarithmic normal distribution.	34
3.5	Statistical measurements for percentage difference of average cell size measurements by two researchers	38
4.1	Pressure transducer results for 2H ₂ + O ₂ at $P_1=15$ kPa, calculation of detonation velocity.	45
5.1	$\frac{E_a}{RT_{vN}}$ calculated for experimental mixtures and pressures	47
5.2	D_{CJ} [m/s] calculated for experimental mixtures and pressures	47
5.3	ZND induction length using San Diego mechanism [102] for experimental mixtures and pressures, Δ_i [mm]	48
5.4	Correlations for mixture trends with pressure and cell width following the equation $\lambda = aP_1^b$ for experimental mixtures tested	48

5.5 Statistical correlations between experimental ternary cell widths and prediction models 62

A.1 Cell width and detonation velocity data for experimental results of this study and literature data for mixtures comprised of H₂, CH₄, CO [76] 85

Nomenclature

a	Scaling factor	mm/Pa
c	Speed of sound	m/s
d	Diameter	m
df	Degrees of freedom	-
g_i	Gavrikov <i>et al.</i> model coefficients and exponent	-
h	Enthalpy	J/mol
i	Counter	-
k	Reaction rate pre-exponential factor	s ⁻¹
l	Length	m
n	Number of histogram bins	-
p	Statistical p-value	-
r	Gamma distribution shape parameter	-
t	Time	s
u	Velocity	m/s
w_i	Ng model coefficients	-
x	Displacement	m
y	Burn ratio for Monnier <i>et al.</i> model	-
z	Distance from shock	m
z_i	Ng model coefficients	-
A	Constant of proportionality	-
C_p	Specific heat capacity (constant pressure)	J kg ⁻¹ K ⁻¹

C_v	Specific heat capacity (constant volume)	$\text{J kg}^{-1}\text{K}^{-1}$
D	Detonation velocity	m/s
E_a	Activation energy	J/mol
E	Expected frequency of data	-
ERC	Error range coverage	-
G_i	Factors for Gavrikov <i>et al.</i> model	-
I	Indicator function	-
IQR	Interquartile range	m
K	Arrhenius reaction pre-exponential factor	-
L	Cell length (longitudinal)	m
LW	Lower whisker	m
M	Mach number	-
MRE	Mean relative error	-
N	Number of samples	-
O	Observed frequency of data	-
P	Pressure	Pa
Q	Heat release	J
Q_i	Quartile	m
R	Ideal gas constant	$\text{J mol}^{-1}\text{K}^{-1}$
$RMSRE$	Root mean squared relative error	-
T	Temperature	K
UW	Upper whisker	m
W_0	Ng model coefficient	-
X	Mole fraction	-
Y	Species fraction	-
Z	Standard normal variable	-
β	Weibull distribution shape parameter	-
χ	Stability parameter in Ng model	-

χ^2	Chi-squared statistical test	-
δ	Weibull distribution scale parameter	-
$\Delta\lambda$	Measurement difference	m
Δ_i	Induction zone length	m
Δ_r	Reaction zone length	m
$\dot{\omega}$	Arrhenius rate law	$\text{kg m}^{-3}\text{s}^{-1}$
$\dot{\sigma}$	Thermicity	s^{-1}
ϵ	Distribution function	-
γ	Ratio of specific heats	-
λ	Cell width	m
μ	Mean	m
ν	Specific volume	m^3/kg
ϕ	Equivalence ratio	-
ψ	Distribution function	-
ρ	Density	kg/m^3
σ	Standard deviation	m
σ^2	Variance	m^2
τ_i	Ignition delay	s
ξ	Exponential distribution rate parameter	-
ζ	Gamma distribution rate parameter	-

Acronyms

AFRL	Air Force Research Laboratory
ANN	Artificial neural network
CAD	Computer-aided design
CDF	Cumulative distribution function
CJ	Chapman-Jouguet
CNRS	Centre national de la recherche scientifique
DDT	Deflagration-to-detonation transition

ENSMA	École Nationale Supérieure de Mécanique et d'Aérotechnique
FEA	Finite element analysis
GAP	Glycidyl azide polymer
HENG	Hydrogen-enriched natural gas
ID	Inner diameter
ISO	International Organization for Standardization
ODE	Ordinary differential equations
OD	Outer diameter
PDF	Probability distribution function
RDE	Rotating detonation engine
RMC	Royal Military College of Canada
SDToolbox	Shock & Detonation Toolbox (CalTech)
SFRJ	Solid-fuel ramjet
vN	von Neumann
WHMIS	Workplace hazardous materials information system
ZND	Zeldovich–von Neumann–Döring

Subscripts

1	Initial state
c	Critical
f	Fuel
i	Induction
m	Mean
p	Products
r	Reactants

Superscripts

b	Scaling exponent
-----	------------------

-

Chapter 1

Introduction

1.1 Background and Motivation

With the growing demand for energy in the modern world, focus has been placed on developing renewable energy sources that can support transportation networks and power grids. In Canada, the aviation, rail, marine, and heavy trucking industries—along with the federal government—are increasingly investing in alternative fuels as transitional solutions to reduce carbon emissions, while hydrogen technologies continue to mature. These sectors face high energy demands and limited short-term electrification options, making low-carbon fuels a critical interim step toward decarbonization. By 2050, the global market value for hydrogen is expected to reach \$11.7 trillion [6]. Some alternative fuel mixtures of interest are hydrogen-enriched natural gas (HENG) [7], [8], synthesis gas [9], biogas [10], wood gas, coal gas [11], and the anaerobic decomposition of polymers or energetic materials and battery fires [12], [13], all of which are primarily blends of hydrogen, methane, carbon monoxide, and carbon dioxide. While most industrial applications in transportation, heating, and energy focus on deflagrative combustion, when these gas mixtures are combined with air at favourable temperatures, pressures, and equivalence ratio, they could detonate.

Given the potential for detonation in industrial safety applications, understanding the fundamental differences between deflagration and detonation is crucial. Deflagration is a subsonic combustion process where the reaction front propagates through thermal and molecular diffusion. This process relies on the transfer of heat and radical species from the burned to the unburned fuel, allowing a flame to propagate. The reaction zone in a deflagration is relatively broad, and the resulting pressure waves are weak, meaning that disturbances can propagate upstream, affecting the flame dynamics. In contrast, detonation is a supersonic combustion wave that propagates due to a leading shock front, which adiabatically compresses the reactants preceding a reaction zone where the exothermic chemical reactions occur [14]. The shock wave and chemical reaction zone are closely coupled, leading to a self-sustaining wave that does not require external heat transfer for

propagation. The onset of detonation can occur through direct initiation, where an external energy source directly generates a detonation wave; however, in most practical scenarios, detonation occurs via deflagration-to-detonation transition (DDT). During DDT, a flame front accelerates due to instabilities and pressure interactions, reaching supersonic speeds relative to the unburned reactants. Local regions of the mixture experience rapid compression and autoignition, forming localized explosion centres in the reaction zones. Eventually, these explosion centres coalesce, generating a self-sustaining detonation wave. The process is often observed in confined geometries, such as tubes or channels, where shock reflections and turbulent flame acceleration promote transition to detonation [14].

Experimental evidence shows that the spontaneous development of cellular structures, driven by instabilities, is essential for sustaining detonations by enabling ignition and rapid combustion within the reaction zone [14]. The formation of a detonation cell arises from the dynamic interactions between the leading shock front, transverse waves, and the exothermic chemical reaction zone. The three-dimensional detonation front is not planar, it has some portions that travel faster than others. A diagram of the wave interactions is shown in Fig. 1.1. In this simplified diagram, consider the detonation propagating left to right at velocity D shown in two instances in time. At t_1 , the shock front is formed by a curved shock called a Mach stem, connected by vertical incident shocks. Transverse waves are seen at the intersection of the incident shock and Mach stem, which travel perpendicular to the direction of propagation of the detonation leading shock front. The point where these three shocks meet is referred to as a triple point. Pairs of triple points travel along the detonation front towards each other as the shock front and transverse waves propagate, and upon intersection, they reflect, forming a new Mach stem. The triple points trace paths towards each other with one moving up and the other moving down, until reflection where the new triple points move away from each other; this cycle is repeated resulting in the cellular structure seen in Fig. 1.1. These triple point trajectories can be recorded on a metal foil with smoke soot deposited (soot foil) resulting in a fish-scale-like pattern, as first demonstrated by Denisov and Troshin [15]. The detonation cell size (λ), given as the width of these cells, is a fundamental parameter that is used to characterize a mixture's reactivity. The cell width can be determined by physical measurement on a sooted foil. To better visualize this process, cells may be traced as shown in Fig. 1.2.

The detonation cell size is related to critical physical dimensions including tube design for industrial safety and aerospace propulsion applications, making it important to study. Mitrofanov and Soloukhin [16] and Moen *et al.* [17] showed that for most mixtures which result in irregular cell patterns, the critical tube diameter is $d_c = 13 \lambda$, below which a detonation leaving the tube into unconfined space fails. This limit increases to vary between 20 and 30 for more regular mixtures like acetylene-oxygen [18], [19]. As seen in Fig. 1.3, the critical tube diameter is the minimum diameter through which a planar detonation can emerge into open space and continue to propagate as a spherical detonation [14]. Below this limit, the shock and flame leaving the pipe at the Chapman-Jouguet (CJ) velocity become decoupled in the open space and the detonation velocity reduces as the detonation fails. As the detonation fails, a spherical deflagration is observed and the effects are less damaging. For tubes greater than the critical tube diameter, the planar detonation evolves into a

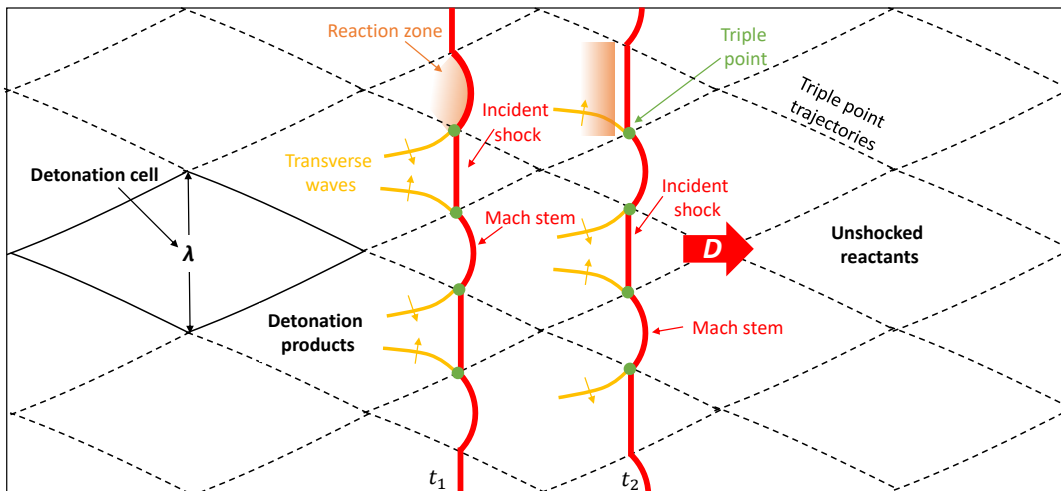


Figure 1.1 – Schematic of production of a detonation cell from a detonation front

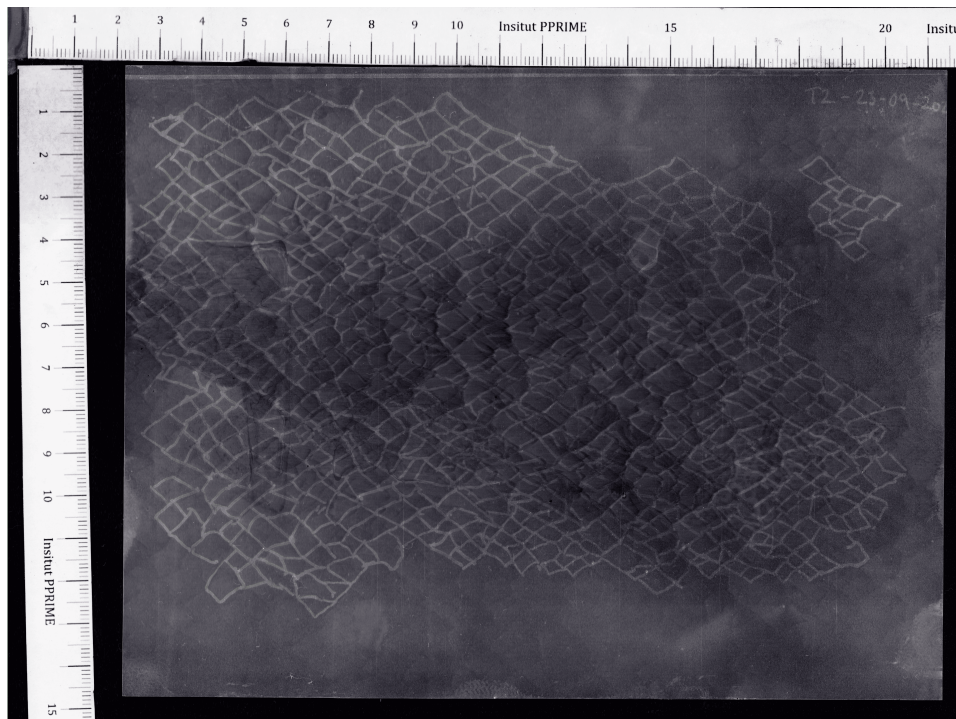


Figure 1.2 – Example trace of cells on a soot foil of a $2\text{H}_2 + \text{O}_2 + 3.76\text{N}_2$ detonation at $P_1 = 100\text{ kPa}$ and $T_1 = 292\text{ K}$. Detonation propagates left to right.

spherical detonation after leaving the tube. As the detonation leaves the tube, expansion waves with steep pressure gradients are generated at the exit which quench the detonation near the edges as it emerges into unconfined space. The pressure gradient of the expansion is less steep along the axis of the tube and the shock and flame remain closely coupled. This closely coupled shock and flame propagate along the spherical detonation and reinitiate the edges, resulting in a self-sustaining cellular detonation in the unconfined space which can be extremely destructive. This concept is paramount to industrial safety applications and thus the cell size for reactive mixtures must be known to ensure a catastrophic detonation is not carried into an open space.

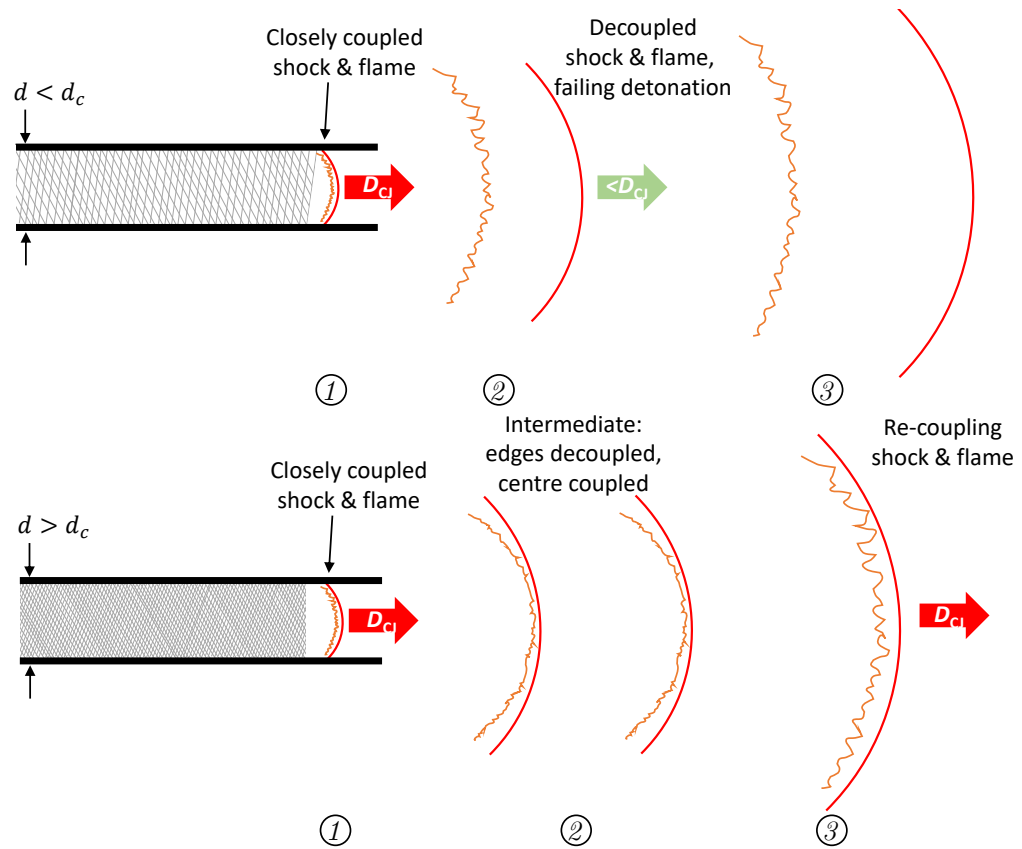


Figure 1.3 – Diagram of a CJ detonation leaving a pipe into unconfined space, top shows for diameter less than critical, bottom is diameter greater than critical.

An initiative in curtailing carbon emissions in the aerospace sector is with the rotating detonation engine (RDE) which attempts to harness the detonations for pressure-gain combustion [20]–[22]. The RDE operates on the principle of continuous detonation, where one or more detonation waves perpetually travel around the circumference of an annular combustion chamber. Fuel and oxidizer are injected into the head of this chamber, and upon ignition, the detonation wave consumes the mixture, producing high-pressure and high-temperature gases that are expelled axially to generate thrust. This method contrasts

with traditional engines that rely on deflagrative combustion.

These engines are expected to have several advantages including: a shorter overall engine length with the elimination of a compressor and turbine leading to lower engine mass [23], single-time ignition at start up improving reliability, and the ability to run off alternative fuels [20], all of which could introduce many benefits in the payload and range capabilities of aerospace vehicles while reducing environmental impact.

Nicholls [24] was a pioneer in the RDE by introducing the theoretical concept of intermittent detonations being used to generate thrust in 1953. Around the same time, he introduced a conceptualized device where the detonation would continuously rotate, dubbed the Continuous Rotating Detonation Engine. The first implementation of continuous detonation combustion in an annular chamber was demonstrated by Voytsekhovskiy [25] who showed that a continuous detonation could be stabilized in a circular channel. Nicholls *et al.* [26], [27] also ran experiments using gaseous hydrogen-oxygen and methane-oxygen, and although they could not get the engine to run continuously, a single CJ wave was realized for the first cycle of the engine showing its feasibility. Later, Bykovskii and Mitrofanov [28], and Bykovskii and Vedernikov [29] performed experimental studies on the stability of the rotating detonation wave with various injection methods, chamber designs, and fuels including methane, propane, acetylene, and hydrogen with oxygen. More recent progress in RDE development in the 2000s was summarized by Kailasanath [21]. Most notably, significant progress has been made by the United States' Air Force Research Laboratory (AFRL) [20], [30], [31] and France's Centre national de la recherche scientifique (CNRS) [32]. AFRL has conducted tests on various combustion chamber sizes, fuels, and nozzle configurations to study the specific impulse, fuel consumption, and thrust. For these tests, AFRL used hydrogen-air and ethylene-air gaseous fuels, and they showed comparable performance to pulsed detonation engines. When coupled with a turbine and compressor, the turbine engine with an RDE-replaced combustion chamber shows a similar power output to a conventional gas turbine [20]. French research has focused on the development of RDEs for high-speed applications, in particular a collaboration with MBDA for a supersonic multi-role strike weapon, with foundational research supported by CNRS Poitiers [21].

To date, most RDE research uses liquid and gaseous fuels and oxidizers, which can be difficult to transport and store in austere military environments. Few studies relate to high-energy density solid-fuels and energetic polymers in RDEs, which lend themselves safer to transport and storage. Bykovskii *et al.* [33]–[35] tested the continuous detonation of coal-hydrogen-air mixtures and Wu *et al.* [36] tested black powder, which decomposes to a mixture of hydrogen, nitrogen, carbon monoxide, hydrogen chloride and trace amounts of methane and carbon dioxide. However, these fuels still require hydrogen gas to sustain the rotating detonation wave. Xu *et al.* [37], [38] recently tested an aluminum powder air-breathing RDE showing it generated higher thrust than an equivalent hydrogen-air RDE. The viability of these fuels is dependent on their detonation characteristics. In a similar vein, research is being done on solid-fuel ramjets (SFRJ) for munition propulsion applications. A study by Yogeshkumar *et al.* [39] considered fuel-rich propellants consisting of aluminum, ammonium perchlorate, and hydroxyl-terminated polybutadiene for SFRJ

applications in 155 mm artillery shells. They also considered other propellants including glycidyl azide polymer (GAP) which was studied for ducted rocket application [40] and has known decomposition products composed of nitrogen, hydrogen, methane, carbon monoxide, and traces of ethylene, ethane, carbon dioxide, and acetylene [41]. Given the diversity of alternative fuels under consideration, it is essential to establish a relationship between experimental detonation characteristics and fuel suitability for use in Rotating Detonation Engines (RDEs). Moreover, RDEs are expected to operate at elevated initial pressures, which makes it important to consider detonation cell size at different pressures. Bykovskii *et al.* [42] proposed a general correlation for RDE operability, suggesting a minimum diameter of $\sim 40\lambda$. While other experimental indicators, such as low-pressure detonability limits or high-pressure test limits in small-diameter tubes, may offer additional insight into detonation behavior, they lack similarly established quantitative criteria. Thus, despite its limitations, cell size remains the most directly applicable metric for preliminary RDE feasibility assessments.

More recently, the increasing popularity of electrification of transportation infrastructure has garnered unprecedented interest in batteries. Recent studies evaluate the anaerobic decomposition of lithium-ion batteries causing thermal runaway fires [12], [13], [43], [44]. Studies determine that this thermal runaway of commercially available battery types result in concentrations of 5-30% H₂, 5-30% CO, 20-90% CO₂, and 0-9% of various hydrocarbons [44], where concentration is dependent on the state of charge. These reactive byproducts are similar to the alternative fuels of interest and can detonate causing significant implications in industrial safety. These batteries and alternative fuel sources have increasing applications in electric vehicles and aircraft development and further decarbonization efforts must consider the industrial safety for transportation of hazardous batteries. Characterizing the detonation cell size of thermal runaway decomposition products enables a more precise assessment of safety risks associated with the transport and storage of batteries, particularly in scenarios where detonation is a potential hazard.

The existing literature has extensive work towards experimental measurements of cell size for sub-atmospheric pressures, room temperature, and mixtures comprised of only one fuel and oxidizer (single-fuel mixtures). At present, there is limited research in mixtures with more than one fuel with oxidizer (multi-fuel mixtures), especially at atmospheric and super-atmospheric pressures, despite their prevalence in industrial pipeline applications and RDEs. More importantly, there is no existing model which has been specifically developed to predict the detonation cell size of these proposed alternative fuel sources, and cell sizes for previously untested mixtures are typically determined through experiments. Notably, the wide range of fuels discussed require extensive testing and it is preferred to obtain an estimate for safety and energy applications. Therefore, the present thesis attempts to answer the important question: *To what extent can existing cell size models accurately predict multi-fuel detonation cell size?*

1.2 Current Study

Previous research has demonstrated that several factors affect cell size, yet no definite model is able to predict a detonation cell size from initial conditions. Existing models have been tuned to specific mixtures and require experimental data to complement the fitted parameters. The growing need for renewable and alternate fuels for safety and RDE propulsion requires estimations of detonation cell sizes to propose physical dimensions. Fig. 1.4 is a ternary plot which illustrates the experimental cell size measurements and alternative fuels of interest of mixtures comprised of varying fuel fractions of hydrogen, methane, and carbon monoxide. The plot shows single fuel detonation cell size experiments at the corners, binary fuel experiments along the edges, and ternary fuel mixture experiments in the middle region, where the fuel fractions are indicated by the values on the axes, all reacted stoichiometrically with oxygen only. The filled regions show the range of fuel composition for the alternative fuels of interest. In cases where the alternative fuel has more than just CO, H₂, and CH₄, the ratio of each of these three species is calculated relative to just their combined total, ignoring the other fuels for the ternary plot comparison. Fig. 1.4 shows most existing literature cell size data points at the corners and edges, suggesting a lack of research in ternary blends reacted with oxygen.

The present study uses an experimental approach to test multi-fuel blends at a range of pressures and determine the cell size. The thesis work includes using a detonation channel at École Nationale Supérieure de Mécanique et d'Aérotechnique (ENSMA) in Poitiers, France which could conduct experiments at initial pressures of up to 200 kPa, allowing experimental cell sizes to be measured at expected operating ranges for an RDE or industrial safety application. In parallel, the work required the development and construction of the detonation channel at the Royal Military College of Canada (RMC) in Kingston. The accuracy of existing cell size prediction models is assessed statistically against the experimental data of this study to evaluate their performance on new mixture data. This data is then compiled with existing literature data to reveal the overall agreeance of models with cell size experimental data.

The present thesis is organized as follows. Chapter 2 presents a brief summary of the factors affecting detonation cell sizes, and discussion of cell size models. Chapter 3 presents the experimental setup used at ENSMA, and detailed procedures and development of the RMC detonation channel. Chapter 4 details the experimental results obtained from the multi-fuel mixtures tested. In Chapter 5, these results are compared to existing cell size models, with a discussion on how the models' predictions vary with pressure and mixture.

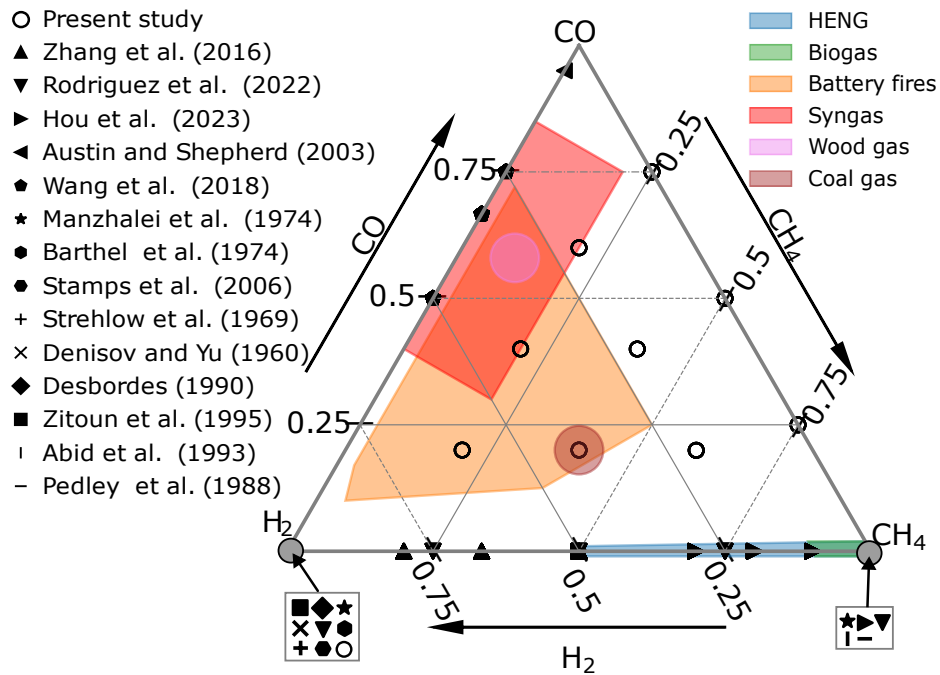


Figure 1.4 – Experimental cell size measurements for multi-fuel mixtures at all initial P_1 and T_1 from data in Appendix A overlaid on alternative fuel applications comprised of H_2 , CO , and CH_4 with stoichiometric O_2 ; bold numbers correspond to mix labels for present study in Table 3.1. References: Zhang *et al.* (2016) [45], Rodriguez *et al.* (2022) [46], Hou *et al.* (2023) [47], Austin and Shepherd (2003) [48], Wang *et al.* (2018) [49], Barthel *et al.* (1974) [50], Stamps *et al.* (2006) [51], Strehlow *et al.* (1969) [52], Denisov and Yu (1960) [53], Desbordes (1990) [54], Zitoun *et al.* (1995) [55], Abid *et al.* (1993) [56], Pedley *et al.* (1988) [57].

Chapter 2

Modeling Background and Details

2.1 Detonation Cell Size

To describe the behavior of a fully developed detonation, classical gas dynamic models provide fundamental insights. The CJ theory describes the steady-state detonation condition, where the post-detonation flow speed is exactly sonic. This means that no pressure disturbances can propagate upstream to affect the leading shock, making the CJ detonation self-sustaining. However, the CJ model does not account for the internal structure of the detonation wave.

A more detailed description is provided by the Zeldovich–von Neumann–Döring (ZND) model [58]–[60], which integrates ordinary differential equations that describe the steady, one-dimensional structure of a detonation wave (Fig. 2.1). The mass, momentum, energy, and species conservation equations for a coordinate system fixed to the detonation wave are [14], [61]

$$\begin{aligned}\frac{d}{dx}(\rho u) &= 0 \\ \frac{d}{dx}(P + \rho u^2) &= 0 \\ \frac{d}{dx}\left(h + \frac{u^2}{2}\right) &= 0 \\ \frac{dY_i}{dx} &= \frac{\dot{\omega}_i}{\rho u}\end{aligned}\tag{2.1}$$

where $\dot{\omega}_i$ is typically assumed to follow an Arrhenius reaction rate law. The equation of state for an ideal gas is given as

$$P = \rho RT\tag{2.2}$$

These equations are numerically solved using the CalTech Shock & Detonation Toolbox (SDToolbox) for the given initial conditions [61]. The ZND model provides calculable thermodynamic and chemical parameters from initial conditions that are used in the predictive

detonation cell size models analyzed in this work. The model assumes that detonation begins with a non-reactive incident shock wave followed by an exothermic reaction zone. The incident shock compresses the explosive mixture with a marked increase in temperature and pressure to the von Neumann (vN) state. At the vN state, the chemical reactions do not progress for a certain duration called the induction zone. In this zone, molecular dissociation and radical formation begin before the main energy release. The induction zone length is defined as the distance from the shock to the point of maximum thermicity as shown in Fig. 2.1. Following the induction zone, rapid chemical reactions complete the transition of reactants to products in the heat release zone, terminating in the sonic plane, termed the CJ state. The reaction zone thickness Δ_r is defined as the width of the thermicity peak, or the distance for the reaction to occur. The flow following the shock is subsonic (in the reference frame of the shock), and thus the energy release behind the shock is able to be transported to support the shock. For a self-propagating detonation, the shock propagates at the CJ speed, where the products are sonic in the shock frame of reference. Therefore, the chemical energy released by the detonation is used to propagate the shock. The shock speed can be computed using the initial mixture parameters and the CJ model in SDToolbox. The post-shock vN state is the initial condition for the differential equations of the ZND model.

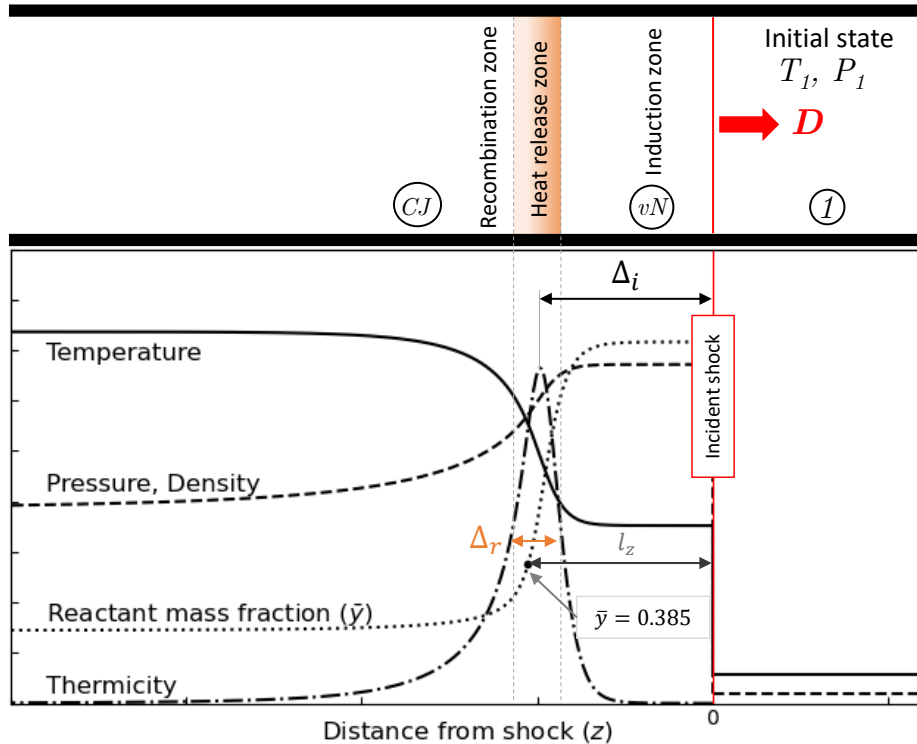


Figure 2.1 – Schematic of ZND detonation temperature, pressure, and density profile for CJ detonation

The one-dimensional ZND model does not fully capture the instabilities that give rise

to detonation cellular structures, as it assumes a steady-state solution in both time and space [14]. In two-dimensions, instability is manifested as transverse oscillations normal to the direction of propagation, which are interacting with the leading shock front. The transverse waves reflect from each other as the leading shock alternates from being a Mach stem to an incident shock for a triple-point configuration shown in Fig. 1.1. This Mach stem is stronger than the leading shock and can facilitate re-ignition. It is these triple-point trajectories from the propagating leading shock and transverse waves that result in the cellular structure of interest to this study.

2.1.1 Factors Affecting Cell Size

The characteristic cell size is generally considered as a measure of the reactivity of a mixture: the smaller the cell size, the more reactive the mixture [62]. Several factors influence the detonation cell size, including pressure, fuel and oxidizer, equivalence ratio, dilution, and temperature. As pressure increases, cell size is seen to decrease following a power law over several orders of magnitude [48] following,

$$\lambda = aP^b \quad (2.3)$$

where a and b are empirically determined constants unique to every mixture. These correlations are plotted for hydrogen and methane data in Fig. 2.2.

Even for the same initial temperature and pressure, the fuel-oxidizer equivalence ratio and dilution significantly influence the detonation cell size, adding additional complexity to modelling. The addition of diluent, such as nitrogen, was investigated for hydrogen-air mixtures at 101 kPa and 293 K to compare cell size to induction zone length from ZND model [64]. The study found that the nitrogen addition significantly desensitizes the mixture, increases cell size and decreases the detonation velocity; however, the ratio λ/Δ_i was similar for all tested dilution mole fractions.

The effect of additives is also important to the mixture of fuel and oxidizer in determining cell size. Several experiments by Austin and Shepherd [48] have investigated the addition of carbon monoxide to mixtures of hydrogen-air, ethylene-air, and hexane-air generally finding that CO does not impact cell size significantly at low mole fraction of CO; however, causes a dramatic increase in cell size after 0.75 mole fraction. They also investigated the influence of addition of increasing amounts of hydrogen or hydrocarbons to CO-air mixtures finding decreased cell width with increasing amounts; the greatest reduction resulting from the addition of C_2H_2 and H_2 , followed by C_2H_4 , and then C_6H_{14} . They found that while CO-air mixtures are not detonable alone, the presence of small amounts of C_6H_{14} , producing reactive hydrogen species, enabled detonation at mole fractions as low as 0.07%. This literature indicates that, even in small amounts, additives play an important role in cell size and should be considered for multi-fuel mixtures. Crane *et al.* [65], [66] evaluated the detonation properties of pure methane compared to actual natural gas and natural gas surrogates containing additives of ethane, propane and carbon dioxide. They found that the actual natural gas and surrogates had a substantially smaller induction

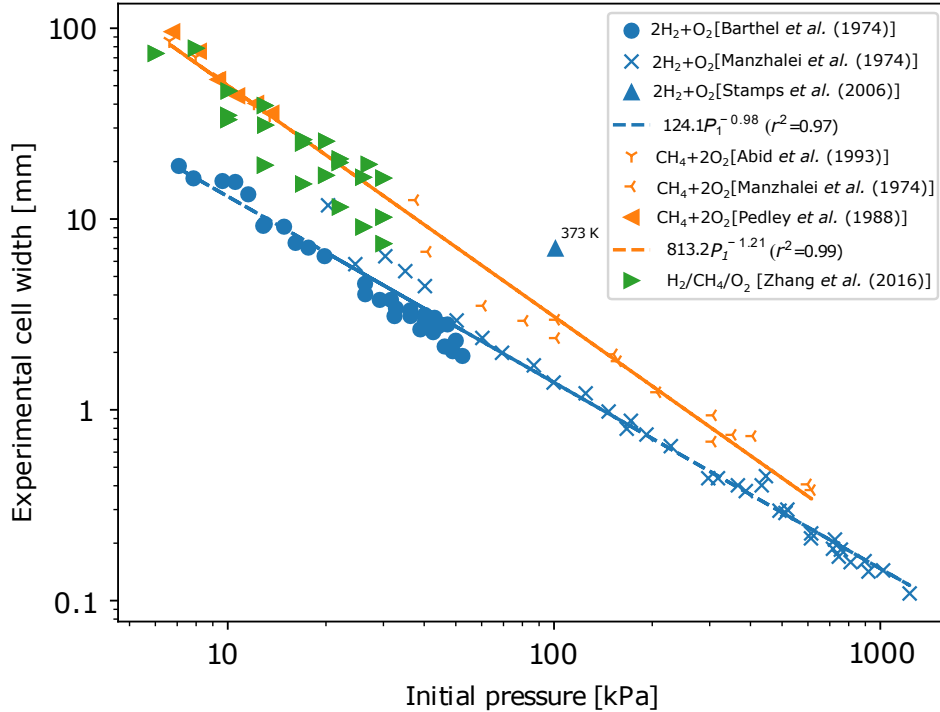


Figure 2.2 – Experimental cell width versus initial mixture pressure for stoichiometric hydrogen-oxygen and stoichiometric methane-oxygen, and binary fuel hydrogen-methane-oxygen at different equivalence ratios, and room temperature. References: Barthel *et al.* (1974) [50], Manzhalei *et al.* (1974) [63], Stamps *et al.* (2006) [51], Abid *et al.* (1993) [56], Pedley *et al.* (1988) [57], Zhang *et al.* (2016) [45]

length than pure methane. Considering the strong correlation of induction length to detonation limits [66], they predict that natural gas is more suitable to RDE application and less safe for pipe confinement applications, since it experienced detonation failure at the lowest pressures out of the three categories of mixtures.

Cell size dependence on temperature was analyzed for hydrogen-air mixtures at atmospheric pressure and initial temperature of 300-650 K by Ciccarelli *et al.* [67] who found that these hotter initial temperatures did not affect cell size at stoichiometric ratio, but did decrease it for rich and lean mixtures. They also found that the general critical tube diameter $d_c = 13 \lambda$ may not be valid at elevated temperatures ($T_1 > 500\text{K}$) and the diameter may need to be greater than 17λ . This is important to RDE in aerospace applications where the engine combustor may operate at elevated temperatures predicted over 600 K [68]. Plaster *et al.* [69] and Zitoun *et al.* [55] conducted experiments with hydrogen-oxygen mixtures at 100 K and 123 K, respectively, and reported that the cell size decreased by approximately a factor of 0.5 compared to measurements at 293 K, for the same initial pressure.

2.2 Cell Size Models

To date, no predictive model has demonstrated sufficient reliability or generality to accurately estimate detonation cell size for previously untested reactant mixtures based solely on initial conditions. This remains true despite the importance of cell size in practical applications, such as defining detonation transmission limits [16], [70], characterizing deflagration-to-detonation transition (DDT) in obstacle-laden systems [71], and informing the design of rotating detonation engines (RDEs). Given the challenges of experimentally determining cell size for every new mixture, various researchers have proposed semi-empirical models to capture observable trends across different conditions. This section reviews the evolution of such models and the incremental advances made toward more broadly applicable predictive capabilities.

2.2.1 Shchelkin and Troshin (1964) [1]

Shchelkin and Troshin [1] proposed an empirical model for estimating detonation cell size λ based on the induction zone length Δ_i . It is given by the relation $\lambda = A\Delta_i$ where A is a dimensionless constant of proportionality when λ and Δ_i have the same length units, typically ranging from 30 to 70 depending on the mixture composition and thermodynamic conditions [14]. The model uses the one-dimensional ZND detonation structure for calculating Δ_i , and assumes that the detonation cell width, which characterizes the transverse wave structure, scales proportionally with the induction length.

A key limitation of the model is that the scaling factor A varies significantly between different fuel-oxidizer mixtures, making it necessary to calibrate against experimental data for each specific case. Additionally, the induction zone length is derived from idealized chemical kinetics, which are subject to variations by reaction mechanisms and calculated post-shock speeds.

2.2.2 Gavrikov *et al.* (2000) [2]

The detonation cell size model developed by Gavrikov *et al.* provides a refined approach for predicting the characteristic cellular structure of detonations based on detailed chemical kinetics. They address the major limitation of Shchelkin and Troshin's model by incorporating key stability parameters, specifically the dimensionless effective activation energy $\frac{E_a}{RT}$ and the ratio of chemical energy release to initial internal energy $\frac{Q}{C_v T_1}$, to establish a more robust empirical correlation that spans a broad range of combustible mixtures and operating conditions.

The widths of the characteristic reaction zone were calculated by using the definition that used the distance between the leading shock and the point of the maximum temperature gradient proposed by Shepherd [72]. Reaction zone widths were also calculated using

constant volume explosion reaction times using the post-shock vN gas velocity, corresponding to times of fuel or oxidizer consumption equal to 50% or 90% of the equilibrium state and time of maximum temperature rise.

Gavrikov *et al.* define the stability parameters that might influence the λ/Δ_i correlation. First, the energy ratio parameter $\frac{T_{vN}}{T_1}$ is related to $\frac{Q}{C_v T_1}$ and the CJ Mach number (M_{CJ}) by specific heat ratios of products and reactants by the expression

$$\begin{aligned}\frac{Q}{C_v T_1} &= \frac{1}{4} \frac{T_{vN}}{T_1} \frac{(\gamma_r + 1)^2}{(\gamma_p^2 - 1)} \\ &= \frac{1}{2} M_{CJ}^2 \frac{\gamma_r (\gamma_r - 1)}{(\gamma_p^2 - 1)}\end{aligned}\quad (2.4)$$

This relation is based on the ZND model and Rankine-Hugoniot shock jump equations for energy conservation between the unburned and burned states, assuming a CJ detonation and ideal gas. The definition of the effective activation energy is based on the constant-volume reaction times behind shocks with two different speeds D_1 and D_2 by:

$$\frac{E_a}{R} = \frac{\ln\left(\frac{t_1}{t_2}\right)}{\frac{1}{T(D_1)} - \frac{1}{T(D_2)}}\quad (2.5)$$

which assumes that the difference in reaction times is due to the difference in temperatures. Gavrikov *et al.* also suggest that using the von Neumann state as initial reaction conditions does not represent the actual reaction in a detonation wave and multi-dimensional detonations are characterized better by a state behind the shock with velocity ranging from $1.0 D_{CJ}$ to $1.6 D_{CJ}$. After a sensitivity analysis to the shock velocity, $1.3 D_{CJ}$ is used in the effective activation energy expression for the model as giving the best correlation.

Gavrikov *et al.* calibrate their empirical model against cell size data consisting of hydrogen combustibles, H_2/O_2 diluted with Ar, and CH_4/O_2 , C_2H_4/O_2 , C_2H_6/O_2 diluted with Ar and N_2 . The function for $\frac{\lambda}{\Delta_i} \left(\frac{E_a}{RT_{vN}}, \frac{T_{vN}}{T_1} \right)$ is constructed using least squares fitting giving the lowest mean square deviation resulting in an equation with the form:

$$\begin{aligned}\ln\left(\frac{\lambda}{\Delta_i}\right) &= G_2(g_1 G_2 - g_2) + G_1[g_3 G_1 - g_4 + (g_5 - g_6 G_2)G_2] \\ &\quad + g_7 \ln G_2 + g_8 \ln G_1 + G_2 \left(\frac{g_9}{G_1} - \frac{g_{11} G_2}{G_1^{g_{12}}} \right) - g_{10}\end{aligned}\quad (2.6)$$

where $G_1 = \frac{E_a}{RT_{vN}} = [3, 16]$ and $G_2 = \frac{T_{vN}}{T_1} = [1.5, 8]$ and the values of the coefficients and exponents g_i have been determined empirically and are given in Table 2.1. The model is implemented in SDToolbox [61] and can be used directly by calculating the parameters $\frac{E_a}{RT_{vN}}$ and $\frac{T_{vN}}{T_1}$ from initial mixture conditions.

Table 2.1 – Dimensionless coefficients and exponent of the Gavrikov *et al.* model equation [2]

Coefficients	Values
g_1	-0.007843787493
g_2	0.1777662961
g_3	0.02371845901
g_4	1.477047968
g_5	0.1545112957
g_6	0.01547021569
g_7	-1.446582357
g_8	8.730494354
g_9	4.599907939
g_{10}	7.443410379
g_{11}	0.4058325462
g_{12}	1.453392165

In their study, the model is tested against their dataset and shows a strong correlation between the experimental and calculated data [2]. Importantly, the model gives accurate estimates for lean mixtures and steam dilution which are typically not reliably represented by standard ZND calculations [2]. The mixtures with argon dilution are examples of reactions with the highest $\frac{T_{vN}}{T_1}$ ratio and lowest activation energy, to which the model presents cell widths within the generally accepted range of uncertainty of experimental measurements of 200% [14]. Hydrocarbon fuels tend to be well represented by standard ZND correlations due to their narrow range of stability parameters $\frac{E_a}{RT_{vN}} = [5, 10]$ and $\frac{T_{vN}}{T_1} = [4.5, 6.5]$. The model agrees well with hydrocarbon data for equivalence ratios less than two, though it poorly represents the data for $\phi > 2$. Gavrikov *et al.* also tested the model against a set of hydrogen-air mixtures diluted with CO₂ where it showed good agreement despite not being represented in the initial fitting parameters.

2.2.3 Ng (2005) [3]

Ng [3] developed a semi-empirical model for detonation cell size prediction based on chemical kinetics and ZND theory. The model is tested using existing cell size measurements found in literature and uses chemical mechanisms from Li *et al.* (2004) [73] for hydrogen mixtures and Konnov (2000) [74] for hydrocarbons. They use the definition of reaction zone length by Shepherd [75] corresponding to the distance between the leading shock and location of the maximum temperature gradient computed by ZND theory.

Ng [3] defines an improvement on the λ/Δ_i correlation in a polynomial series given

by:

$$\lambda = W(\chi) \cdot \Delta_i = \sum_{i=1}^N (w_i \chi^{-i} + z_i \chi^i) \cdot \Delta_i \quad (2.7)$$

where χ is a non-dimensional stability parameter defined as

$$\chi = \frac{E_a}{RT_{vN}} \frac{\Delta_i}{\Delta_r} \quad (2.8)$$

where $\frac{E_a}{RT_{vN}}$ is the effective activation energy for a constant volume explosion, Δ_i is the induction zone length, and Δ_r is the reaction zone length as shown in Fig. 2.1. Ng provides constants up to $N = 3$ for the correlation based on multi-variable least-squares fitting with experimental data (Table 2.2). Ng’s model is also implemented in SDToolbox [61] requiring inputs of the Δ_i and χ . The improved correlation takes into account the temperature

Table 2.2 – Dimensionless coefficients of the Ng [3] model equation with $N = 3$

Coefficients	Values
W_0	30.465860763763
w_1	89.55438805808153
w_2	-130.79282369483
w_3	42.02450507117405
z_1	-0.02929128383850
z_2	$1.026325073064710 \times 10^{-5}$
z_3	$-1.031921244571857 \times 10^{-9}$

sensitivity and the shape of the reaction structure for the ZND, providing a better estimate of cell size. Ng [3] shows that the correlation provides a better representation at rich and lean mixture limits for hydrogen-air mixtures, which is poorly represented with the constant coefficient proportionality model by Shchelkin and Troshin [1]. Ng’s model also provided better accuracy to mixtures with elevated temperature and pressure in his testing. Similar to Gavrikov’s model, though, this model presents large discrepancies at higher equivalence ratios possibly due to inefficiencies in kinetic mechanism. Ng [3] further tests the model on new data of hydrogen-air diluted with CO_2 and hydrogen-oxygen diluted with argon which provides reasonable estimates within the precision of experimental data.

2.2.4 Monnier *et al.* (2023) [5]

This model predicts the representative detonation cell width based on graph theory, geometric probabilities, and the ZND model. The fundamental premise is that the cellular detonation burns mass at the same rate as a steady planar ZND detonation. This ensures mass conservation over long timescales and provides a link between detonation structure and reaction zone dynamics.

Monnier *et al.*’s model [5] is based on several assumptions:

1. transverse waves follow a stationary ergodic motion by which the cellular structure behaves as a stochastic process where statistical properties remain unchanged over time and space;
2. the mass of reactants consumed per unit time in a multicellular detonation is the same as in an equivalent planar ZND detonation;
3. the front-view structure of detonation cells can be statistically represented by a hexagonal tiling; and
4. the model assumes ignition occurs solely due to adiabatic shock compression and does not account for turbulent diffusion.

The model calculates the CJ speed and ZND parameters from initial conditions. It predicts a mean burnt mass fraction of $\bar{y}_z = 0.385$ and a ratio of cell width to cell length of $\lambda/L = 0.64$. This mean burnt mass fraction is shown for the ZND calculation in Fig. 2.1 where it lies close to the point of maximum thermicity. Its physical premise is that the detonation propagates under conditions where the real cellular and ZND average combustion rates are identical. This equality implies that the average burnt mass of the cell and ZND model are equal, thus $\bar{y}_{\text{cell}} = \bar{y}_{\text{ZND}} = \bar{y}$. Then, by their respective reaction times, it must satisfy that the time for half the cell length (the point where the transverse waves collide) is equal to the same ZND time to produce that burned fraction and thus $\frac{2}{t_{\text{cell}}} = \frac{\bar{y}_z}{t_{\text{ZND}}}$. This occurs as a function of the distance from the shock z where the average specific volume ($\nu = \frac{1}{\rho}$) of the mixture is given by:

$$\bar{\nu}_z(\bar{y}_z) = (1 - \bar{y}_z) \nu_{\text{vN}} + \bar{y}_z \nu_{\text{CJ}} \quad (2.9)$$

knowing the specific volumes at von Neumann and CJ states by the post-shock calculations in SDToolbox [61]. Then, the average specific volume is given by:

$$\bar{\nu} = \bar{y} \frac{\nu_{\text{CJ}}}{\bar{\nu}_z(\bar{y}_z)} \quad (2.10)$$

Using these parameters, the representative ZND reaction length l_z to produce the mean burn mass fraction is calculated by the ZND induction zone length, where l_z as depicted in Fig. 2.1, is the distance from the incident shock to the point where $\bar{y}_z = 0.385$:

$$l_z = \frac{\Delta_i}{(1 - \bar{\nu})} \quad (2.11)$$

The particle time at the position z is given by the ratio of distance $z(t)$ to flow speed $u(t)$ from the ZND calculation:

$$t(z) = \frac{z(t)}{u(t)} \quad (2.12)$$

The solution for cell length is then calculated using the intersection of the two curves $f_1(z)$ and $f_2(z)$ as a function of the distance from the shock z , where $z = l_z$:

$$f_1(z) = \frac{\lambda}{L} \frac{2}{\bar{y}_z} D_{\text{CJ}} t_{\text{m}}(z) \quad (2.13)$$

$$f_2(z) = \frac{\lambda}{L} \frac{2}{\bar{y}_z} \frac{\nu_0}{\bar{\nu}_z(\bar{y}_z)} z \quad (2.14)$$

The value of f_1 or f_2 at the intersection of these two curves at a distance l_z from the shock yields the cell length prediction. Given their correlation of $\lambda/L = 0.64$, the cell width λ can be determined. This intersection physically represents the compatibility constraint that the cellular detonation produces the same mean burnt mass fraction at the same time as the ZND process.

The model, being based on a post-processed ZND calculation, depends on the initial chemical mechanism used. It is based on geometrical considerations derived from experimental observations and statistical considerations indicating that transverse waves follow a stationary ergodic motion. Therefore, the chemical kinetic mechanism must be appropriate to the mixture used. Moreover, the authors specify that the statistical average cell size measured is only significant for regular or moderately irregular mixtures, and therefore the combustion process is limited to reaction zones whose ignition mechanism is adiabatic shock compression only such as those with H_2 , C_3H_8 , and C_2H_4 . When compared to methane-oxygen mixtures, the model overestimates the cell size, indicating limits in prediction for other ignition mechanisms such as turbulent diffusion [5]. Additionally, the number of cells must be large and independent of confinement to accurately employ this model in comparison.

2.2.5 Bakalis *et al.* (2023) [4]

Bakalis *et al.* [4] present an Artificial Neural Network (ANN)-based model for predicting detonation cell size, using chemical kinetic and thermodynamic input parameters as the training variables. The model is trained and validated using experimental data from the Caltech detonation database [76], which includes a variety of gaseous fuel-oxidizer mixtures under different initial conditions. The study systematically determines optimal ANN hyperparameters, including the number of hidden layers, neurons per layer, and training methodologies to minimize loss and maximize accuracy.

A deep neural network architecture is selected, and its training dataset consists of 388 experimental cell size measurements, along with calculated chemical kinetic and thermodynamic parameters obtained from steady one-dimensional ZND detonation modeling. Konnov’s detailed reaction mechanism and the CHEMKIN-II package are used for kinetic analysis. The features considered include the induction length (Δ_i), maximum thermicity ($\dot{\sigma}_{\max}$), detonation Mach number (M_{CJ}), initial pressure, temperature, equivalence ratio, and activation energy.

The dataset is split into training (60%), validation (20%), and testing (20%) sets. The ANN is optimized through hyperparameter tuning, selecting between 1 to 4 hidden layers with varying neuron counts (512, 256, 128, 64). The Rectified Linear Unit activation function is used due to its efficiency in handling non-linearities. The loss function is based on the squared relative error which ensures that predictions are not disproportionately influenced by large cell sizes.

The study finds that an ANN using only three features: Δ_i , $\dot{\sigma}_{\max}$, and M_{CJ} , offers a prediction accuracy of 22.34% mean error, with better performance for smaller cell sizes. A feature sensitivity analysis reveals that increasing the number of features beyond three does not significantly improve accuracy and, in some cases, worsens performance. The authors also tested the χ parameter (Eq. 2.8) [77] though found worse results than using the constituent parameters separately. Bakalis *et al.* claim their model to have 23-30% error, compared to the Gavrikov *et al.* [2] and Ng [3] models which have prediction errors up to 50%.

A limitation is that the model is trained on a single chemical kinetic mechanism (Konnov’s mechanism), which may limit its generalizability to mixtures not well represented in the dataset. Bakalis and Ng [78] further tested their model to predict the cell size of hydrocarbon/ammonia/nitrous oxide mixtures which are not used in the original training of the ANN model. The predictions reveal good agreement to measured data, and also different chemical mechanisms.

2.2.6 Other Models Considered

In 2006, Vasil’ev conducted a review of all known models for prediction of detonation cell size [79], [80]. The main categories of models discussed in the paper include one-dimensional idealized models, acoustic models, semi-empirical models, closed-cell models, and numerical simulations. Each of these models differs in complexity, assumptions, and predictive capabilities.

The acoustic wave hypothesis, first introduced by Strehlow [52], attempts to explain the periodicity of detonation cells by considering the role of transverse waves as acoustic disturbances. These models propose that small perturbations in the shock front generate acoustic waves that travel within the induction zone, amplifying and eventually producing transverse wave structures. However, experimental comparisons reveal major discrepancies, with calculated values often being 30 to 180 times smaller than measured cell sizes. The common deficiency in acoustic models for cell size is the neglect of the shock interactions at the cellular detonation front [80]. Since the spatial distance of sound sources are not determined in the models, they fail to predict the structure. Attempts by Barthel [50], [81], and Chiu and Lee [82] to extend the acoustic theory to encompass the interactions and chemical kinetics were unsuccessful.

The early parametric models of cell size include models which are justified by some factor that influences cell size such as pressure, dilution ratio, and the wave velocity profile. This includes models by Strehlow [83], Barthel [81], and Lundstrom and Oppenheim [84]. However, the physics and comprehensive characteristic parameters of the cell are not included and therefore only illustrate qualitative modeling of trends like change in cell size with increasing pressure or dilution [80].

The cell models of Vasil’ev *et al.* are postulated in several papers [80], [85]–[88] and

incorporate the multifront nature of detonation waves, emphasized by modelling microexplosions at triple points. Vasil'ev *et al.* describe the propagation of a detonation by the following steps: collision of transverse waves, formation of a local blast wave (microexplosion), instantaneous chemical energy release, compression and heating of mixture in the induction zone, and the next transverse waves arriving to ignite the mixture and renew the cycle. A similar idea of model is proposed by Crane *et al.* [89], which uses one-dimensional cylindrical blast simulations to predict a steady kernel size unique to a detonable mixture; however, this model is computationally intensive and still requires refinement before further testing.

It has become common to model the cell size using unsteady Euler or Navier-Stokes flow equations coupled with kinetics based typically on the Arrhenius equation [79], but also possible with full chemistry. The primary restriction with these is computational power and time that limit their use in gaining rapid predictions of cell size. Moreover, simulation code is not widely available and implementation has been limited to fuels primarily composed of hydrogen to determine the 2D and 3D cellular structure [79]. Furthermore, given the relative novelty of these models, they continue to need validation against experimental results to ensure accurate parameters in the software implementation. Therefore, simple approximation models for cell size are not readily available with numerical simulations and many fail to accurately represent the cell size.

In 2019, Malik *et al.* [90] created a deep artificial neural network to predict detonation cell size which does not use effective activation energy or reaction length definitions. Their model uses the fuel concentration as an input to determine the adiabatic flame temperature, CJ velocity, CJ temperature, and CJ pressure. As such, their model is unique to specific mixtures that they tested including hydrogen-air, methane-air, methane-oxygen, propane-air, and propane-oxygen. Malik *et al.* found that their model was accurate in the subset of data that they tested, with a maximum mean error of 13.9% in methane-air due to more irregular detonation cell size distributions. Similarly, Siatkowski *et al.* [91] used a machine learning model to predict the detonation cell size of biogas-oxygen mixtures only based on initial pressure, equivalence ratio, and percentage of methane. Despite the high accuracy of these models, since they are limited by the mixture type, and these are not mixtures tested for this study, they cannot be compared to this thesis' data. Also, the code for training the model is not available in the public domain, and a new subset trained on this study's data is out of scope.

Overall, while these models are considered, they are not used directly for comparison to the experimental data in this study. This is because of computational limitations for extensive numerical simulations that defeat the purpose of obtaining rapid estimations and do not accurately predict the cell size. Also, the earlier studies are qualified as being only qualitatively accurate, or are unable to be used for the mixtures in this study.

Chapter 3

Experimental Methodology

3.1 ENSMA Detonation Channel

The experiments were performed in a six metre long and 52 mm diameter cylindrical channel (Fig. 3.1). Either an electrical spark, having an energy of 4 J, or one from a Bosch R6 automotive spark plug was used to ignite the mixture, depending on equipment serviceability. A 1 m Shchelkin spiral promoted DDT and the following 3 m provided distance for the detonation to reach steady-state. In the final 2 m, Kistler 603B pressure transducers paired with Kistler 5018A charge amplifiers, and Piezo PZT5A shock pins were placed to measure the passage of the detonation wave and measure its velocity. A stainless steel sheet covered with soot was rolled along the inner circumference of the cylindrical channel in the last 30 cm to record triple point trajectories and measure cell sizes. Steel wool could also be placed at the end of the channel to prevent the reflected shock from interfering with the soot foil results. In some cases, the spark was not sufficient to obtain a steady detonation in the channel. To promote DDT, a driver mixture of stoichiometric ethylene-oxygen was used separated by three 20 micron stacked Mylar diaphragms; this gave a 1 m driver section and 5 m test gas section. The test mixtures were prepared by the method of partial pressures and left to mix over at least 12 hours in a gas bottle. Mixtures were prepared with varying mole fractions of hydrogen, carbon monoxide, and methane to cover the range of alternative fuel sources from Fig. 1.4 and effectively model the trends of cell size with

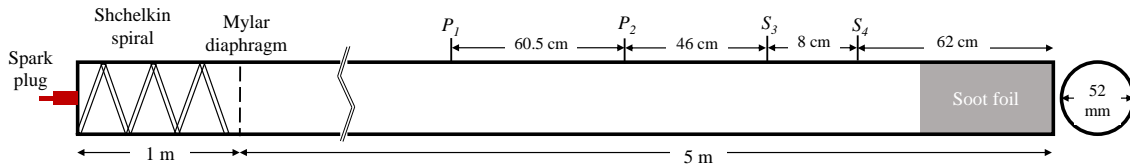


Figure 3.1 – Experimental setup of cylindrical detonation channel at ENSMA.

changing fuel fraction. For each trial, a partial vacuum was created in the channel to at least 1% of the desired test pressure.

Experiments were performed at initial absolute pressures of 20, 50, 100 and 200 kPa at initial temperatures ranging from 17-22°C in a cylindrical channel. The composition of the multi-fuel mixtures corresponds to the alternative fuels of interest in the ternary plot (Fig. 1.4), the mixtures are shown in Table 3.1 in mole fraction basis and as a fraction of the fuels where $X_{f,i} = \frac{X_i}{\sum X_{\text{fuels}}}$. These mixtures were specifically chosen to systematically cover the range of ternary compositions lacking cell size data, as shown in Fig. 1.4. The evenly spaced mixtures across the ternary plot enable a more detailed analysis of trends associated with varying fuel fractions. Additional binary CO-CH₄ tests were conducted to address gaps identified in the literature. Combined with existing literature data, these experiments effectively complete the dataset for multi-fuel mixtures composed of hydrogen, methane, and carbon monoxide. For each mixture and pressure combination, a minimum of one test was conducted, with additional tests performed when surplus gas and time permitted or when soot foil quality rendered initial results unusable. In total, 52 successful tests, with no failed attempts to detonate, were completed for this study. An additional 44 successful tests were performed as part of a contract but not used in this study; 19 attempts to detonate these contract mixtures were unsuccessful. Each test took about one hour to perform with two researchers.

Table 3.1 – Composition by mole fraction of binary and ternary mixtures tested

Mix	X_{H_2}	$\frac{X_{\text{H}_2}}{\sum X_{\text{fuels}}}$	X_{CH_4}	$\frac{X_{\text{CH}_4}}{\sum X_{\text{fuels}}}$	X_{CO}	$\frac{X_{\text{CO}}}{\sum X_{\text{fuels}}}$	X_{O_2}
1	0.083	1/5	0.250	3/5	0.083	1/5	0.583
2	0.190	2/5	0.190	2/5	0.095	1/5	0.524
3	0.333	3/5	0.111	1/5	0.111	1/5	0.444
4	0.222	2/5	0.111	1/5	0.222	2/5	0.444
5	0.111	1/5	0.111	1/5	0.333	3/5	0.444
6	0.095	1/5	0.190	2/5	0.190	2/5	0.524
7	0	0	0.222	1/2	0.222	1/2	0.555
8	0	0	0.133	1/4	0.400	3/4	0.466
9	0	0	0.286	3/4	0.095	1/4	0.619

Cell size measurements were recorded for each cell on the foil. For each test, a cell size frequency distribution and an average cell size were determined, and compared to similar measurements from another researcher. The detonation velocity was obtained by measuring the time between successive peaks in the oscilloscope traces and using the known distances between sensors. These velocities and pressures could be compared to expected CJ conditions to confirm a CJ detonation at the soot foil. Fig. 3.2 shows an example pressure transducer and shock pin trace for a trial completed in the ENSMA detonation channel. The corresponding time, distance, and speed calculations are shown in Table 3.2. The velocity is calculated by determining the point where the initial rise in pressure occurs signalling the arrival of the shock. This threshold was selected as the point where

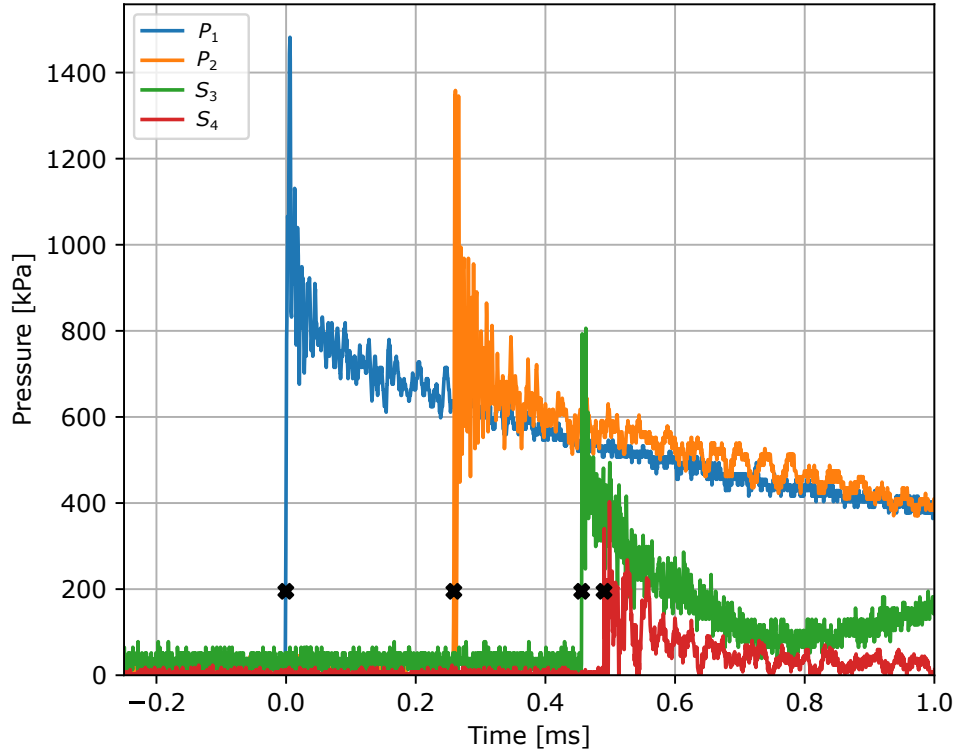


Figure 3.2 – Pressure transducer and shock pin traces for $0.083 \text{ H}_2 + 0.250 \text{ CH}_4 + 0.083 \text{ CO} + 0.583 \text{ O}_2$ (Mix 1) at $P_1 = 50 \text{ kPa}$. Lines correspond to pressure transducers at locations shown in Fig. 3.1.

the signal exceeds 0.5 V . Knowing the physical distances between the sensors, the velocity can be calculated by $u = \frac{\Delta x}{\Delta t}$ and then averaged to determine the detonation velocity. For this example calculation, the CJ velocity is calculated as $D_{\text{CJ}} = 2310.2 \text{ m/s}$, and thus the experiment achieved a detonation average velocity of $100.8\% D_{\text{CJ}}$.

The detonation velocity was calculated for all experimental trials and compared to the expected CJ velocity from SDToolBox [61]. Fig. 3.3 shows this comparison and illustrates that the experimental average detonation velocity for all successful tests was always within $\pm 2\%$ of the CJ velocity. This validates that the apparatus is suitable for the initial conditions of these experiments and a CJ detonation is observed at the soot foil for cell size measurements.

Table 3.2 – Pressure transducer and shock pin results for $0.083 \text{ H}_2 + 0.250 \text{ CH}_4 + 0.083 \text{ CO} + 0.583 \text{ O}_2$ (Mix 1) at $P_1=50 \text{ kPa}$, calculation of detonation velocity.

Parameter	$P_1 - P_2$	$P_2 - P_3$	$P_3 - P_4$
Time between peaks [ms]	0.2592	0.1972	0.0344
Distance between sensors [cm]	60.5	46.0	8.0
Calculated velocity [m/s]	2334.1	2332.7	2325.6
Average detonation velocity [m/s]	2330.8		

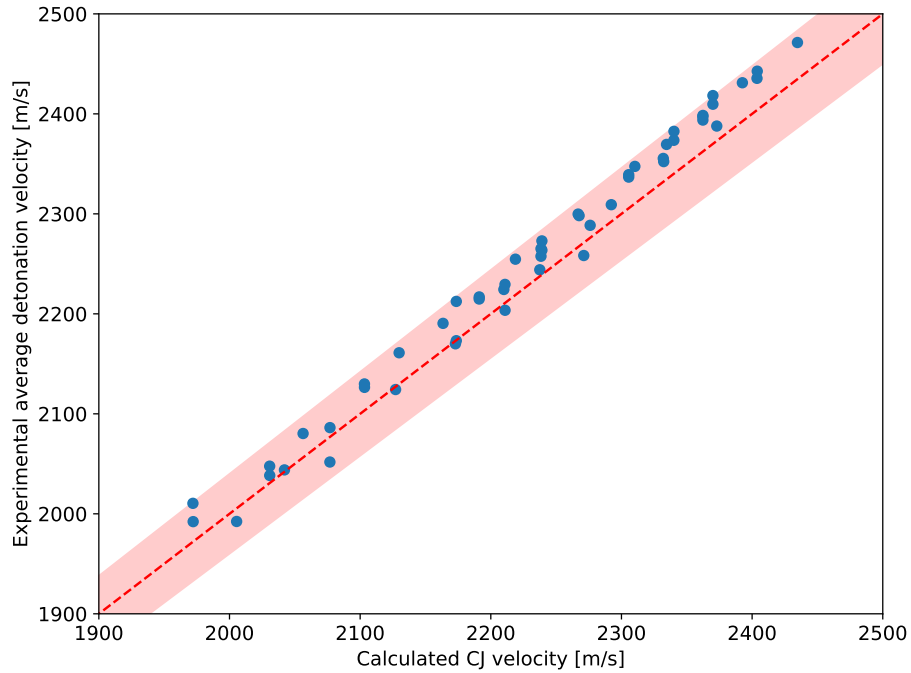


Figure 3.3 – Comparison of calculated CJ velocity using SDToolBox [61] to experimental average detonation velocities. Pink band indicates $\pm 2\%$ error.

3.2 RMC Detonation Channel

Part of the work of this thesis is the development and inaugural testing of the RMC detonation channel. This channel provides an in-house capability to test various detonable mixtures and rapidly obtain detonation cell size and velocity data to compare to existing literature or develop future models. The rectangular channel is comprised of four sections, each 4 ft (1.22 m) long, 1 ft (0.30 m) tall and 3 in (7.6 cm) wide, with plans to add an additional optical section for Schlieren photography in the future (Fig. 3.4).

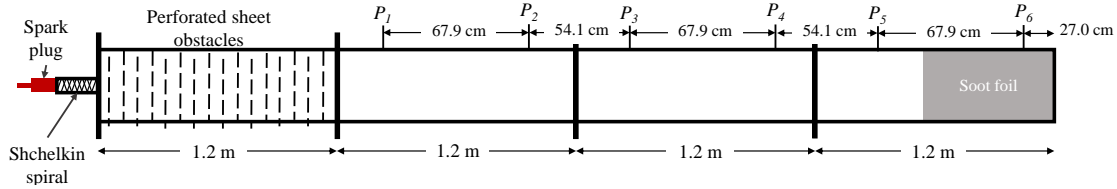


Figure 3.4 – Experimental setup of rectangular detonation channel at RMC

Starting with pure gases, the detonable mixture was created using the method of partial pressures and stored in a mixed gas bottle for at least 24 hrs. To perform an experiment, a vacuum was created in the channel and mixing panel. The mixed gases were then injected into the channel via the mixing panel to the desired test pressure, measured by Omega PXM309 pressure transducers and displayed on an Omega DP8EPT digital panel. Once the test pressure was reached in the channel, the valve connecting it to the panel was closed and a vacuum was created in the mixing panel to prevent explosive gas from remaining in the lines. The ignition system was comprised of an automotive spark plug connected to a smart ignition coil and a 12 V battery. A signal generator is used to trigger both the ignition source and the data acquisition device, which also records the data from the pressure transducers to determine the detonation velocity.

A Shchelkin spiral was created using two 12.7 cm long, 1.91 cm outer diameter, and 0.267 cm wire diameter stainless steel spring in a 1.27×30 cm (1/2×12 inch) standard NPT nipple to promote DDT. Once the detonation entered the main channel, there was a 1.22 m (4 ft) long region of obstacles generated by successive perforated sheets, followed by a 2.44 m (8 ft) length to allow the detonation to reach steady CJ state. PCB Piezotronics model 113B21 piezoelectric pressure transducers were placed in the second, third and fourth channel sections to capture the detonation speed and pressure and compare to the expected CJ state. In the final section, cold rolled, hardened 6061-T6 aluminum plates 30 cm×30 cm×1.6 mm (12×12×0.063 in) were installed by affixing them to the steel channel using single-sided magnets. The adhesive side of each magnet was taped to the back of the aluminum plate, while the magnetic side attached to the steel. The plate was coated with soot using a kerosene lamp within a fume hood and methodically moving the foil above the burning flame to obtain an even and suitable coating across the entire surface. Different materials and thicknesses were tested for survivability, efficiency, and clarity of visualizing the soot traces. After the mixture was detonated, the vacuum pump was used to extract the combustion products to the exterior of the building via a blower motor and diluting with air to comply with exhaust gas regulations. The operating procedures for the RMC channel are given in Appendix B.

3.3 Detonation Cell Size Measurements

Several methods exist in literature for measuring cell size manually. A common technique is by first defining long lived tracks on the foil and drawing their trajectories [14]. Then, the cell size is determined by measuring the spacing at different locations between adjacent marked tracks of triple point trajectories. While this is easier for regular mixtures like acetylene-oxygen, irregular mixtures, like most hydrocarbons-air, have much more subjective triple-point tracks which often appear and disappear or converge and diverge [92]. For example, Sharpe and Radulescu [92] found large variability in cell size estimations of an irregular mixture by eight different researchers which differed by approximately a factor of two.

Attempts have been made to digitally process soot foils. Shepherd and Tieszen [75] employed taking the two-dimensional power spectrum of the scanned foils to analyze the spectral content. An autocorrelation process by Sharpe and Radulescu found these methods are highly dependent on the quality of signal-to-noise ratio and are inadequate for more irregular soot foils [92]. Shepherd *et al.* [93] also used a digital spectral processing technique to obtain a quantitative spectrum of wavelengths present in the structure for varying regularities of mixtures; this recognized the merits of the distribution-style technique of presenting cell size, similar to the histograms used in this study.

In this study, the cell size measurement technique involved using computer software developed by Alexandre Poyet (a PhD candidate from ENSMA). The software uses a known scaling factor of pixels to millimeters, and the user draws the cell width of each visible cell on every soot foil image. This process is less subjective to determining marked tracks and is applicable to irregular mixtures if considering an entire distribution. Fig. 3.5 shows an example of this technique by the author, the green lines represent the measured cell widths.

3.3.1 Cell Size Statistics

Using the digital soot foil traces, a histogram can be created which shows the distribution of all measured cells. For the soot foil from Fig. 3.5, the histogram is shown in Fig. 3.6 along with several continuous probability distribution functions that are proposed to best fit the data. Visual inspection of the experimental cell size distribution histograms shows that the distribution is right-skewed. Some right-skew distributions that visually fit the histograms include logarithmic-normal, exponential, Weibull, and gamma [94].

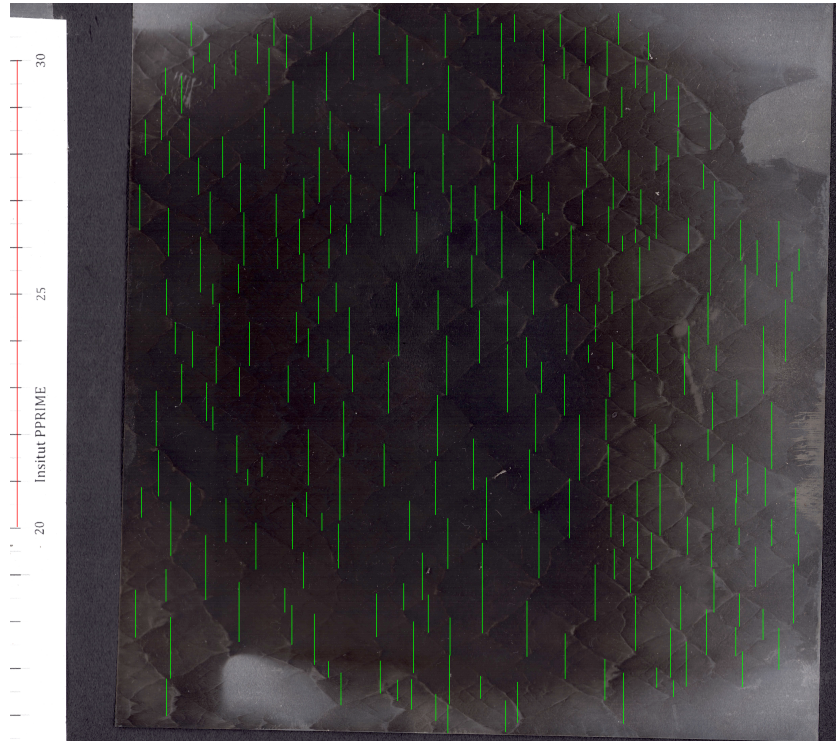


Figure 3.5 – Soot foil with measurement traces for CJ detonation in cylindrical channel for $0.083 \text{ H}_2 + 0.250 \text{ CH}_4 + 0.083 \text{ CO} + 0.583 \text{ O}_2$ (Mix 1) at $P_1 = 49.99 \text{ kPa}$, $T_1 = 18.1 \text{ C}$. Detonation propagates left to right.

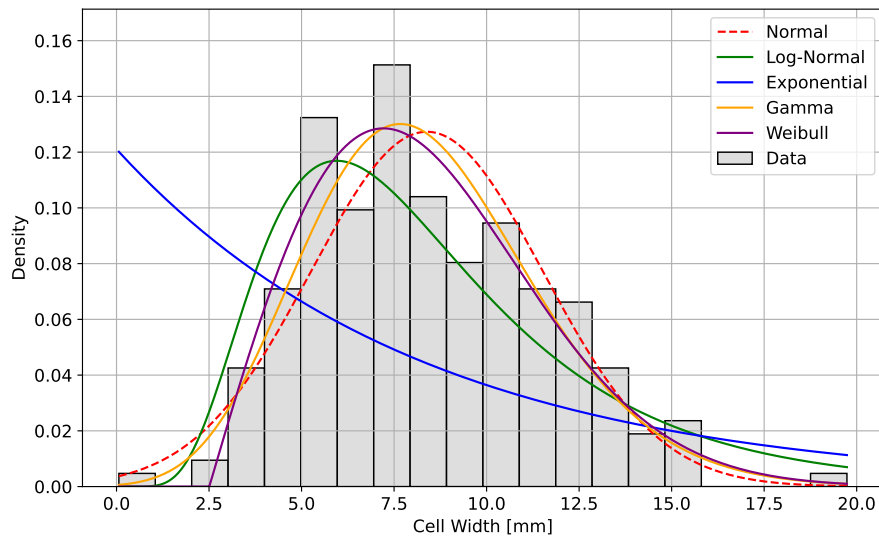


Figure 3.6 – Density histogram of experimental cell size measurements and probability density functions for various distributions for $0.083 \text{ H}_2 + 0.250 \text{ CH}_4 + 0.083 \text{ CO} + 0.583 \text{ O}_2$ (Mix 1) at $P_1 = 50 \text{ kPa}$

Each of the continuous probability distributions varies in its shape and can be described by a specific probability density function that is comprised of several parameters. The normal or Gaussian distribution has the general form of [94]

$$f(x) = \frac{1}{\sqrt{2\pi\sigma^2}} e^{-\frac{(x-\mu)^2}{2\sigma^2}} \quad (3.1)$$

where μ is the mean of the distribution, and σ^2 is the variance. A normal distribution is common in statistics to represent real random variables with unknown distributions.

Similarly, a log-normal distribution is a continuous distribution in which the logarithm of a random variable is normally distributed. It is commonly used in bounded phenomena and follows the function [94]

$$f(x) = \frac{1}{x\sigma\sqrt{2\pi}} e^{-\frac{(\ln x - \mu)^2}{2\sigma^2}} \quad (3.2)$$

where μ and σ^2 are the mean and variance of the log-normal distribution.

An exponential distribution is typically used to model the occurrence of events that occur continuously and independently at a constant rate, such as time between events. The probability density function is given by [94]

$$f(x) = \xi e^{-\xi x} \quad (3.3)$$

where ξ is the rate parameter.

A Weibull distribution is often used to model a time between failure for different physical systems like cycle analysis for mechanical parts or number of failures with time [94]. The Weibull distribution follows the probability density function

$$f(x) = \frac{\beta}{\delta} \left(\frac{x}{\delta}\right)^{\beta-1} e^{-\left(\frac{x}{\delta}\right)^\beta}, x \geq 0 \quad (3.4)$$

with scale parameter $\delta > 0$ and shape parameter $\beta > 0$.

The gamma distribution is commonly used in modeling econometrics and life testing like waiting times [94]. Its probability density function is a two-parameter model which follows

$$f(x) = \frac{\zeta^r}{\Gamma(r)} x^{r-1} e^{-\zeta x}, x > 0 \quad (3.5)$$

where ζ is the rate parameter, r is the shape, and $\Gamma(r) = (r-1)!$ for $r > 0$.

By inspection of Fig. 3.6, it clearly shows that a normal distribution or exponential are not the best fit. It is evident that a right-skew distribution like log-normal, Weibull or gamma are likely to fit most of the data in this study. For this particular example, it shows that a log-normal distribution is likely to best fit the data. This visual fit was repeated for

several trials with the same conclusion. However, it is immediately noted that some trials do not form a distribution at all due to lack of data; these are ignored for the suitability of the distribution, but the mean is still used for comparison to cell width models in the remainder of the study.

Several quantitative methods exist to evaluate the fit of a dataset to a given distribution. A χ^2 goodness-of-fit test was performed on each trial conducted. This test compares the observed frequencies (O) of the data bins in a histogram to the expected frequencies (E) from a hypothesized distribution. The comparison parameter is calculated by [94],

$$\chi^2 = \sum_{i=1}^n \frac{(O_i - E_i)^2}{E_i} \quad (3.6)$$

where n is the number of bins. The p -value is also calculated that represents the smallest level of significance that would lead to the rejection of the null hypothesis [94], or the probability that the data would have occurred by random chance. Generally in statistics, a 95% confidence or $p = 0.05$ is used as the significance limit for the p -value where a larger value is not statistically significant enough to reject the null hypothesis. The null hypothesis in a χ^2 test is that the data follows the specified distribution. Therefore, a low χ^2 and high p -value is indicative that the observed data fits the expected distribution well. The p -value is dependent on the degrees of freedom (df) of the study which is determined by the number of bins minus the number of estimated parameters (like mean and standard deviation) minus one. Then, using the χ^2 cumulative distribution function (CDF), the p -value is calculated by the following equation [94] where the χ^2 distribution is solved using the SciPy stats library [95] for the obtained χ^2 value:

$$p = 1 - \text{CDF}_{\chi^2}(\chi_{\text{obs}}^2, df) \quad (3.7)$$

The χ^2 test is dependent on the number of bins and frequency within a given bin. Cochran [96] proposed a generally accepted rule of thumb where all bins should have at least a frequency of one, and at least 80% of bins should have a frequency greater than five. A lower frequency would give inaccurate results for a χ^2 test [96], [97]. Since 20 bins are selected for the variation of this study's data, this requires a minimum of 84 cells in the histogram (assuming they meet the distribution specified by Cochran [96]) to obtain a reliable χ^2 test result. Therefore, for any trials where this minimum was not obtained, the χ^2 test is deemed insignificant and not used towards the evaluation of distribution fit. Some tests show histograms that have several far outliers either much smaller or larger than the remaining distribution, and although the distribution appears log-normal by visual inspection, it does not satisfy the χ^2 test due to the outliers. These cases are reassessed by clipping any outliers that are greater than 1.5 times the interquartile range and capturing those extreme points in the readjusted bins. The $1.5 \times IQR$ is a commonly used condition for outliers in box plots and since it uses quartiles, it is non-parametric and thus does not assume an underlying distribution [94]. An example of this is shown in Fig. 3.7 where following this adjustment, the χ^2 test supports the log-normal goodness-of-fit with a significant p -value.

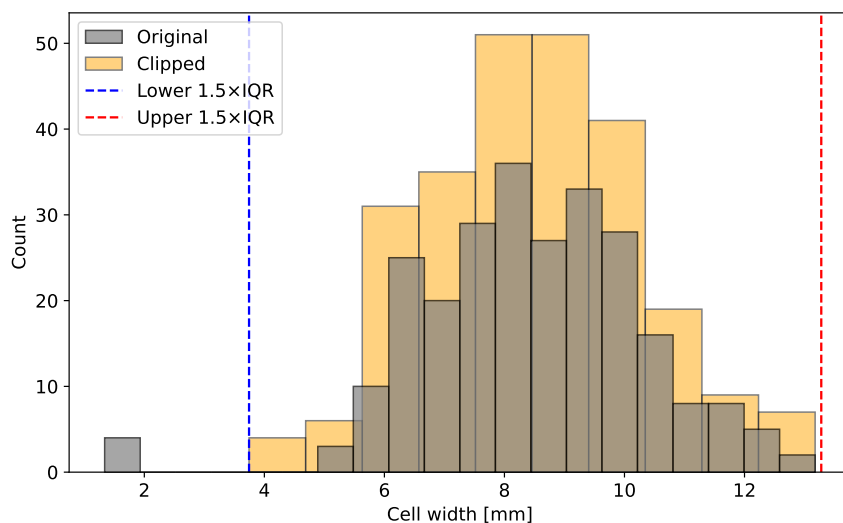


Figure 3.7 – Original and clipped frequency histogram to remove outliers exceeding $1.5 \times IQR$ and using 10 bins for $0.222 \text{ CH}_4 + 0.222 \text{ CO} + 0.555 \text{ O}_2$ (Mix 7), $P_1 = 100 \text{ kPa}$

The χ^2 test results are shown in Table 3.3 for each histogram distribution of mixture and pressure and comparing to each relevant distribution. The data are calculated by the Python stats library. The number of measured cells N is shown for each row with an asterisk signifying too few cells to obtain a reliable χ^2 test. For each row, the bolded values correspond to the distributions that have a low χ^2 value and $p > 0.05$ showing that the null hypothesis cannot be rejected. The data show that the log-normal, Weibull and gamma distributions generally fit the experimental data the best by having lower χ^2 and higher p -values. The log-normal distribution has the most trials with a significant p -value and low χ^2 at 23 trials, followed by gamma at 20, Weibull at 17, normal at 10, and exponential at 0.

In some cases, however, like Mix 3 at 100 kPa shown in Fig. 3.8, none of the distributions significantly represented the data accurately, despite having a large number of measured cells. From the shape of the histograms, these appear to be bimodal or uniformly distributed. The trials that were discounted for not having enough samples also do not show an obvious distribution when visually inspecting the histograms. These are generally low pressure tests which have larger cells, resulting in fewer total cells to count on a given foil.

The log-normal distribution is selected as the best fit for the experimental data based on the visual fit and assessment of the χ^2 test. This is reflective of the right-skewed distribution observed and the values bound at a minimum of zero. The log-normal distribution is also simple to implement by taking the natural logarithm of the data, and since that presents a normal distribution, it is compatible with statistical tools which assume normality [94].

Table 3.3 – χ^2 goodness-of-fit test for measured experimental cell size histograms compared to statistical distributions. Bolded values indicate significant $p\text{-val} \geq 0.05$.

Mix	P_1 [kPa]	N	Normal		Log-Normal		Exponential		Weibull		Gamma	
			χ^2	p-val	χ^2	p-val	χ^2	p-val	χ^2	p-val	χ^2	p-val
1	20	36*										
1	50	215	34.4	0.02	18.6	0.48	192.3	0.0	18.9	0.45	18.8	0.47
1	100	383	8220.5	0.0	30.3	0.05	177.6	0.0	87.7	0.0	37.5	0.01
1	200	155	20.7	0.35	17.1	0.59	63.2	0.0	13.5	0.81	15.9	0.67
2	20	81*										
2	50	474	13868.9	0.0	51.8	0.0	205.6	0.0	177.4	0.0	71.3	0.0
2	100	425	43.2	0.0	24.9	0.16	323.3	0.0	25.7	0.15	25.2	0.16
2	200	57*										
3	20	100	28.5	0.07	22.4	0.26	44.7	0.0	20.4	0.37	21.6	0.30
3	50	232	26.7	0.11	12.7	0.85	134.3	0.0	15.7	0.68	12.6	0.86
3	100	325	51.9	0.0	40.1	0.0	131.4	0.0	33.7	0.02	39.6	0.0
4	20	71*										
4	50	320	76.0	0.0	17.3	0.57	103.0	0.0	22.8	0.25	16.6	0.62
4	100	326 [†]	22.9	0.01	17.8	0.05	282.7	0.0	42.0	0.0	17.9	0.04
4	200	113 [†]	17.8	0.04	9.3	0.41	79.3	0.0	9.9	0.35	9.8	0.37
5	20	14*										
5	50	259	25.0	0.16	10.8	0.93	104.5	0.0	9.2	0.97	9.8	0.96
5	100	428	189.2	0.0	26.2	0.12	290.9	0.0	45.9	0.0	27.9	0.09
5	200	144	17.6	0.55	12.5	0.86	77.8	0.0	11.6	0.90	12.2	0.88
6	20	44*										
6	50	221	143.3	0.0	16.9	0.60	59.6	0.0	21.7	0.30	17.5	0.55
6	100	371	50.7	0.0	22.0	0.29	307.4	0.0	23.1	0.24	22.7	0.25
6	200	213	23.4	0.22	23.4	0.22	261.5	0.0	49.2	0.0	21.6	0.30
7	20	17*										
7	50	109	43.6	0.0	30.7	0.05	62.6	0.0	30.6	0.04	30.8	0.04
7	100	254 [†]	11.3	0.25	11.2	0.26	201.2	0.0	13.0	0.16	11.2	0.26
7	200	170	18.4	0.50	14.0	0.78	85.6	0.0	13.7	0.80	13.8	0.79
8	20	14*										
8	50	10*										
8	100	208	52.5	0.0	28.1	0.08	138.2	0.0	34.3	0.02	28.9	0.07
8	200	216	28.8	0.07	28.4	0.08	105.5	0.0	24.7	0.17	28.2	0.08
9	20	17*										
9	50	133	94.2	0.0	19.3	0.44	62.5	0.0	21.8	0.29	18.3	0.51
9	100	434	39.8	0.0	17.0	0.59	210.9	0.0	18.8	0.47	17.3	0.57
9	200	208	29.9	0.05	21.9	0.29	123.1	0.0	21.7	0.30	21.6	0.30
Total			10		23		0		17		20	

[†]Modified χ^2 test to clip data exceeding $1.5 \times IQR$ and using 10 histogram bins

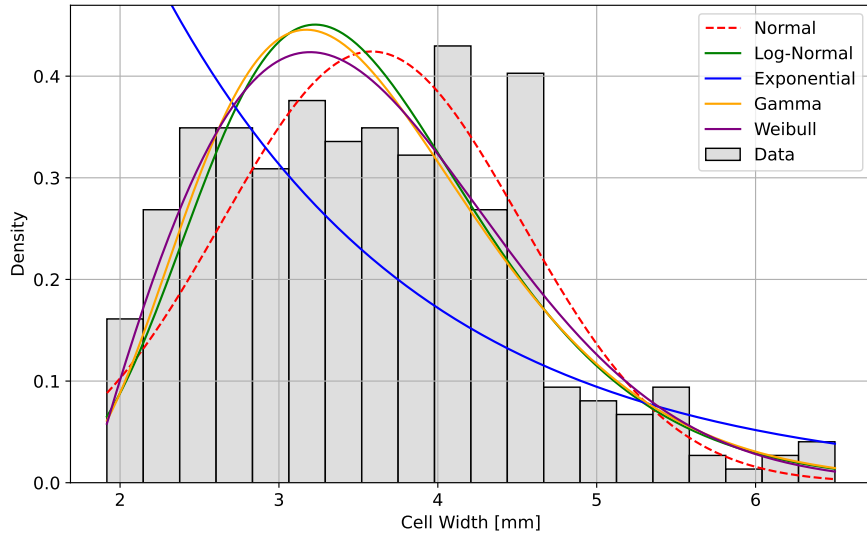


Figure 3.8 – Density histogram of experimental cell size measurements and probability density functions for various distributions for $0.333\text{ H}_2 + 0.111\text{ CH}_4 + 0.111\text{ CO} + 0.444\text{ O}_2$ (Mix 3) at $P_1 = 100\text{ kPa}$

A log-normal distribution is given by two parameters $\mu = \bar{\lambda}$ and σ which are the expected value (mean) and standard deviation of the natural logarithm of the variable. Then the continuous distribution ϵ for the log-normal transformation $\psi = \ln(\epsilon)$ is given by [94]:

$$\epsilon = e^{\bar{\lambda}_\psi + \sigma_\psi Z} \quad (3.8)$$

where Z is the standard normal variable or z-distribution from a normal distribution with $\bar{\lambda} = 0$ and $\sigma = 1$. The mean is the average of all values in the log-normal dataset. For a log-normal distribution, it is calculated by transforming the data to follow a normal distribution by taking the natural logarithm of all points, and then computing the mean of the transformed data ($\bar{\lambda}_\psi$) by [94]:

$$\bar{\lambda}_\psi = \frac{1}{N} \sum_{i=1}^N \ln \lambda_i \quad (3.9)$$

where N is the number of points for the trial, and λ_i is each measured cell size. It is noted that there is no significant difference between the normal distribution and log-normal distribution mean cell size. The largest percent difference is a 3.6% increase for the Mix 1 test at 50 kPa, and with most other differences being less than 1%. Therefore, despite other literature data using a normal average, their data may still be compared to this study's experimental data. The standard deviation measures the spread or dispersion of the data points around the mean. A high standard deviation means that the data points are spread

out widely, while a low standard deviation means they are close to the mean. The standard deviation for the log-transformed data (σ_ψ) is determined by [94]:

$$\sigma_\psi = \sqrt{\frac{1}{N} \sum_{i=1}^N (\ln \lambda_i - \bar{\lambda}_\psi)^2} \quad (3.10)$$

The mean of the original dataset ϵ is then calculated by [98]:

$$\bar{\lambda}_\epsilon = e^{\bar{\lambda}_\psi + \frac{\sigma_\psi^2}{2}} \quad (3.11)$$

where $\bar{\lambda}_\psi$ is the calculated mean of the log-transformed data and σ_ψ^2 is the variance. The expected median of the original dataset is the exponentiated mean of the log data [98]:

$$\tilde{\lambda}_\epsilon = e^{\bar{\lambda}_\psi} \quad (3.12)$$

For this study, the relative standard deviation is presented as a ratio of standard deviation to the mean ($\sigma_\psi/\bar{\lambda}_\psi$) to better compare to the range of cell sizes measured. This would mean that the relative standard deviation of the original dataset is calculated by:

$$\frac{\sigma_\epsilon}{\bar{\lambda}_\epsilon} = \sqrt{e^{\sigma_\psi^2} - 1} \quad (3.13)$$

The mode is the value that appears most frequently in the dataset. Since the peak of the underlying normal is at $\bar{\lambda}_\psi$, and exponentiation skews the data, the mode is shifted left by σ_ψ^2 , hence [98]:

$$\text{Mode}(\epsilon) = e^{\bar{\lambda}_\psi - \sigma_\psi^2} \quad (3.14)$$

Skewness measures the asymmetry of the data distribution. A positive skew indicates a longer right tail, while a negative skew indicates a longer left tail. A skewness of 0 indicates a symmetric distribution. For a log-normal distribution, it is calculated by [98]:

$$\text{Skewness}(\epsilon) = (e^{\sigma_\psi^2} + 2) \sqrt{e^{\sigma_\psi^2} - 1} \quad (3.15)$$

Kurtosis measures the ‘‘tailedness’’ of the distribution. A positive excess kurtosis indicates heavy tails or more outliers, while negative excess kurtosis indicates light tails or fewer outliers. It is determined by [98]:

$$\text{Kurtosis}(\epsilon) = e^{4\sigma_\psi^2} + 2e^{3\sigma_\psi^2} + 3e^{2\sigma_\psi^2} - 6 \quad (3.16)$$

Table 3.4 summarizes these six statistics, as well as the χ^2 and p-value for each trial.

Table 3.4 – Quantitative histogram statistics for the multifuel experimental mixtures from Table 4.2 for a logarithmic normal distribution.

Mix	20 kPa		50 kPa		100 kPa		200 kPa	
1	[16.55, 49.97]		[0.06, 19.74]		[2.19, 14.63]		[1.63, 4.63]	
	32.16	0.25	8.72	0.54	5.24	0.33	2.86	0.23
	31.17	0.78	7.68	1.77	4.97	1.03	2.79	0.70
	29.28	1.10	5.95	6.07	4.48	1.94	2.65	0.88
	-	-	18.62	0.48	30.29	0.05	17.06	0.59
2	[1.86, 34.75]		[2.51, 19.32]		[1.54, 8.24]		[0.42, 4.72]	
	14.19	0.90	6.73	0.36	4.48	0.28	1.77	0.89
	10.56	3.42	6.34	1.13	4.32	0.85	1.32	3.38
	5.85	26.18	5.61	2.34	4.01	1.32	0.74	25.47
	-	-	51.82	0.00	24.91	0.16	-	-
3	[3.26, 26.36]		[1.97, 7.42]		[1.92, 6.50]		no data	
	12.24	0.50	4.28	0.26	3.59	0.27		
	10.94	1.63	4.14	0.79	3.46	0.83		
	8.74	5.08	3.88	1.13	3.23	1.24		
	22.41	0.26	12.69	0.85	40.09	0.00		
4	[10.21, 65.10]		[3.03, 10.72]		[0.57, 7.37]		[1.61, 4.25]	
	22.20	0.42	5.77	0.27	4.32	0.24	2.87	0.19
	20.50	1.32	5.58	0.83	4.21	0.73	2.82	0.57
	17.48	3.24	5.20	1.24	3.98	0.96	2.72	0.58
	-	-	17.28	0.57	17.81	0.05 [†]	9.32	0.41 [†]
5	[12.37, 60.39]		[4.94, 22.39]		[1.86, 13.56]		[2.39, 10.23]	
	42.68	0.49	11.38	0.31	5.92	0.34	5.50	0.29
	38.33	1.59	10.89	0.95	5.62	1.04	5.29	0.89
	30.91	4.79	9.95	1.64	5.05	1.99	4.88	1.44
	-	-	10.79	0.93	26.24	0.12	12.50	0.86
6	[13.63, 81.95]		[6.41, 25.62]		[2.39, 11.52]		[1.04, 5.92]	
	38.46	0.57	11.95	0.29	6.04	0.25	3.22	0.27
	33.34	1.91	11.47	0.90	5.86	0.76	3.11	0.82
	25.06	7.15	10.58	1.46	5.52	1.04	2.90	1.21
	-	-	16.85	0.60	21.97	0.29	23.42	0.22
7	[10.34, 75.59]		[5.95, 26.47]		[1.34, 13.18]		[2.13, 7.34]	
	39.22	0.67	13.63	0.33	8.56	0.31	4.58	0.25
	32.58	2.31	12.93	1.03	8.18	0.95	4.44	0.78
	22.49	10.79	11.65	1.96	7.48	1.64	4.17	1.09
	-	-	30.70	0.04	11.24	0.26 [†]	14.01	0.78
8	[22.34, 54.13]		[36.88, 59.60]		[3.85, 29.44]		[2.93, 10.98]	
	35.72	0.28	47.45	0.18	13.86	0.38	6.33	0.30
	34.42	0.85	46.71	0.54	12.97	1.18	6.07	0.92
	31.97	1.32	45.25	0.53	11.36	2.58	5.58	1.53
	-	-	-	-	28.15	0.08	28.42	0.08
9	[20.31, 43.99]		[4.77, 26.68]		[2.90, 10.48]		[1.61, 4.97]	
	35.35	0.17	11.83	0.34	5.65	0.25	2.97	0.22
	34.87	0.51	11.20	1.06	5.48	0.77	2.90	0.67
	33.92	0.46	10.04	2.05	5.15	1.07	2.76	0.82
	-	-	19.27	0.44	16.97	0.59	21.92	0.29

Cell Layout		
Histogram bin range		
Mean	Rel. Std. Dev.	
Median	Skewness	
Mode	Kurtosis	
χ^2	p-value	

[†]Modified χ^2 test to clip data exceeding $1.5 \times IQR$ and using 10 histogram bins.

3.3.2 Cell Size Measurement Variability

In considering measurement uncertainty and distributions for accurate modelling, it is important to quantify the degree of acceptable variation. While it is commonly accepted that experimental estimates of representative cell size can vary by a factor of two between researchers [14], it is unhelpful in comparing the accuracy of models more finely and tuning them to predict cell size for physical applications.

Measuring cell size more accurately has important implications to applications of physical dimensions. The critical tube diameter and RDE have correlations to diameter based on cell size. The critical tube diameter has been studied to be $\frac{d_c}{\lambda} < 13$ [16] for irregular mixtures, and $\frac{d_c}{\lambda} = [20, 30]$ for regular mixtures diluted with argon [19], [99]. This already shows a factor of two difference, and when compounded with possibly a similar magnitude difference in the measurements of cell size, it becomes increasingly difficult to design based on expected cell sizes. In the RDE, Bykovskii *et al.*'s correlation of 40λ minimum diameter is more untested so efforts should be made to determine more accurate cell size distributions which can then evaluate the mixture's suitability to an RDE.

To help minimize systematic errors in measurements for this study, cell sizes for all trials were measured by two separate researchers, the author (Ayush Gupta) and Alexandre Poyet. Both researchers used the same image and software, so the only variable is the individual's analysis of a cell. Fig. 3.9 shows a difference histogram of the two independent measurements for each trial. In each, the grey represents the overlap where both researchers measured the same normalized frequency and size of cell, and the blue and orange represent where the measurements differed. The data are normalized by the total sample size to eliminate the individual's sample size as a variable. Dashed lines indicate the mean cell size for each researcher's measurements assuming the log-normal distribution.

Fig. 3.9 shows good agreement between the two researchers' cell size measurements across the range of data analyzed. For most initial conditions, the means were almost coincident. The largest discrepancies are seen at low pressure tests (20 kPa) where the sample size is smaller due to larger cells. In these cases, the fewer cells give more weighting to each measurement and thus small variations in measurements lead to greater change in the mean and histogram distribution.

Quantification of the variability of this study's cell size measurements, assuming a log-normal distribution, is important to compare to the generally accepted factor of two difference [14]. Since the log-normal distribution is a normal distribution after transformation, statistical measures like confidence interval and limits of agreement are still valid as for normal distributions. First, the data are transformed from the original to the log space by $\epsilon_1 = \ln \lambda_1$ and $\epsilon_2 = \ln \lambda_2$, where λ_1 was A. Gupta and λ_2 was A. Poyet's original cell measurements. The average cell size was then determined by the average in the log space. The difference of logs ($\Delta\epsilon_i$), which corresponds to the log ratio in the original space

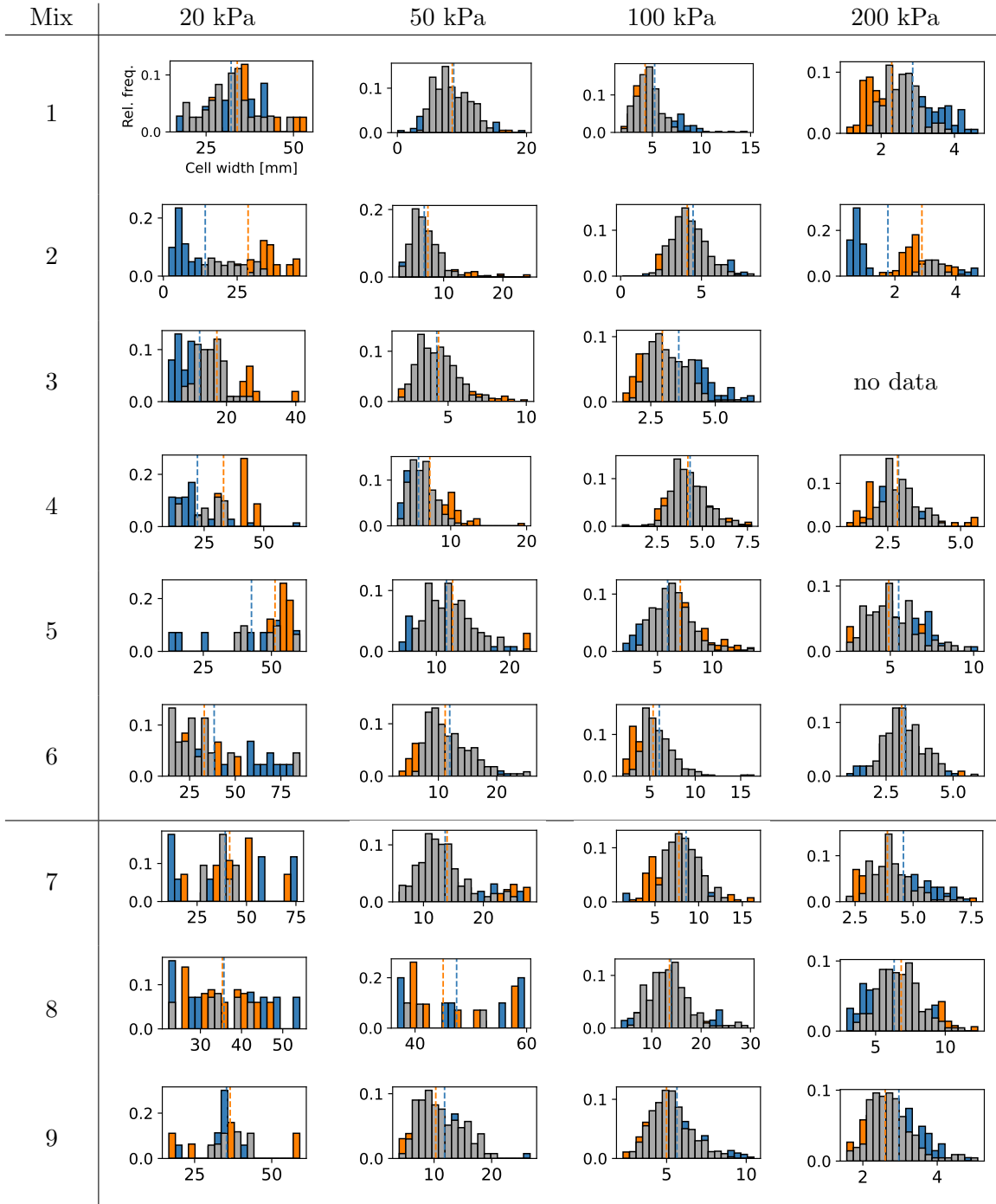


Figure 3.9 – Relative frequency histogram of differential cell size of two independent measurements by A. Gupta (blue) and A. Poyet (orange), overlap shown in grey.

is calculated by:

$$\Delta\epsilon_i = \epsilon_1 - \epsilon_2 = \ln\left(\frac{\lambda_1}{\lambda_2}\right) \quad (3.17)$$

The mean difference between the two authors' average cell size is determined by,

$$\overline{\Delta\lambda} = \frac{1}{N} \sum_{i=1}^N \Delta\lambda_i \quad (3.18)$$

The standard deviation is a measure of the variability of a measurement from the mean. A low standard deviation indicates that most values fall close to the mean and there is low variability, while a high standard deviation indicates a larger spread between the data. It is calculated by,

$$\sigma_{\Delta\lambda} = \sqrt{\frac{1}{N-1} \sum_{i=1}^N (\Delta\lambda_i - \overline{\Delta\lambda})^2} \quad (3.19)$$

The limits of agreement describe the range where 95% of the individual data points fall. For the difference of logs of cell measurements it is calculated by,

$$LoA_{\log} = \overline{\Delta\lambda} \pm 1.96 \times \sigma_{\Delta\lambda} \quad (3.20)$$

A confidence interval refers to the range where the mean of a study is likely to fall with a certain confidence probability. For this study, a 95% confidence interval is selected and calculated in log space by,

$$CI_{\log} = \overline{\Delta\lambda} \pm 1.96 \times \frac{\sigma_{\Delta\lambda}}{\sqrt{N}} \quad (3.21)$$

To effectively display the difference in two researchers' measurements, the variability is converted back to the original units and expressed in a percentage difference scale. The bias as a percent difference is given by the median ratio between the two measurements,

$$PD = (e^{\overline{\Delta\lambda}} - 1) \times 100\% \quad (3.22)$$

The LoAs may be expressed in percent difference form as well by,

$$LoA = \left(e^{\overline{\Delta\lambda} \pm 1.96\sigma_{\Delta\lambda}} - 1 \right) \times 100\% \quad (3.23)$$

Similarly, the CI in percentage scale is calculated by,

$$CI = \left(e^{\overline{\Delta\lambda} \pm 1.96 \frac{\sigma_{\Delta\lambda}}{\sqrt{N}}} - 1 \right) \times 100\% \quad (3.24)$$

The statistical measurements for the multi-fuel mixtures' average cell sizes compared between the two researchers are shown in Table 3.5.

Table 3.5 – Statistical measurements for percentage difference of average cell size measurements by two researchers

Measurement	Description	Value
Max PD	Maximum difference	107.2%
μ_{PD}	Mean difference	-0.8%
σ_{PD}	Standard deviation	23.7%
$CI_{95\%}$	95% confidence interval	[-6.5%,5.3%]
$LoA_{95\%}$	95% limits of agreement	[-34.6%,50.7%]

A Bland-Altman plot is a graphical method used to assess the agreement between two measurement techniques by plotting the difference between paired measurements against their mean. The plot includes a mean difference (bias line), which indicates the average discrepancy between the two researchers, and limits of agreement, typically set at ± 1.96 standard deviations from the mean difference. These limits help visualize the range within which most differences lie, providing insight into measurement consistency and potential systematic bias. If the differences are randomly scattered around the bias line with no clear trend, the two researchers' measurements are considered in good agreement. However, trends or widening LoA may suggest measurement bias or variability dependent on the magnitude of values. A Bland-Altman plot is plotted for the average cell size measurements of Gupta and Poyet in Fig. 3.10. The mean difference and LoA correspond to the same calculated values in Table 3.5.

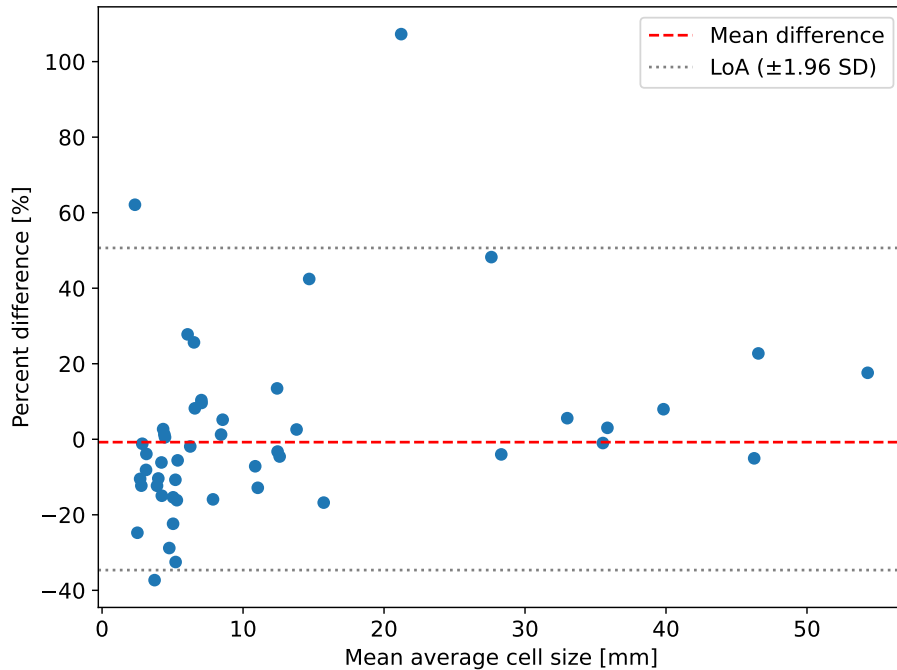


Figure 3.10 – Bland-Altman plot comparing average cell size of two independent experimental measurements of A. Gupta and A. Poyet

The statistical analysis shows that the two researchers have percent differences well below the generally accepted factor of two [14] for average cell size, with a maximum of only 107%. The mean difference is approximately 0%, which shows that the two researchers measured the same average cell size overall considering all trials; however, the data show a high standard deviation, resulting in a true mean varying within -7% to 5% with 95% confidence. As seen on the Bland-Altman plot, the data tend to have no systematic bias between the two measurements and the spread appears fairly random, though 95% of the data fall within the limits of about -35% to 51% showing considerable variability. Fig. 3.10 does show that there is slightly greater difference at smaller mean cell sizes. This may be a result of irregular mixtures having a wide range of cell sizes and that a small difference in measurement results in a greater percentage difference; whereas, a similar absolute size difference at larger mean cells would result in a proportionally smaller percentage difference. The data show that the two researchers are able to measure cell size more precisely than the generally accepted uncertainty. There is also no systematic tendency of one researcher to over- or under-predict compared to the other. This further narrows the acceptable range for which models should be able to predict detonation cell size leading to more accurate modelling for applications. Given this precision in cell size measurement using this technique, the remainder of this thesis uses the cell size measurements by the author only.

Chapter 4

Results

This chapter presents the results obtained from the detonation channel at ENSMA in Poitiers, France and the preliminary results of low-pressure hydrogen/oxygen experiments at RMC's detonation channel.

4.1 ENSMA Detonation Channel

For each trial, pressure traces and soot foils were recorded to calculate the detonation speed in relation to the expected CJ velocity, and measure the detonation cell width. Examples of soot foil scans are shown in Fig. 4.1. On each foil, darker lines indicate the triple point trajectories and form diamond-like patterns which are cells. The cell size measurement for the trial is taken as an average of all the recognizable cell widths on each foil with a histogram shown to show the variance in measurements. The average is calculated by assuming a log-normal distribution. The histograms have 20 evenly sized bins in each case which encompass the entire range of data, and groups similar cell sizes while not removing variability. Fig. 4.2 shows these average cell widths and distributions for each trial conducted as measured by the author, except for 200 kPa Mix 3 where no data were obtained; a red line indicates the mean value which is used as representative to compare to literature data. The complete numerical statistics for the histograms are shown in Table 3.4 including mean, median, mode, standard deviation, skewness, and kurtosis.

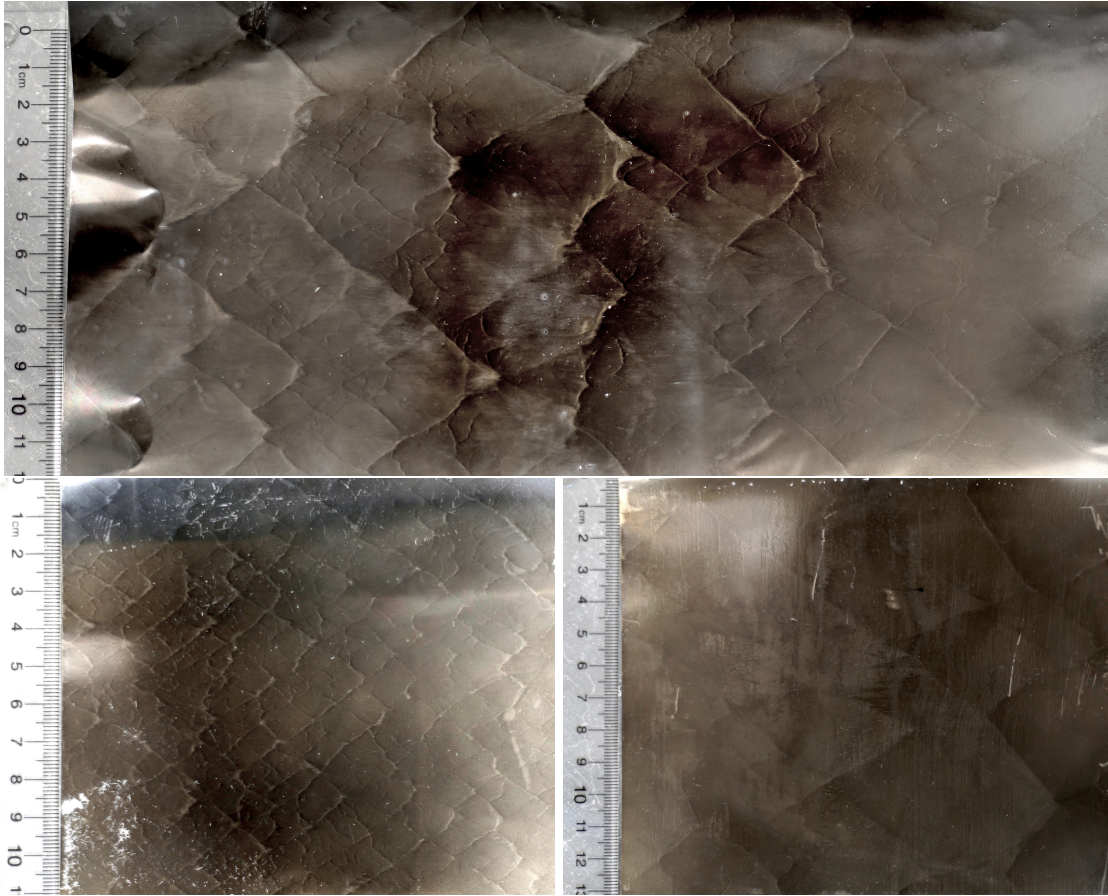


Figure 4.1 – Soot foil images for CJ detonation in cylindrical channel for $0.083\text{H}_2 + 0.250\text{CH}_4 + 0.083\text{CO} + 0.583\text{O}_2$ (Mix 1) at $P_1 = 20.03\text{ kPa}$, $T_1 = 17.4\text{ C}$ (top), $0.083\text{H}_2 + 0.250\text{CH}_4 + 0.083\text{CO} + 0.583\text{O}_2$ (Mix 1) ($P_1 = 49.90\text{ kPa}$, $T_1 = 17.2\text{ }^\circ\text{C}$) (bottom left); $0.095\text{H}_2 + 0.190\text{CH}_4 + 0.190\text{CO} + 0.524\text{O}_2$ (Mix 6) at $P_1 = 20.0\text{ kPa}$, $T_1 = 18.0\text{ }^\circ\text{C}$ (bottom right). Detonation propagates left to right.

The average cell sizes in Fig. 4.2 show the general trend of decreasing cell width with increasing pressure. Moreover, the cell size decreases for all tested pressures as hydrogen fuel fraction increases and with constant carbon monoxide fraction (Mix 1 to 3). The average cell size also increases as carbon monoxide fraction increases from $X_{f,\text{CO}} = \frac{2}{5}$ in Mix 4 to $X_{f,\text{CO}} = \frac{3}{5}$ in Mix 5 with constant methane fuel fraction of $X_{f,\text{CH}_4} = \frac{1}{5}$. Mix 6 shows similar average cell size to Mix 4 which have the same fuel fraction of carbon monoxide ($X_{f,\text{CO}} = \frac{2}{5}$) but greater fuel fraction of hydrogen, contributing to slightly smaller cells. The binary fuel mixtures (Mix 7, 8, and 9) of carbon monoxide and methane have generally larger cells than the other ternary mixtures. In these, the average cell size increases with increasing fuel fraction of carbon monoxide from $X_{f,\text{CO}} = \frac{1}{4}$ to $X_{f,\text{CO}} = \frac{3}{4}$ with the remainder fuel fraction being methane. The detonation velocities are shown in Appendix A for each trial. All velocities are within $\pm 2\%$ of the CJ velocity showing that there is a CJ detonation at the soot foil.

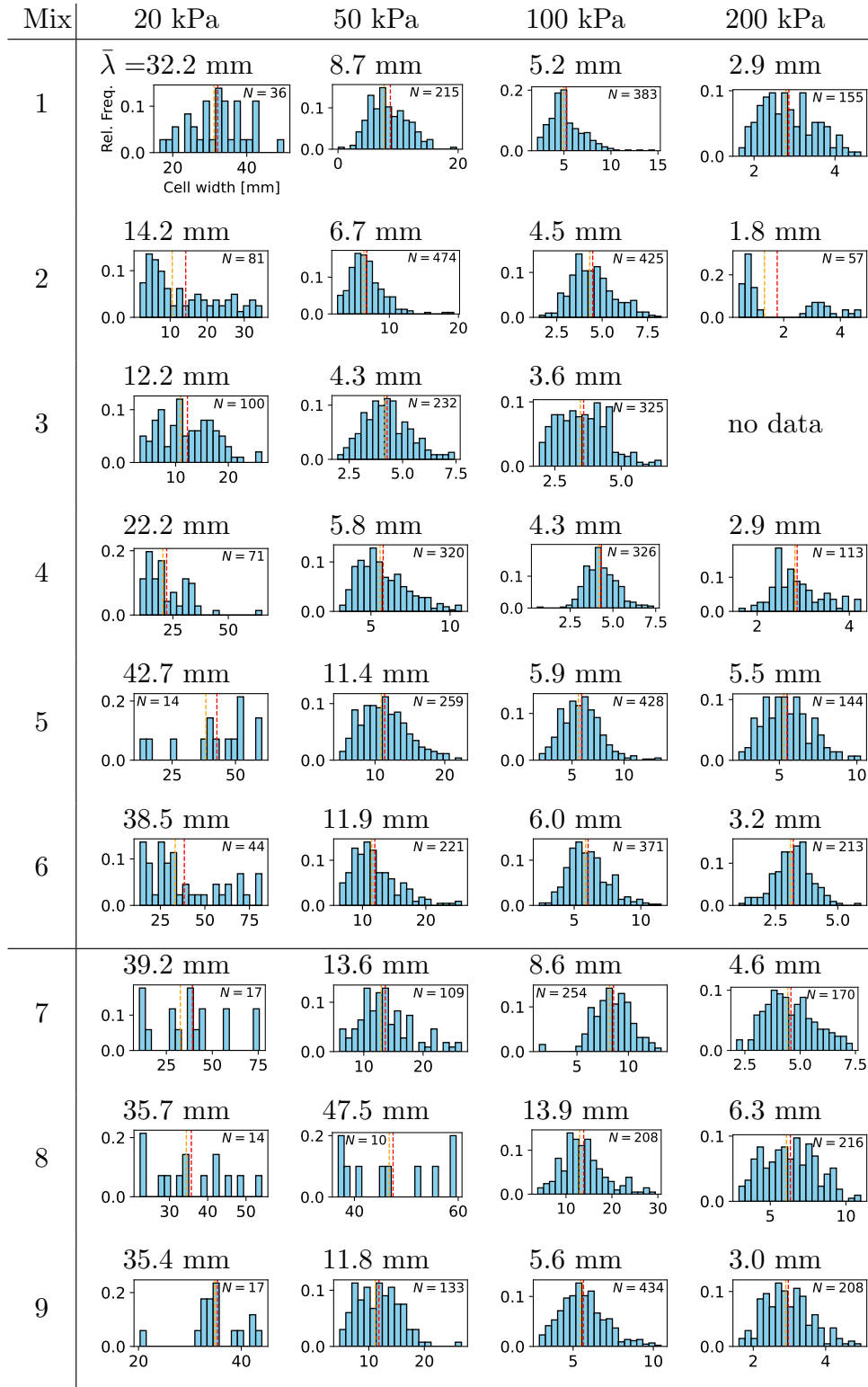


Figure 4.2 – Average cell width and histograms showing the relative frequency of cell size measurements (red line is mean, orange is median)

4.2 RMC Detonation Channel

The rectangular detonation channel at RMC became operational in December 2024 and preliminary testing was done to evaluate the detonation characteristics comparing to well-known literature results. These tests used stoichiometric hydrogen-oxygen mixtures at lower pressures (<20 kPa) to minimize risk. To date, four successful tests have been performed: one at 20 kPa, one at 15 kPa, and two at 12.5 kPa. More tests were done but did not detonate.

The preliminary cell size and velocity data is presented in Fig. 4.3 showing the distribution of cells measured on the same soot foil, and average cell size with a red line. The log-normal χ^2 and p-value is also shown for the distributions, though only the test at 20 kPa shows a significant result supporting this distribution. The velocity is calculated by the average arrival time of the shock at each pressure transducer and known distances between them. An example pressure trace is shown in Fig. 4.4 for the 15 kPa test. The graph also indicates the points used for measuring the velocity as a black 'X' on each trace. These points are selected as where the trace exceeded a certain threshold voltage on the transducer, selected as 0.1 V. Voltage readings corresponding to non-physical pressures below 0 kPa are excluded from the plot. These artifacts result from the AC-coupled nature of the PCB 113B21 piezoelectric pressure transducers, which are designed for dynamic pressure measurements. Following shockwave passage, signal undershoot or baseline drift can occur due to the discharge time constant of the internal Integrated Circuit Piezoelectric amplifier, leading to momentary negative voltages that do not represent real absolute pressure values [100], [101]. The velocity is calculated using the same method as for the ENSMA detonation channel with known physical distances and shock arrival times in Table 4.1. The example calculation in Table 4.1 shows consistent velocity measurements up to the fifth transducer and then a decrease in the last section. This may be due to the protruding soot foil placed in the last 30 cm of the channel creating a 1.6 mm front-facing step which slows the detonation. Using SDToolbox [61], the CJ velocity is calculated for each mixture, and compared to the observed experimental detonation velocity. Note that the two tests performed at 12.5 kPa are combined in the same column, and the measurements of cell width and velocity are very similar between the two trials. Example soot foils are shown in Fig. 4.5.

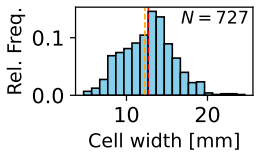
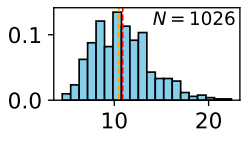
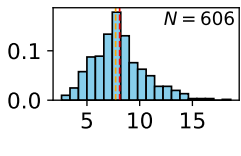
For mix of $2\text{H}_2 + \text{O}_2$	12.5 kPa	15 kPa	20 kPa
Cell width	12.7 mm	10.9 mm	8.1 mm
Rel. Freq.			
Average velocity	2630 m/s	2706 m/s	2702 m/s
$\%D_{CJ}$	97	99	98
Log-norm χ^2 , p-val	34.7, 0.02	41.2, 0.00	25.7, 0.14

Figure 4.3 – Cell width and detonation velocity of stoichiometric hydrogen/oxygen tests at RMC

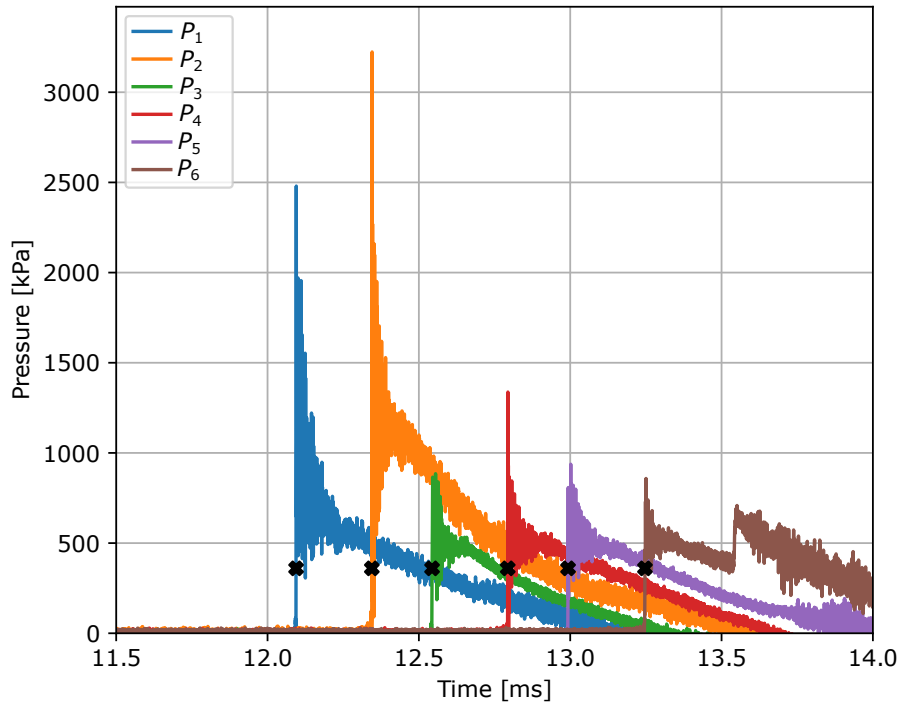


Figure 4.4 – Pressure transducer traces for 15 kPa test of $2\text{H}_2 + \text{O}_2$ at RMC rectangular detonation channel. Traces correspond to pressure transducers at locations shown in Fig. 3.4.

Table 4.1 – Pressure transducer results for $2\text{H}_2 + \text{O}_2$ at $P_1=15\text{ kPa}$, calculation of detonation velocity.

Parameter	$P_1 - P_2$	$P_2 - P_3$	$P_3 - P_4$	$P_4 - P_5$	$P_5 - P_6$
Time between peaks [ms]	0.2503	0.1990	0.2501	0.1993	0.2540
Distance between sensors [cm]	67.89	54.05	67.89	54.05	67.89
Calculated velocity [m/s]	2712.3	2716.1	2714.5	2712.0	2672.8
Average detonation velocity [m/s]	2705.5				

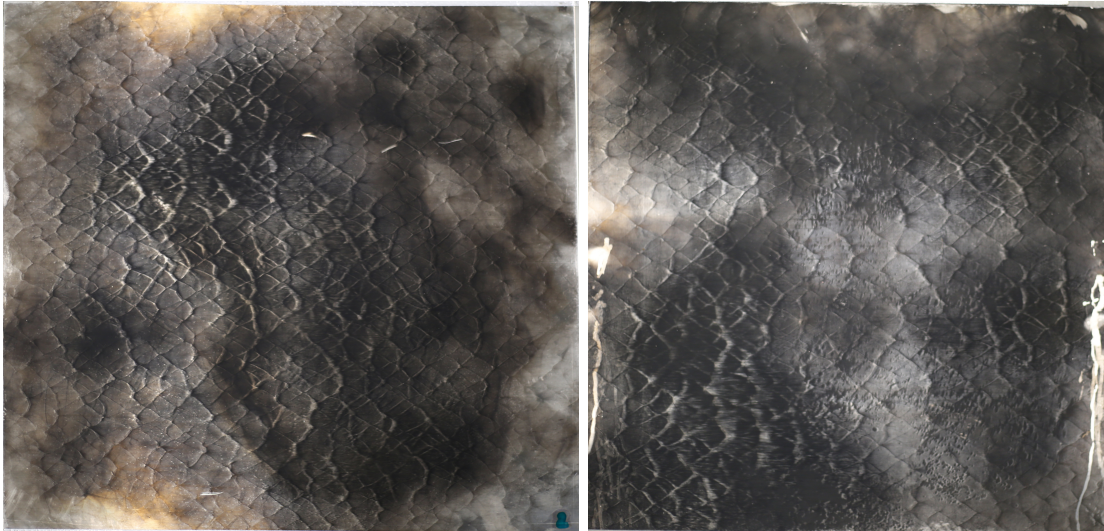


Figure 4.5 – Soot foil images for CJ detonation in rectangular RMC channel for stoichiometric hydrogen/oxygen at $P_1 = 14.99\text{ kPa}$, $T_1 = 20.3\text{ C}$ (left); $P_1 = 12.52\text{ kPa}$, $T_1 = 18.5\text{ }^\circ\text{C}$ (right). Detonation propagates left to right.

Chapter 5

Discussion

The present section compares the experimental results to literature models for cell size. First, the distribution of cell size measurements is analyzed for the experimental trials, showing significant variation within the same soot foil. Second, the new multi-fuel mixtures are compared to five literature models, analyzing their errors, biases, and systematic differences in predictions based on pressure and mixture. Third, the models are evaluated against the broader set of literature data to show levels of consistency within mono-, binary-, and multi-fuel mixtures.

5.1 Experimental Results

The results for the average detonation cell width of each mixture and pressure are presented in Table 4.2. Several key trends can be observed, aligning with established detonation theory and previous binary fuel literature results. The detonation velocities obtained from the pressure transducer and shock pin data are within 2% of the calculated CJ velocity for all trials, indicating a steady CJ detonation at the soot foil; measurements are shown in Table 5.2.

5.1.1 Kinetic and Thermodynamic Calculations

Some key kinetic and thermodynamic parameters are calculated for the experiment initial conditions using SDToolBox [61] to substantiate the discussions. The effective activation energy for the overall reaction is determined by an Arrhenius reaction rate simulation at different temperatures T_1 in SDToolBox by,

$$\ln(t_{\text{reaction}}) = \frac{E_a}{R} \left(\frac{1}{T_1} \right) + \ln K \quad (5.1)$$

solving for E_a/R and the pre-exponential factor K . The results are shown in Table 5.1 using the San Diego mechanism [102]. The detonation velocity is determined by SDToolBox's [61] built-in function shown in Table 5.2. The calculated effective activation energy and CJ detonation velocity increase with increasing pressure across all mixtures.

Table 5.1 – $\frac{E_a}{RT_{vN}}$ calculated for experimental mixtures and pressures

Mixture	20 kPa	50 kPa	100 kPa	200 kPa
0.083 H ₂ + 0.250 CH ₄ + 0.083 CO + 0.583 O ₂ (Mix 1)	5.3	6.0	6.4	6.7
0.190 H ₂ + 0.190 CH ₄ + 0.095 CO + 0.524 O ₂ (Mix 2)	5.2	5.6	5.8	6.1
0.333 H ₂ + 0.111 CH ₄ + 0.111 CO + 0.444 O ₂ (Mix 3)	4.8	4.9	5.0	5.6
0.222 H ₂ + 0.111 CH ₄ + 0.222 CO + 0.444 O ₂ (Mix 4)	5.0	5.1	5.3	5.8
0.111 H ₂ + 0.111 CH ₄ + 0.333 CO + 0.444 O ₂ (Mix 5)	5.2	5.6	5.8	6.2
0.095 H ₂ + 0.190 CH ₄ + 0.190 CO + 0.524 O ₂ (Mix 6)	5.3	5.9	6.2	6.6
0.222 CH ₄ + 0.222 CO + 0.555 O ₂ (Mix 7)	5.2	6.1	6.7	7.2
0.133 CH ₄ + 0.400 CO + 0.466 O ₂ (Mix 8)	5.3	6.2	6.8	7.3
0.286 CH ₄ + 0.095 CO + 0.619 O ₂ (Mix 9)	5.1	6.0	6.6	7.1

Table 5.2 – D_{CJ} [m/s] calculated for experimental mixtures and pressures

Mixture	20 kPa	50 kPa	100 kPa	200 kPa
0.083 H ₂ + 0.250 CH ₄ + 0.083 CO + 0.583 O ₂ (Mix 1)	2271	2310	2340	2370
0.190 H ₂ + 0.190 CH ₄ + 0.095 CO + 0.524 O ₂ (Mix 2)	2292	2332	2362	2393
0.333 H ₂ + 0.111 CH ₄ + 0.111 CO + 0.444 O ₂ (Mix 3)	2332	2373	2404	2434
0.222 H ₂ + 0.111 CH ₄ + 0.222 CO + 0.444 O ₂ (Mix 4)	2173	2210	2238	2267
0.111 H ₂ + 0.111 CH ₄ + 0.333 CO + 0.444 O ₂ (Mix 5)	2042	2077	2103	2130
0.095 H ₂ + 0.190 CH ₄ + 0.190 CO + 0.524 O ₂ (Mix 6)	2174	2211	2239	2268
0.222 CH ₄ + 0.222 CO + 0.555 O ₂ (Mix 7)	2127	2163	2191	2219
0.133 CH ₄ + 0.400 CO + 0.466 O ₂ (Mix 8)	1972	2005	2031	2056
0.286 CH ₄ + 0.095 CO + 0.619 O ₂ (Mix 9)	2237	2276	2306	2335

The ZND induction length is calculated by SDToolBox's [61] ODE integration and using the San Diego mechanism [102] for the experiment initial conditions. The calculated data are shown in Table 5.3.

Table 5.3 – ZND induction length using San Diego mechanism [102] for experimental mixtures and pressures, Δ_i [mm]

Mixture	20 kPa	50 kPa	100 kPa	200 kPa
0.083 H ₂ + 0.250 CH ₄ + 0.083 CO + 0.583 O ₂ (Mix 1)	0.145	0.057	0.028	0.014
0.190 H ₂ + 0.190 CH ₄ + 0.095 CO + 0.524 O ₂ (Mix 2)	0.080	0.032	0.017	0.017
0.333 H ₂ + 0.111 CH ₄ + 0.111 CO + 0.444 O ₂ (Mix 3)	0.042	0.017	0.009	0.051
0.222 H ₂ + 0.111 CH ₄ + 0.222 CO + 0.444 O ₂ (Mix 4)	0.059	0.024	0.013	0.007
0.111 H ₂ + 0.111 CH ₄ + 0.333 CO + 0.444 O ₂ (Mix 5)	0.110	0.046	0.024	0.013
0.095 H ₂ + 0.190 CH ₄ + 0.190 CO + 0.524 O ₂ (Mix 6)	0.143	0.057	0.029	0.015
0.222 CH ₄ + 0.222 CO + 0.555 O ₂ (Mix 7)	0.393	0.146	0.069	0.033
0.133 CH ₄ + 0.400 CO + 0.466 O ₂ (Mix 8)	0.590	0.223	0.107	0.052
0.286 CH ₄ + 0.095 CO + 0.619 O ₂ (Mix 9)	0.284	0.105	0.050	0.024

5.1.2 Pressure and Mixture Trends

First, as supported by literature, increasing pressure leads to a decrease in detonation cell size following a power law. This trend is evident across all tested mixtures, as higher pressures promote molecule collisions enhancing reaction rate, reducing the characteristic cell width. The physical basis for this lies in the increased collision frequency of reactive species, which accelerates ignition reducing the reaction zone length, and strengthens the shock-reaction coupling within the detonation front [14]. The correlation of pressure to cell width follows a power law of $\lambda = aP_1^b$ which is calculated for the mixtures in Table 5.4. In general, the mixtures tested follow a decreasing trend where $b \approx -1$ for all mixtures but have different values of a . This aligns with literature data for other mixtures that show a similar strong exponential decrease trend but there is no simple method to predict the coefficient a .

Table 5.4 – Correlations for mixture trends with pressure and cell width following the equation $\lambda = aP_1^b$ for experimental mixtures tested

Mixture	a	b
0.083 H ₂ + 0.250 CH ₄ + 0.083 CO + 0.583 O ₂ (Mix 1)	1106	-1.19
0.190 H ₂ + 0.190 CH ₄ + 0.095 CO + 0.524 O ₂ (Mix 2)	149	-0.81
0.333 H ₂ + 0.111 CH ₄ + 0.111 CO + 0.444 O ₂ (Mix 3)	133	-0.81
0.222 H ₂ + 0.111 CH ₄ + 0.222 CO + 0.444 O ₂ (Mix 4)	666	-1.14
0.111 H ₂ + 0.111 CH ₄ + 0.333 CO + 0.444 O ₂ (Mix 5)	1967	-1.29
0.095 H ₂ + 0.190 CH ₄ + 0.190 CO + 0.524 O ₂ (Mix 6)	3799	-1.45
0.222 CH ₄ + 0.222 CO + 0.555 O ₂ (Mix 7)	735	-0.99
0.133 CH ₄ + 0.400 CO + 0.466 O ₂ (Mix 8)	188	-0.50
0.286 CH ₄ + 0.095 CO + 0.619 O ₂ (Mix 9)	1120	-1.15

While trends with initial pressure strongly influence detonation cell size, it is also important to consider the potential influence of channel geometry on wave structure at the low pressure trials. At sufficiently low pressures, where cell sizes increase, there is a possibility that the detonation structure could become constrained by the channel dimensions, resulting in mode locking; however, this was not observed in the present experiments. Across all conditions, soot foils as shown in Fig. 4.1, consistently showed multiple distinct cell tracks distributed across the full channel circumference, with no evidence of synchronization or repeated propagation modes. The cellular structures were spatially irregular, and the measured cell sizes exhibited a broad distribution, as shown in the histograms presented in Table 4.2. Furthermore, the average cell sizes did not correspond to any rational fraction or multiple of the channel diameter, indicating that the detonation was not geometrically constrained. These observations collectively suggest that the detonation remained in a non-locked, multi-mode regime across all tested conditions.

Second, the composition of the mixture plays a critical role in determining the cell size, as different fuels exhibit distinct reactivity characteristics. Increasing the hydrogen fraction leads to a marked decrease in cell size, as seen in mixtures 1 through 3, and 4 through 6 in Table 4.2. Hydrogen-rich mixtures have a high CJ detonation speed compared to mixtures with less hydrogen (Table 5.2). Conversely, increasing the proportion of methane results in a significant increase in detonation cell size, as observed in mixtures 1, 5, 6, and 7, 8, 9. This aligns with a previous study by Zhang *et al.* [45] which analyzed cell size of different proportions of methane-hydrogen mixtures. Moreover, Fig. 2.2 also shows that methane-oxygen mixtures have larger cell size across all pressures compared to hydrogen-oxygen.

Fig. 5.1 shows the change in cell size while holding one of the ternary fuel fractions constant and varying the remaining fuel fraction of the other two constituent fuels and comparing to literature data. Fig. 5.1(a) shows the change in cell size with varying methane and carbon monoxide fuel fraction while maintaining 20% fuel fraction of H_2 , while Fig. 5.1(b) varies the carbon monoxide and hydrogen fuel fractions for a constant 20% methane fuel fraction. The plot combines the experimental data for ternary mixtures with the literature data for binary mixtures. Since each plot has a constant fuel fraction of one of the ternary fuels, the remaining binary fuel fraction is indicated on the two x -axes. The right-most points contain the binary fuel mixtures for 20% H_2 and 80% CH_4 on Fig. 5.1(a), and 20% CH_4 and 80% CO on Fig. 5.1(b) for stoichiometric mixtures with oxygen. The remaining dots are experimental measurements that contain varying levels of the third fuel. The colours indicate different initial pressures. Trend lines are drawn by using a least squares regression for the points of each pressure range. The two graphs show that there is a decreasing trend of cell width for increasing methane and decreasing carbon monoxide ratio at constant 20% hydrogen fraction, as well as a decreasing cell size for increasing fraction of hydrogen and decreasing carbon monoxide at constant 20% methane. There is also agreement of these trends of decreasing cell width across the range of pressures. For example, the cell widths decrease by 30% at low pressure and 60% at higher pressure in Fig. 5.1(a) across the range of methane fraction of 25% to 100%. Similarly, for increasing hydrogen fraction from 25% to 100% keeping methane at 20% in Fig. 5.1(b), the cell width decreases by 75%.

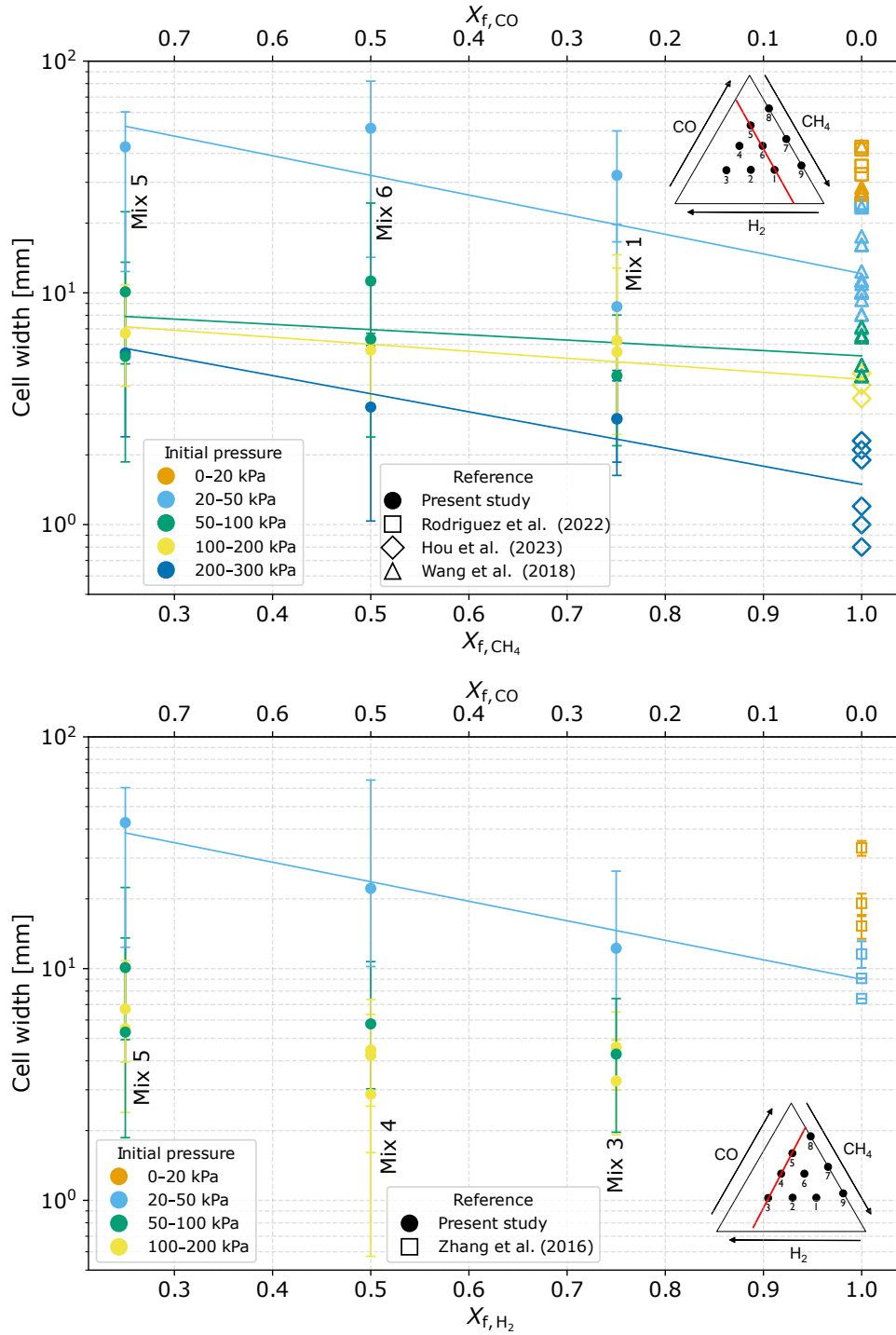


Figure 5.1 – Cell width variation with changing fuel fraction of ternary fuel mixture and pressure for (a) $X_{f,H_2} = 0.2$ (top) and (b) $X_{f,CH_4} = 0.2$ (bottom). Repeated points correspond to different experimental trials, and error bars indicate observed min and max cell sizes. References: Rodriguez *et al.* (2022) [46], Hou *et al.* (2023) [47], Wang *et al.* (2018) [49], Zhang *et al.* (2016) [45].

The role of carbon monoxide in detonation propagation is more nuanced for ternary mixtures. As the CO fraction increases, the resulting detonation cell sizes tend to fall between those observed in hydrogen-rich and methane-rich mixtures. This trend is evident when comparing the average cell sizes of mixtures 1, 3, and 5, which represent the highest fuel mole fractions of methane, hydrogen, and CO, respectively. Although CO contributes significantly to the overall heat release during detonation, its oxidation kinetics are slower than those of hydrogen but faster than those of methane, resulting in intermediate reactivity and corresponding detonation cell sizes. This behavior is consistent with calculated induction zone lengths in Table 5.3, which place CO-rich mixtures between hydrogen-rich and methane-rich cases in terms of reactivity. Prior experimental studies by Austin and Shepherd [103] tested CO detonations in the presence of small fractions of other hydrocarbons, finding that the dominant mechanism depended on the generation of hydroxyl molecules, requiring hydrogen-containing species which readily decompose to form the OH molecule. Fig. 5.2 shows the three CO-CH₄ binary mixtures of this study at the different test pressures, along with literature data for pure methane-oxygen mixtures. The data appears to follow a straight line on the semi-logarithmic plot which indicates an exponential trend between the binary mixtures of varying carbon monoxide-methane fraction to the methane mono-fuel literature data across the ranges of pressure. This shows a trend between varying amounts of carbon monoxide to methane mixtures from 0-75% CO in methane. Austin and Shepherd [48] found that mixtures containing 10-70% CO had no significant variation in cell width, though cell size increased after 75% CO when in binary fuel mixtures with hydrocarbons; indicating that CO acts as an inhibitor. This may be evident in the present study's binary mixture tests of methane-CO as well. For example at 50-100 kPa, there is little change between mixture 7 and 9 containing 50% and 25% CO respectively; however, a greater change in cell size at 75% CO for mixture 8. Further experiments at RMC's detonation channel could be done to evaluate this trend further at low pressures. These trends highlight the complex interplay between pressure, fuel composition, and detonation cell size.

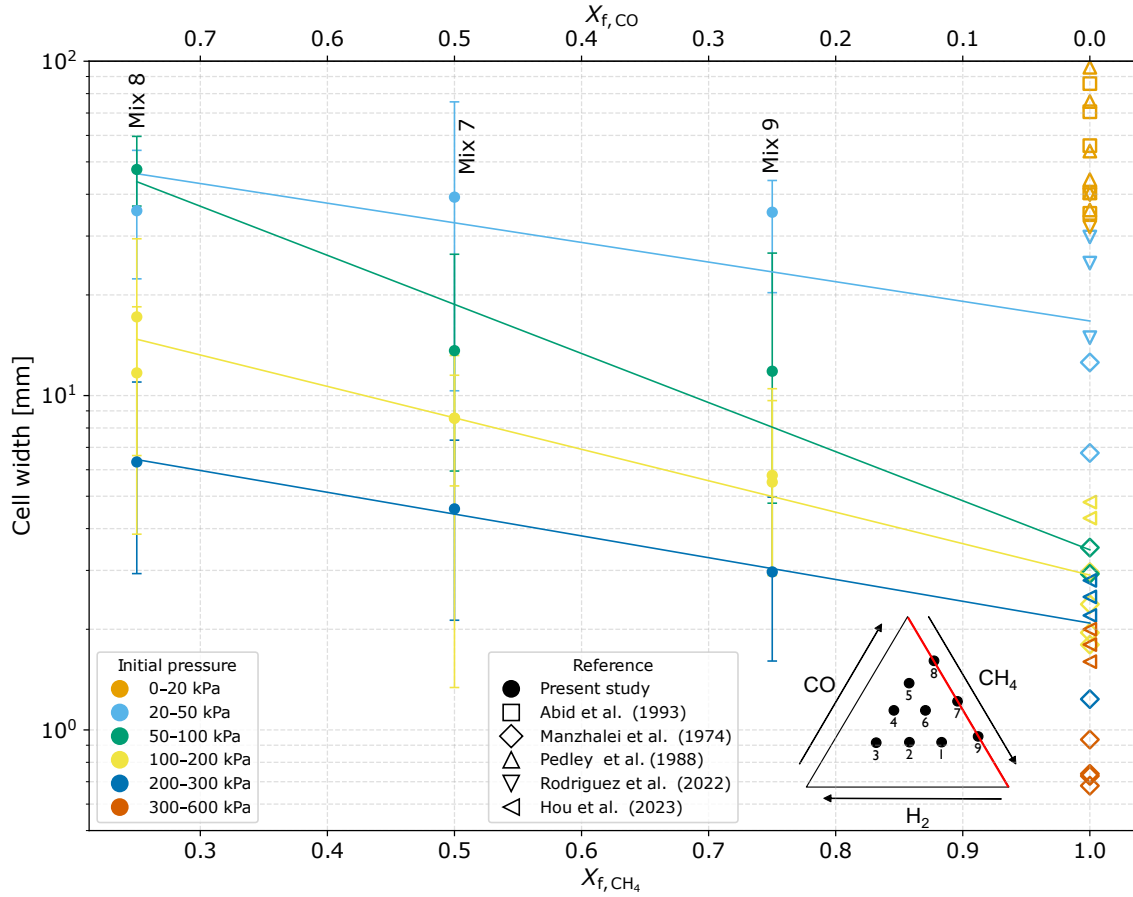


Figure 5.2 – Cell width variation with changing fuel fraction of binary CO-CH₄ mixture at different pressures. Repeated points correspond to different experimental trials, and error bars indicate observed min and max cell sizes. References: Abid *et al.* (1993) [56], Manzhalei *et al.* (1974) [63], Pedley *et al.* (1988) [57], Rodriguez *et al.* (2022) [46], Hou *et al.* (2023) [47].

5.1.3 Cell Size Measurement Distribution

The histograms in Table 4.2 provide a more detailed picture of the distribution of detonation cell sizes. The red dashed line in each plot marks the log-normal mean cell width (μ_ϵ) and the orange is the log-normal median ($\bar{\lambda}_\epsilon$), but the actual data reveal a broader variability in cell sizes within the same test. This highlights the importance of analyzing the full distribution rather than relying solely on a single statistical measure. Most literature results tend to use the mean as the representative cell size of a test, though plotting the median along with the distribution shows an interesting trend. In most cases, the mean and median are very similar; however, in tests with fewer cells to measure, there is greater absolute variability leading to a wider spread of data and a larger difference between the mean and median. In most histograms, it is seen that the mean is greater than the median which is indicative of a right-skewed distribution, further confirming the use of

the log-normal distribution. For this dataset, the difference between mean and median is not large and the mean is used as representative of the cell size to compare with literature data better and encompass the entire range of data analyzed.

Most histograms exhibit a right-skewed distribution, where the highest frequency of measurements is concentrated near the mean, but there are outliers at larger cell sizes. As seen in the example soot foils in Fig. 4.1 and Fig. 4.5, while most of the detonation structure follows a dominant cell size, sporadic instances of larger cells occur; Lee [14] suggests this is due to temporary weakening of transverse waves or fluctuations in reaction front strength. The spread of the distribution varies significantly across mixtures and pressures seen by the inconsistent distribution shapes in Table 4.2. The standard deviations normalized by mean, in Table 3.4, show values ranging from 17% to 90%, with lower standard deviations typically at higher pressure tests. For example, Mix 2 at 20 kPa had a mean cell size of 14.2 mm but a standard deviation of 12.8 mm showing a deviation that is 90% of the mean value; this is visually seen by the flatter histogram; the soot foil had fewer cells to count and large variability in width. Contrarily, Mix 4 at 200 kPa, has a standard deviation that is only 19% of the mean value indicating a more peaked histogram; the foil at the high pressure test had many small cells to measure and less variability was seen. There are noticeable anomalies like Mix 9 at 20 kPa which had the lowest normalized standard deviation of 15% though the histogram does show a large range of cell sizes.

The distributions seen have a dependence on pressure and mixture. A 1-D ZND calculation is done to determine the induction length in Fig. 5.3. This was done for ternary mixtures 1, 3, and 5 which had the highest fraction of methane, hydrogen, and carbon monoxide respectively and at the lowest pressure of 20 kPa and highest of 200 kPa. The induction zone length is defined as the distance from the shock to the point of maximum temperature gradient as seen in Fig. 5.3 representative for $2\text{H}_2+\text{O}_2$ mixture at 20 kPa. The induction zone is the distance before the heat release occurs. The calculations show that the induction length decreases substantially with increasing pressure. Moreover, the mixtures with highest hydrogen fraction have a shorter induction length at both pressures. The difference in induction length by mixture is more substantial at low pressure where the high carbon monoxide mixture has a much longer induction length than at high pressure, and while they were almost coincident at high pressure, at 20 kPa the high methane mixture has a much longer induction length.

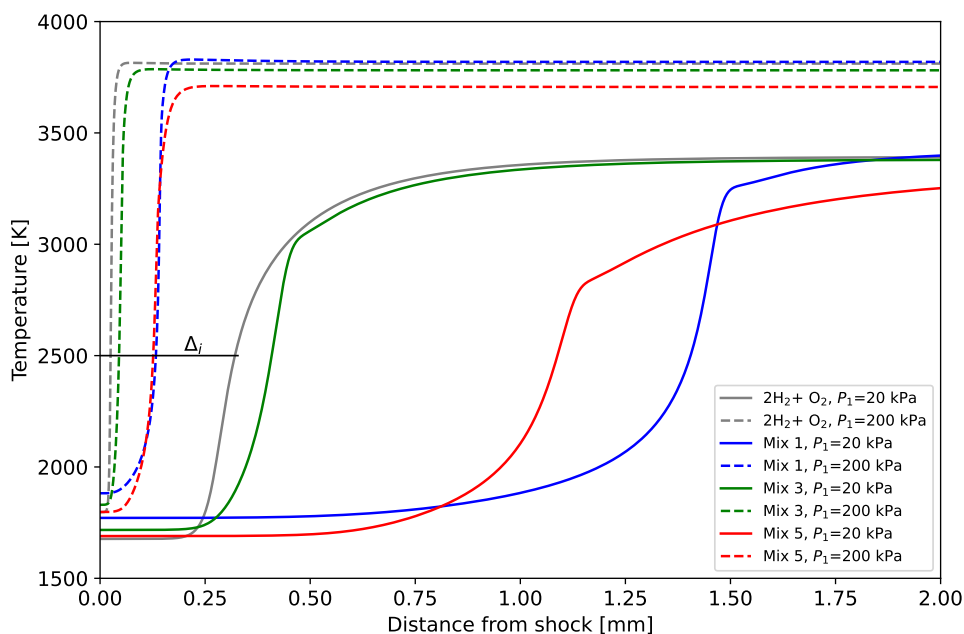


Figure 5.3 – ZND temperature profiles for sample mixtures of $2\text{H}_2+\text{O}_2$, Mix 1, 3, and 5 at $P_1 = 20\text{ kPa}$ and $P_1 = 200\text{ kPa}$, $T_1 = 293\text{ K}$ using San Diego mechanism [102].

For small induction length, high-pressure mixtures, such as those rich in hydrogen (e.g., mixtures 1-3), the cell size distributions tend to be narrow and tightly clustered around the mean. Higher pressures increase reaction rates and reduce the induction length as shown in Fig. 5.3, leading to smaller detonation cells as shown by Shchelkin and Troshin [1]. Also, a higher number of cells per unit area provides a larger sample size, reducing statistical variance. In contrast, mixtures with longer induction lengths (such as those with higher methane or carbon monoxide fractions, e.g., mixtures 5, 8, and 9) show broader distributions with greater variance. Zhang *et al.* cited seeing irregular cell structures for a variety of methane-hydrogen-oxygen mixtures as well [45]. Larger detonation cells, such as mixtures 5-9 at 20 kPa have more variability shown by an indiscernible distribution, as each individual measurement represents a larger fraction of the total sampled area. More tests should be conducted at lower pressures to obtain a statistically significant sample size and distribution.

In several cases, nested cells influence the distribution of cell sizes seen on the histogram. For example, in Fig. 4.1 for Mix 1 at $P_1 = 20\text{ kPa}$, it can be seen that there are smaller cells inside a bigger dominant cell. The larger cell tends to prevail in frequency when analyzing the entire foil; however, these smaller nested cells are still counted by the two researchers. When analyzing soot foils, it is difficult to recognize if the embedded smaller cells are related to the mixture irregularity or other phenomena which would create a variable cell size across the foil.

Another interesting anomaly appears in some methane-rich mixtures (e.g., mixtures 8

and 9 at lower pressures), where the histogram is more evenly spread rather than concentrated around a dominant mode. Methane’s known irregular cell structure may contribute to this [45], but are also a result of the larger and fewer cells resulting in greater measurement variance. This sparse histogram is not apparent at higher pressures where a greater number of cell measurements provides a more normal distribution. Additional tests are needed at the lower pressures to determine if the cells fall into a log-normal distribution with increasing sample size.

For trials with a statistically significant number of cells measured, these histograms demonstrate that detonation cell size follows a log-normal distribution rather than a single value. While the mean cell size remains a useful benchmark, the actual distribution of cell sizes reveals how pressure and fuel composition influence the detonation cell pattern. The confidence in the mean cell size is highest for conditions with more frequent sampling (small cells, high pressure, fuels containing high fraction of hydrogen) and lowest for conditions where cell counts are fewer (large cells, low pressure, lower fraction of hydrogen). Since each test takes over one hour to complete, performing additional experiments for the same initial conditions is beyond the scope of this study’s resources. As well, some distributions were markedly not log-normal, and therefore the mean or median should not be used. A right-skewed, log-normal distribution is generally expected since negative values are impossible, and for a given area, there are a greater number of small cells that can be measured than larger ones. The commonly used factor of two uncertainty [14] is only consistent with the observed spread of cell sizes for some of these experimental histograms, reinforcing the need for careful interpretation of experimental results. Therefore, this study recommends that predictive models should incorporate statistical distributions of cell size, rather than a single value.

5.2 Experimental Data Model Comparison

This section compares the experimental data obtained for the mixtures comprised of hydrogen, carbon monoxide, and methane to predictions by the studied models. For every chemical kinetic calculation, SDToolBox [61] was used with the San Diego mechanism [102] as it was the most applicable to the range of mixtures used in this study. Shchelkin and Troshin [1] propose that the cell width for a specific mixture varies by a constant scaling factor of induction length. Using the average cell size data obtained experimentally, these scaling factors are plotted for each mixture and superimposed on a ternary plot of induction length at 100 kPa in Fig. 5.4. The contours on the plot show that the induction length calculated by the ZND model varies by orders of magnitude across the range of mixtures tested. The longest induction length is in mixtures with higher mole fraction of carbon monoxide and methane, while the shortest is in mixtures high in hydrogen. The ratio λ/Δ_i generally increases as Δ_i decreases and tends to increase with hydrogen fraction as well. This was apparent for binary and ternary mixtures. There were no significant changes in λ/Δ_i with change in pressure. Literature estimates λ/Δ_i as typically 35 for fuel-oxygen mixtures [104], but it can vary from 10 to 50 for common fuel-air mixtures at stoichiometric

composition, and it has even greater variation for diluted mixtures [72]. The experimental results from this study found similar values on the lower end of these typical ranges for λ/Δ_i of 11.5-32.3. The induction length calculation is subject to variations in chemical reaction mechanism. Since there is no simple relation between fuel quantities and the variation of λ/Δ_i in the ternary fuels and the correlation for λ/Δ_i is dependent on mixture, estimating the cell size based on induction length alone is not accurate for new untested mixtures. However, having done these experiments, the scaling factor λ/Δ_i is now known for these mixtures based on the San Diego mechanism. Thus, the average factor of all the ternary fuels, $\lambda/\Delta_i = 20.8$, is used as an *ex post facto* model to compare to the prediction models. The relationship between each of the experimental mixtures and pressures to this *ex post facto* model is shown in Fig. 5.5, with a moderate correlation and 76% of the points falling on the model line while considering measurement variation. The figure shows that the correlation is fairly accurate for most mixtures and pressures, with the greatest outliers seen at the 20 kPa tests.

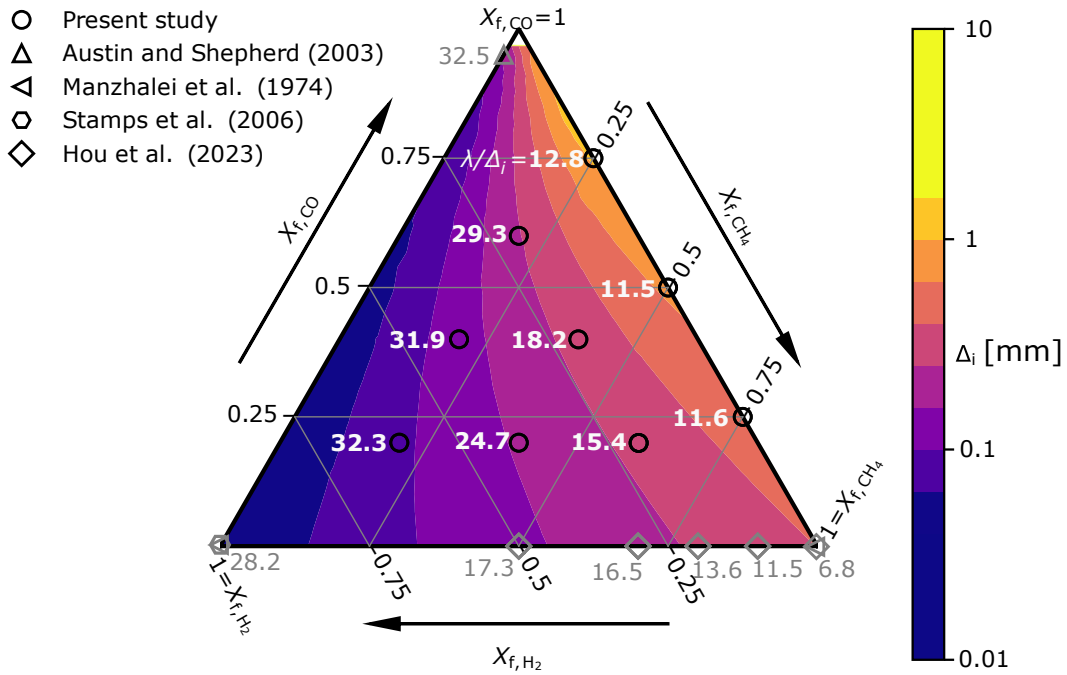


Figure 5.4 – Ternary plot of Δ_i contours using San Diego mechanism [102] and averaged λ/Δ_i (notated numbers) of stoichiometric, undiluted methane, hydrogen, carbon monoxide fuel blends at $P_1=100$ kPa. References: Austin and Shepherd (2003) [48], Manzhalei *et al.* (1974) [63], Stamps *et al.* (2006) [51], Hou *et al.* (2023) [47].

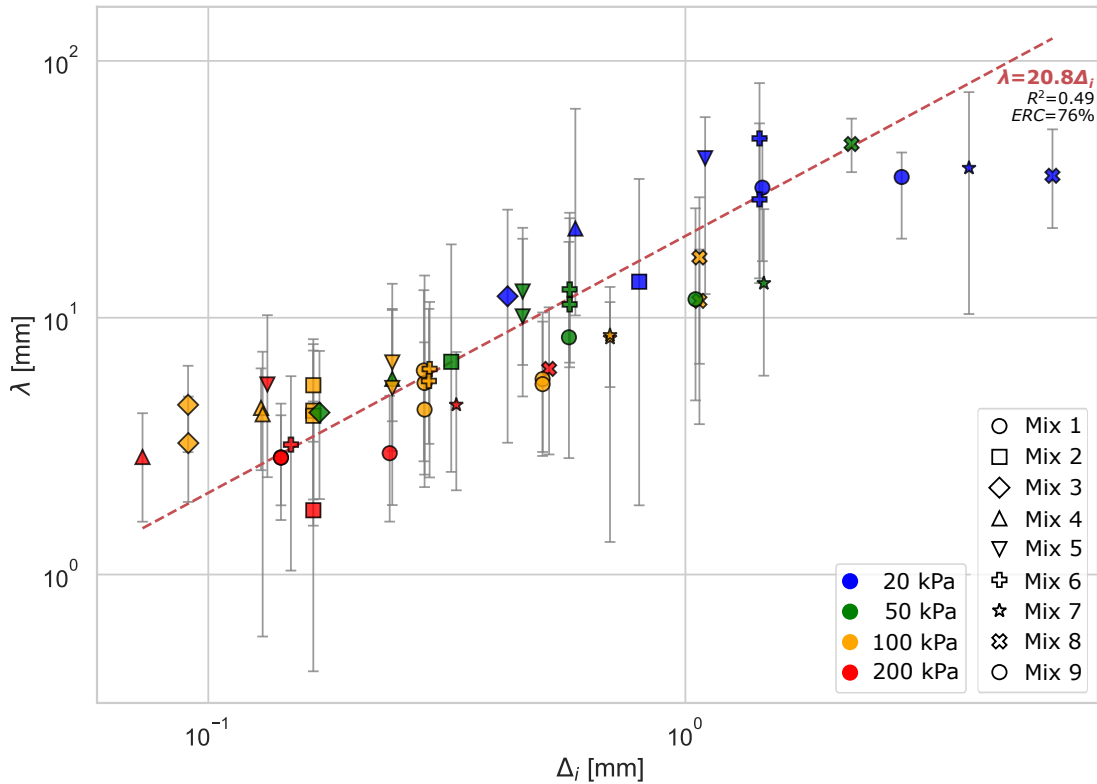


Figure 5.5 – Correlation between experimental cell width and calculated induction length using San Diego mechanism [102], with line of $\lambda = 20.8\Delta_i$

The models of Gavrikov *et al.* [2], Ng [3], Bakalis *et al.* [4], and Monnier *et al.* [5] are used to predict the detonation cell size based on initial conditions and compare against the experimental average cell sizes for the mixtures tested in this study. Histograms show the distribution and frequency of the percentage error for each model in Fig. 5.6. The data shows several interesting trends. First, the predictions by Gavrikov *et al.*'s model have the greatest percentage error with bins up to 600% error and the minimum around 2%. Meanwhile, model of Ng and the *ex post facto* model $\lambda/\Delta_i = 20.8$ have smaller maximum error up to 200%. The best performing model overall is Bakalis *et al.*'s which has error only up to 90%, well within the generally accepted factor of two measurement uncertainty for cell size [14], though not the uncertainty determined by the researchers' measurement variation. Second, the frequency variation shows the distribution of errors across the models. Gavrikov *et al.*'s and Ng's models show a fairly even distribution of error with similar frequency across their range, while Bakalis *et al.*'s and Monnier *et al.*'s have the greatest frequency near the highest error bin. The flatter distribution indicates that the model is more erratic and may predict some mixtures or pressures better than others, whereas the skewed distribution may indicate a more systematic error that consistently over- or underestimates. Further analysis with respect to pressure and mixture reveals the more nuanced aspects of model prediction.

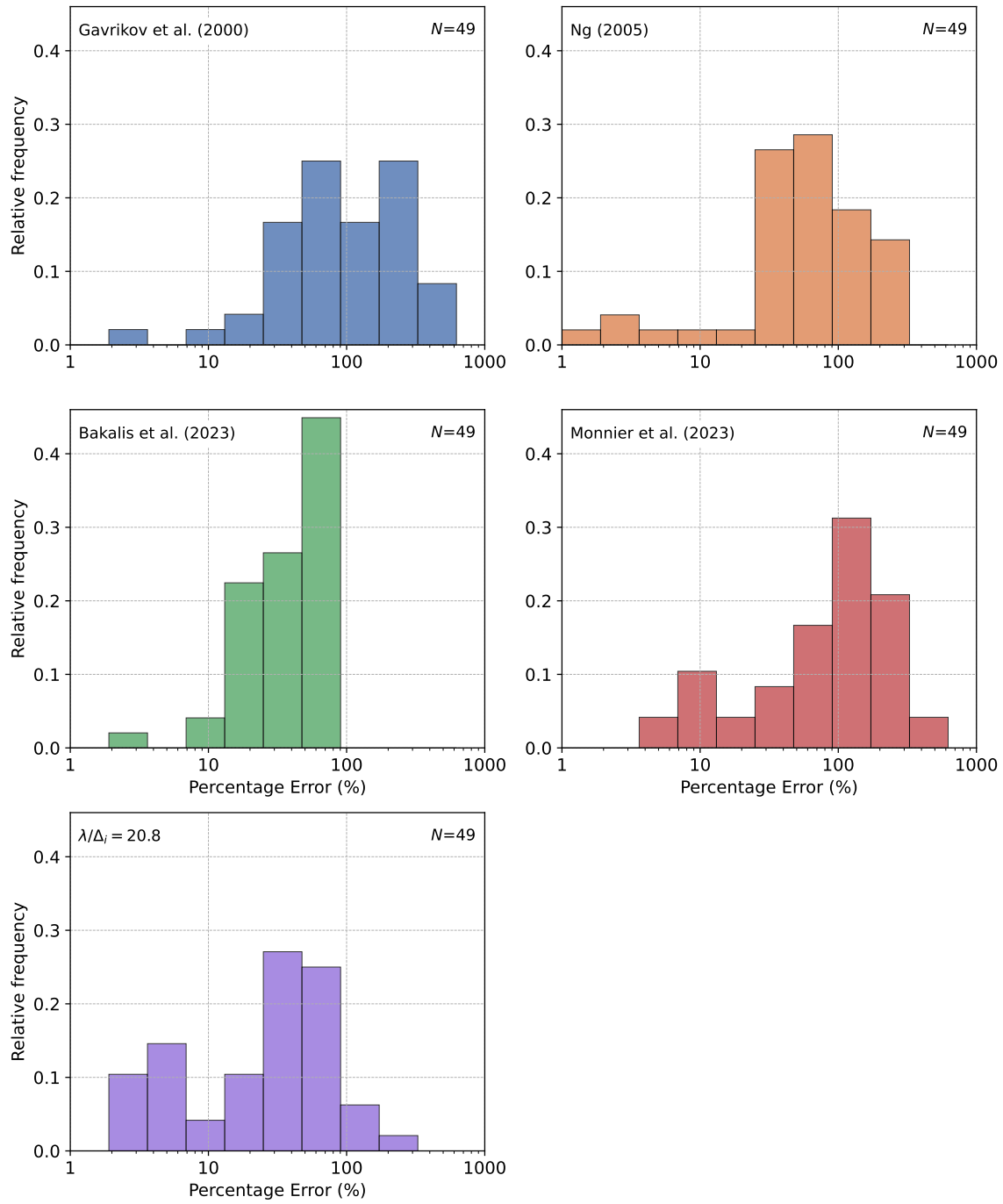


Figure 5.6 – Relative frequency of percent error of average cell size by model for all experimental test mixtures

A box plot visually represents the distribution of a dataset using five key statistics: the minimum, first quartile (Q_1), median (Q_2), third quartile (Q_3), and maximum. The box spans from Q_1 to Q_3 , showing the interquartile range (IQR), which captures the middle 50% of the data. The median (Q_2) is marked within the box, indicating the dataset's central tendency. These quartiles are calculated by the following equations for a sorted dataset:

$$Q_2 = \text{Median} = \tilde{\lambda} = \lambda_{(\frac{N+1}{2})} \quad (5.2)$$

$$Q_1 = \lambda_{(\frac{N+1}{4})} \quad (5.3)$$

$$Q_3 = \lambda_{(\frac{3(N+1)}{4})} \quad (5.4)$$

$$IQR = Q_3 - Q_1 \quad (5.5)$$

The whiskers extend to the minimum and maximum values within $1.5 \times IQR$ from Q_1 and Q_3 , respectively, helping to identify spread and variability. The lower whisker (LW) and upper whisker (UW) are calculated by:

$$LW = \min(\lambda_i \mid \lambda_i \geq Q_1 - 1.5 \times IQR) \quad (5.6)$$

$$UW = \max(\lambda_i \mid \lambda_i \leq Q_3 + 1.5 \times IQR) \quad (5.7)$$

Any data points outside this range are plotted as outliers, highlighting potential anomalies. Box plots are useful for comparing distributions, detecting skewness, and identifying variability or extreme values in datasets. For cell size distribution comparison, the box plot indicates the percent error of the model prediction to the entire range of measured data shown in the histograms of Table 4.2.

Fig. 5.7 provides further insight by decomposing model accuracy as a function of pressure. At lower pressures (20 and 50 kPa), model predictions have tighter interquartile ranges across all models, suggesting that under these conditions, the governing detonation dynamics are well-represented by existing model formulations. However, as pressure increases (100 and 200 kPa), error variances rise significantly, with certain models, particularly Gavrikov *et al.*, displaying extreme maximum exceeding 600% error. For the tested dataset, the IQR remains within the $\pm 200\%$ allowable measurement uncertainty for all models and pressures except Gavrikov *et al.* This suggests that the models or chemical mechanisms used to provide inputs become less reliable at elevated pressures and may indicate a systematic bias or scaling issue in the models, where kinetic assumptions that hold at lower pressures break down as pressure increases. Moreover, at higher pressures, the detonation cell sizes observed on soot foils become smaller, which increases the relative uncertainty in their measurement. However, only Bakalis *et al.*'s model and the scaling factor $\lambda/\Delta_i = 20.8$ fall close to within the measured uncertainty of about 50% of the two

researchers' measurements; they show the least error distribution and very accurately predict the cell size consistently. However, it is important to note that the λ/Δ_i scaling factor requires the experimental cell size to obtain the factor and thus is not a predictive model.

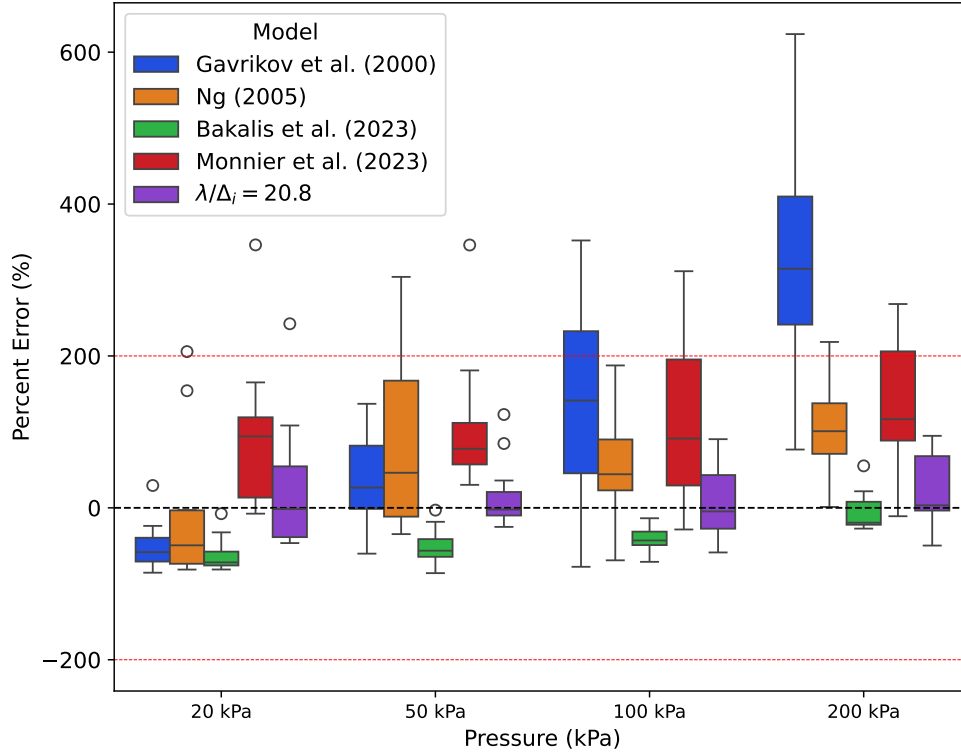


Figure 5.7 – Box plot of model accuracy to experimental results by pressure

This degradation in accuracy at high pressures can be linked to multiple factors. Most models employ empirical fitting constants derived from lower-pressure data, leading to extrapolation errors when applied to high-pressure scenarios. Fig. 5.8 shows the distribution of cell size data sorted by initial test pressure. There is a clear indication that subatmospheric data are much more prevalent than superatmospheric data, and the mode falls in the bin range of 24-42 kPa. This range aligns with the lowest percentage errors seen for the model predictions in this study in Fig. 5.7.

The quantification of the statistical correlation between the models tested and experimental measurements is shown in Table 5.5. These are done using relative error since cell sizes are concerned with the ratio to characteristic lengths, like tube diameter. The mean relative error (MRE) measures the sum of all relative error divided by the number of measurements, where a lower value shows less relative error:

$$MRE = \frac{1}{N} \sum_{i=1}^N \frac{\lambda_i - \hat{\lambda}_i}{\lambda_i} \quad (5.8)$$

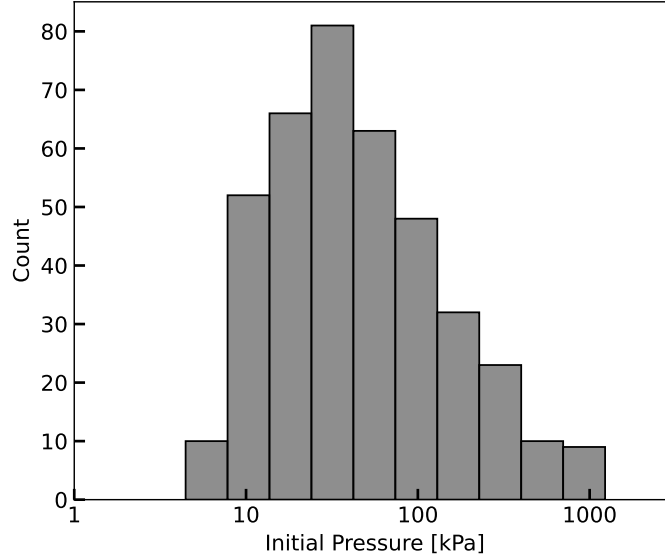


Figure 5.8 – Distribution of number of cell size measurement tests by initial test pressure for all data in literature and this study, for mixtures comprised of hydrogen, methane, and carbon monoxide with oxygen (Appendix A).

where λ is the experimental measurement and $\hat{\lambda}$ is the prediction by the model, and N is the total number of tests. The root mean squared relative error (RMSRE) presents a similar measure but larger errors have higher weighting:

$$RMSRE = \sqrt{\frac{1}{N} \sum_{i=1}^N \left(\frac{\lambda_i - \hat{\lambda}_i}{\lambda_i} \right)^2} \quad (5.9)$$

The bias measures systematic error whereby a model consistently deviates from the measured values in one direction:

$$\text{Relative Bias} = \frac{1}{N} \sum_{i=1}^N \frac{\hat{\lambda}_i - \lambda_i}{\lambda_i} \quad (5.10)$$

The error-range coverage provides the fraction of model predicted cell sizes which are within the range of measured cells for each trial:

$$ERC = \frac{\sum_{i=1}^N I(\lambda_{\min,i} \leq \hat{\lambda}_i \leq \lambda_{\max,i})}{N} \quad (5.11)$$

where I is an indicator function which returns 1 if the condition is met. The absolute measurement error shows heteroscedasticity by presenting a general increase in absolute error with increasing cell size suggesting that the variability of the difference depends on the magnitude of the measurements. This is because as the cell size increases, the measurement precision is on the order of millimetres translating to a greater absolute difference.

Out of the prediction models, Bakalis *et al.* has the lowest MRE and RMSRE, and the highest error range coverage further indicating that the model predicts the cell size measured in this study’s tests accurately. Ng has the next lowest MRE and RMSRE and the second-highest error range coverage. The two models also have a small difference in MRE and RMSRE showing more consistency in the models throughout the range of parameters tested as the mean was not skewed by larger deviations. They are well within the agreed factor of two deviation for cell size measurements. Gavrikov *et al.* had high errors and bias, and the predictions were not as accurate in the range of cell size measurements. The λ/Δ_i correlation shows low MRE and RMSRE similar to Bakalis *et al.*’s model, but with the lowest bias and error range coverage; however, the scaling factor was fitted to the results of this study so low errors are expected. It is interesting to see though that the prediction model of Bakalis *et al.* has similar error to the fitted λ/Δ_i , showing it is able to accurately adapt to new mixtures and pressures not in its training original dataset. Most of the models have a bias to overpredict the cell size; however, Bakalis *et al.* is the only model to consistently underpredict. This has implications for the usability of these models in designing critical physical dimensions like tubes in industrial safety or minimum diameter RDEs. For example, the critical tube diameter requires a $d_c < 13\lambda$ for a detonation to fail [16]. Additionally, the same is true for an RDE application where the requirement is a minimum diameter of $\sim 40\lambda$ [42]. Thus, an underpredicting model would result in developing an RDE with too small a diameter for the fuel being used. When considering these applications, the Bakalis *et al.* model’s tendency to underpredict by about 40% on average is a greater risk to the physical applications and should be noted.

In all prediction models, the mean relative error is greater than is reported in their respective papers. Gavrikov *et al.* [2] report a 50% average error, Ng [3] reports a 46.4% error, Bakalis *et al.* [4] report a 22.3% error, and while Monnier *et al.* [5] do not report a percentage error, they specify that the model has good agreement when the mechanism is suited to the mixture except in cases of high argon dilution where it overpredicts despite mechanism selection. The errors found for the experimental mixtures of this study are greater than the reported error for each model by a factor of two for Bakalis *et al.* and Ng, and a factor of three for Gavrikov *et al.*

Table 5.5 – Statistical correlations between experimental ternary cell widths and prediction models

Model	Mean relative error	Root mean squared relative error	Relative bias	Error range coverage
Bakalis <i>et al.</i> [4]	43%	48%	-40%	64%
Gavrikov <i>et al.</i> [2]	152%	206%	117%	29%
Ng [3]	85%	109%	60%	57%
Monnier <i>et al.</i> [5]	113%	147%	110%	56%
$\lambda/\Delta_i = 20.8$ [1]	42%	60%	16%	76%

Further granularity can be obtained by considering each trial mixture and pressure independently and comparing the holistic dataset of cell size measurements to each model prediction. For this analysis, all cells measured on a soot foil for a test of a certain mixture

and pressure are compared to the single predicted value of the model. In cases where multiple trials are done at the same conditions, the cell size results are aggregated. This helps indicate how the model predicts within the framework of considering the cell size of an experiment as a distribution rather than a single representative value. Since cell size models only return a single value for the prediction, the box plots indicate the degree to which the prediction falls within the variation seen in the histograms. Therefore, a model that predicts close to the expected value of the log-normal distribution would result in a box plot of small IQR and range. Contrarily, if the model predicts within the edges of the distribution, some values present larger errors than others, resulting in a larger IQR and greater variation in the error. Notably, these plots are subject to the distribution seen for the experimental values, but this is a feature of this comparison as it details the extent to which the model can predict a cell size that is representative of the distribution mean rather than just one observed value. This is shown in Fig. 5.9.

Fig. 5.9 presents several overarching trends between pressure, mixture and model, while showing some anomalous data points as well. The composition of the fuel mixture also plays a critical role in the accuracy of detonation cell size predictions. Hydrogen-containing mixtures (Mix 1-6) generally exhibit lower relative errors, whereas methane and CO mixtures (Mix 7-9) display significantly larger errors. Hydrogen detonations are well-studied, with well-defined cell structures, making them easier for models to predict. In contrast, CH₄- and CO-based detonations involve higher activation energy and lower CJ velocity, greater sensitivity to intermediate species [103], and more irregular cell structure [45], which may not be adequately represented in the models or are more difficult to measure. Moreover, while hydrogen data are plentiful and used in the empirical correlations for the models, carbon monoxide and methane binary fuel mixture tests are scarcer and not used in the models' fits. The large errors observed for mixtures 7-9, particularly at higher pressures, indicate that these models struggle to generalize across different fuel chemistries.

Examining the performance of the models in individual mixtures reveals distinct patterns. The Gavrikov *et al.* and Monnier *et al.* models show the highest relative errors and the largest variability. In many cases, these models significantly overpredict the detonation cell size, particularly at high pressures and for binary CH₄-CO mixtures. This suggests that their underlying assumptions may not adequately capture the detonation physics for complex fuels or at elevated pressures. On the other hand, the Bakalis *et al.* and Ng models generally perform better, with lower median errors, tighter IQR, and less variability. Bakalis *et al.* is the most consistent model, often yielding the smallest errors across different conditions, making it the most reliable choice for general prediction applications. Statistically, this means that the worse performing models did not predict close to the centre of the spread of histogram data, whereas the better models did, allowing them to better encompass the variability. The $\lambda/\Delta_i = 20.8$ fit shows similar low percentage error and tight IQR indicating that it predicts a cell size close to the expected value of the distribution. This is due to it being calibrated from the average cell size of these experiments. The greatest errors for the fitted scaling factor are for Mix 7-9 which have a significantly lower calculated λ/Δ_i than the averaged 20.8 value used in this comparison, which further demonstrates the sensitivity of this model to the experimentally-derived scaling factor.

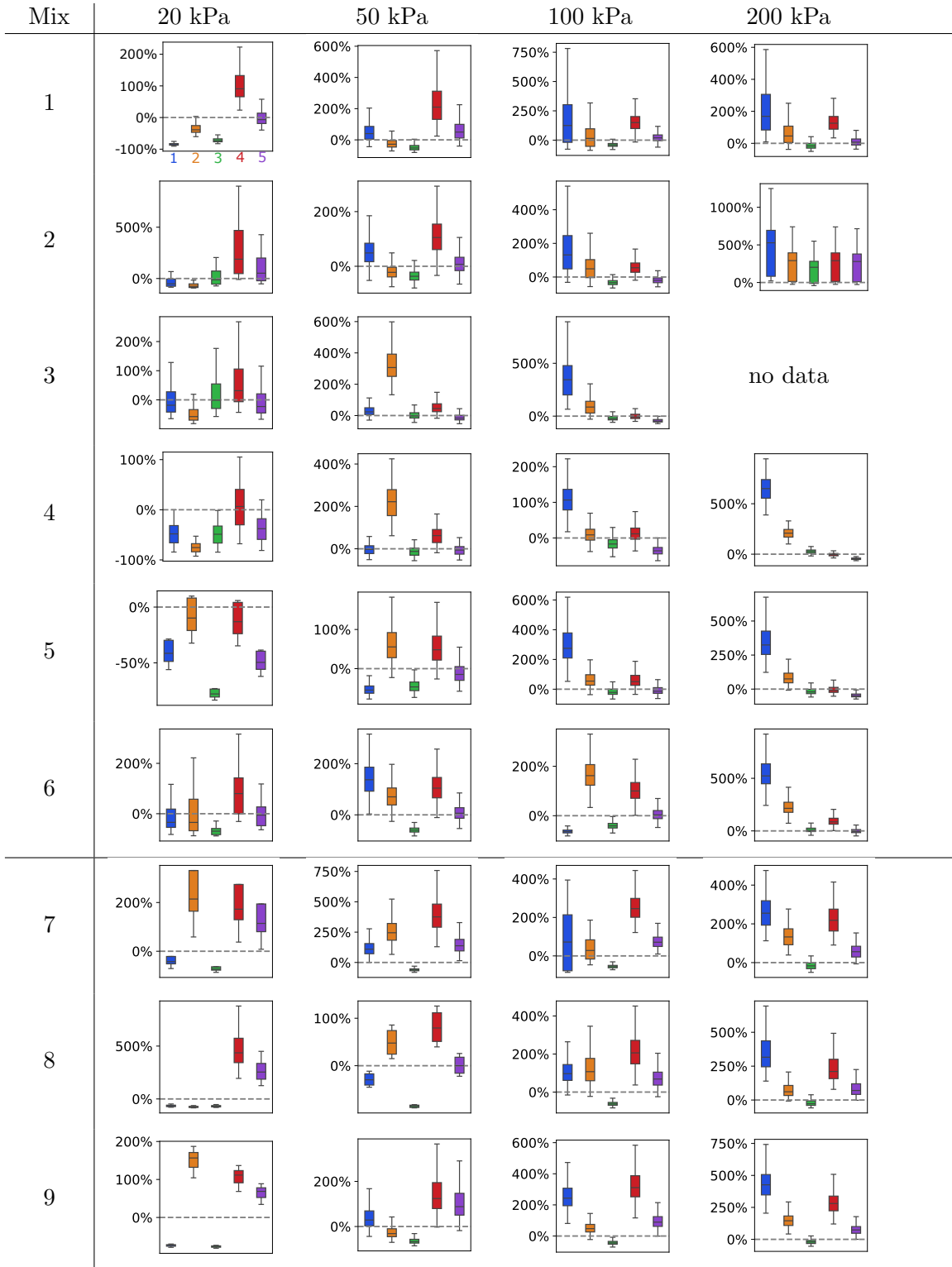


Figure 5.9 – Relative error box plots of experimental measurements for ternary fuel mixtures compared to prediction cell models of 1. Gavrikov *et al.*[2], 2. Ng [3], 3. Bakalis *et al.*[4], 4. Monnier *et al.*[5], $\lambda/\Delta_i = 20.8$ [1]

Certain fuel-pressure combinations stand out in the data. Mix 1-3 at 20 kPa and 50 kPa have the lowest overall relative error reflecting a good modelling ability of changes in hydrogen and with little carbon monoxide at low pressure. Mix 4 and 5 at 20 kPa were the only ones where most models underpredicted the cell size, albeit not by a significant amount. These low pressure tests had higher ratios of carbon monoxide which resulted in more varied and larger cell sizes seen on the experimental soot foils, aligning with a previous study's results by Austin and Shepherd on CO detonations [103]. Since little data are available on carbon monoxide detonations, the models rely on hydrogen and methane parameters, which would produce smaller cells than with carbon monoxide added. For mixtures containing higher amounts of methane (Mix 1, 2, 6, and 9), the Monnier *et al.* model tends to have greater error in this study. The model study shows similar overestimation in cell size for methane-oxygen mixtures which the authors attribute to the fundamental assumption of adiabatic heating by shock compression, and the combustion mechanism including turbulent diffusion for this mixture [5]. The shapes of the box plots give an indication of the accuracy and precision of the models. Several plots show very short IQRs and spread which indicate that the models are precise and the cell sizes are more consistent and regular. In cases with a higher IQR, there is significantly more variability in the detonation cell sizes measured and the models' predictions are less accurate which reflects greater in the relative error. In general, Gavrikov *et al.*, Monnier *et al.*, and Ng models have larger spread meaning they likely predict a cell size that is farther from the central tendency of the measured data, leading to higher IQR.

There are possible sources of error in current models that stem from the reliance on approximations and empirical correlations regarding reaction kinetics and shock dynamics that may not be representative for all mixtures and pressures. The activation energy, thermicity and induction length depend on various intermediate reaction mechanisms which vary significantly between hydrogen, methane, and carbon monoxide mixtures. Methane and carbon monoxide have higher activation energies and induction lengths than hydrogen mixtures, thus if a model is primarily calibrated using hydrogen data, it would poorly predict the cell size for the other fuels. Empirical models also fit their parameters to a limited set of pressure conditions. The fact that errors increase at high pressures suggests that models may not properly scale with pressure.

Several key conclusions emerge from this analysis. First, higher pressures lead to higher prediction errors, indicating a need for better high-pressure detonation models coupled with more experimental data to calibrate. Second, hydrogen-based mixtures are predicted with greater accuracy, whereas hydrocarbon- and CO-rich mixtures present significant challenges for existing models. Third, the Bakalis *et al.* model generally outperforms others, making it the preferred choice for detonation cell size prediction. Ultimately, the findings highlight the limitations of existing detonation models and underscore the need for continued research into detonation dynamics across varied fuel compositions and pressure regimes.

5.2.1 Extending Model Comparison to Literature Data

The comparison of measured cell size to model prediction is now expanded to available literature data for mixtures comprised of hydrogen, methane and/or carbon monoxide reacted with oxygen stoichiometrically, serving as a broader validation of the models presented. The entire set of considered data are shown in Appendix A with average cell size, as well as minimum and maximum cell sizes measured where available by the source author. The models are compared again using a histogram of all predictions' relative error for mean cell width, and a box plot breaking down the trends with pressure.

The histograms in Fig. 5.10 show a left-skewed error distribution, with most model predictions exhibiting errors in the 10–100% range, though with significant occurrences of extreme errors exceeding 200% in all models. The spread of errors suggests that model accuracy is highly dependent on the specific mixture conditions and operating pressures. The box plot (Fig. 5.11) provides further insight by decomposing model accuracy as a function of pressure. At lower pressures (20–50 kPa), model predictions are relatively accurate, with tight interquartile ranges across all models, suggesting that under these conditions, the governing detonation dynamics are well-represented by existing model formulations. However, as pressure increases (100–200 kPa), error variances rise significantly, with certain models, particularly Gavrikov *et al.*, displaying extreme inaccuracy well exceeding the tolerable 200% range. The $\lambda/\Delta_i = 20.8$ model shows a greater number of outliers when considering the entire dataset, showing that the calibration from this study's mixtures does not hold for all mixtures comprised of varying fractions of hydrogen, carbon monoxide, and methane reacted with stoichiometric oxygen. This suggests that the λ/Δ_i is well suited to the fitted experimental data but struggles when applied to the broader range of mixtures and pressures, and should not be used without experimental calibration. The consideration of all data though generally shows the same trends as this study's subset data, with Bakalis *et al.* still being the most accurate in all conditions. However, there is an anomaly at 30–50 kPa where the Bakalis *et al.* ANN shows considerably higher error.

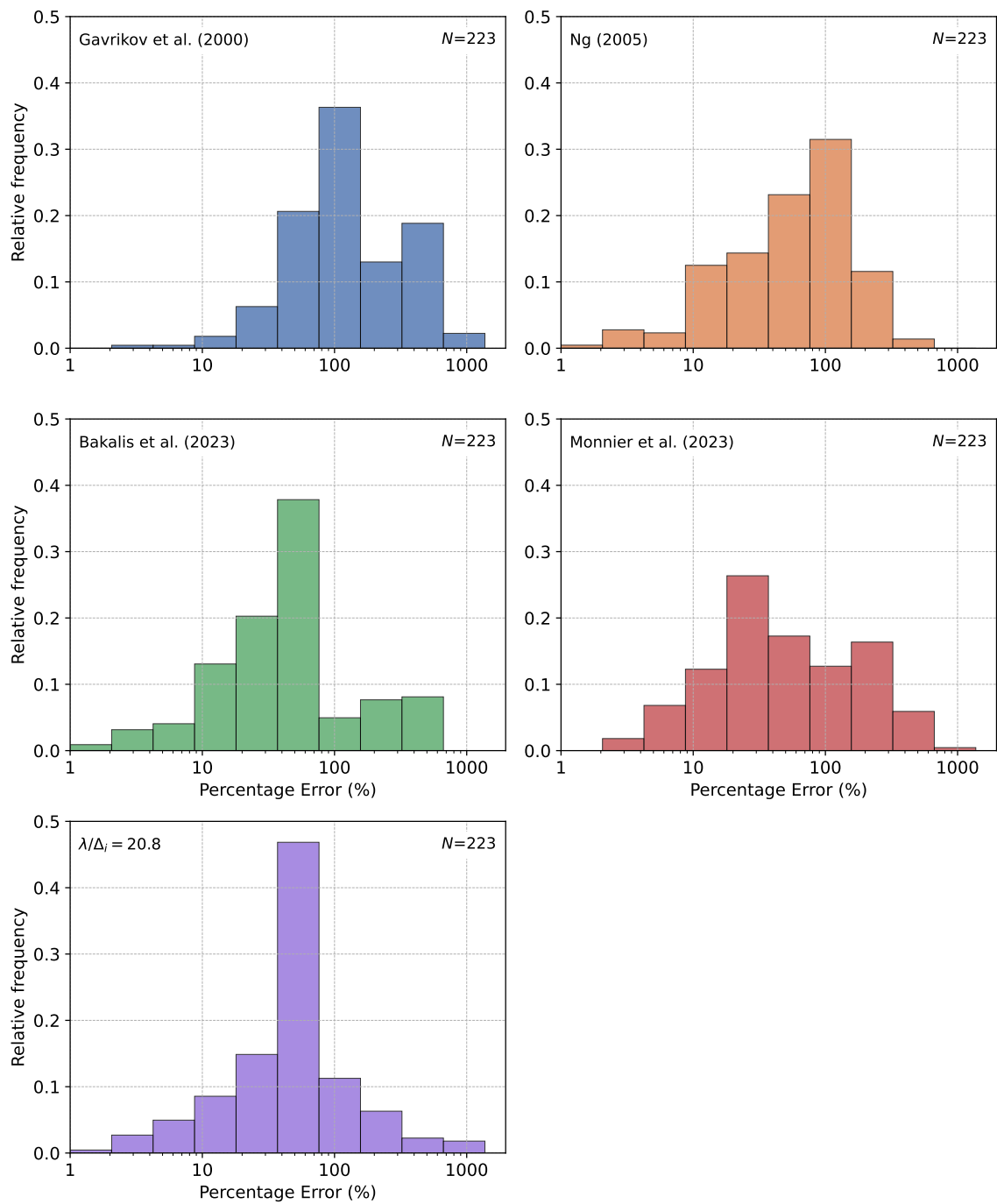


Figure 5.10 – Relative frequency of percent error by model for all test and literature binary and ternary mixtures comprised of hydrogen, methane, and carbon monoxide

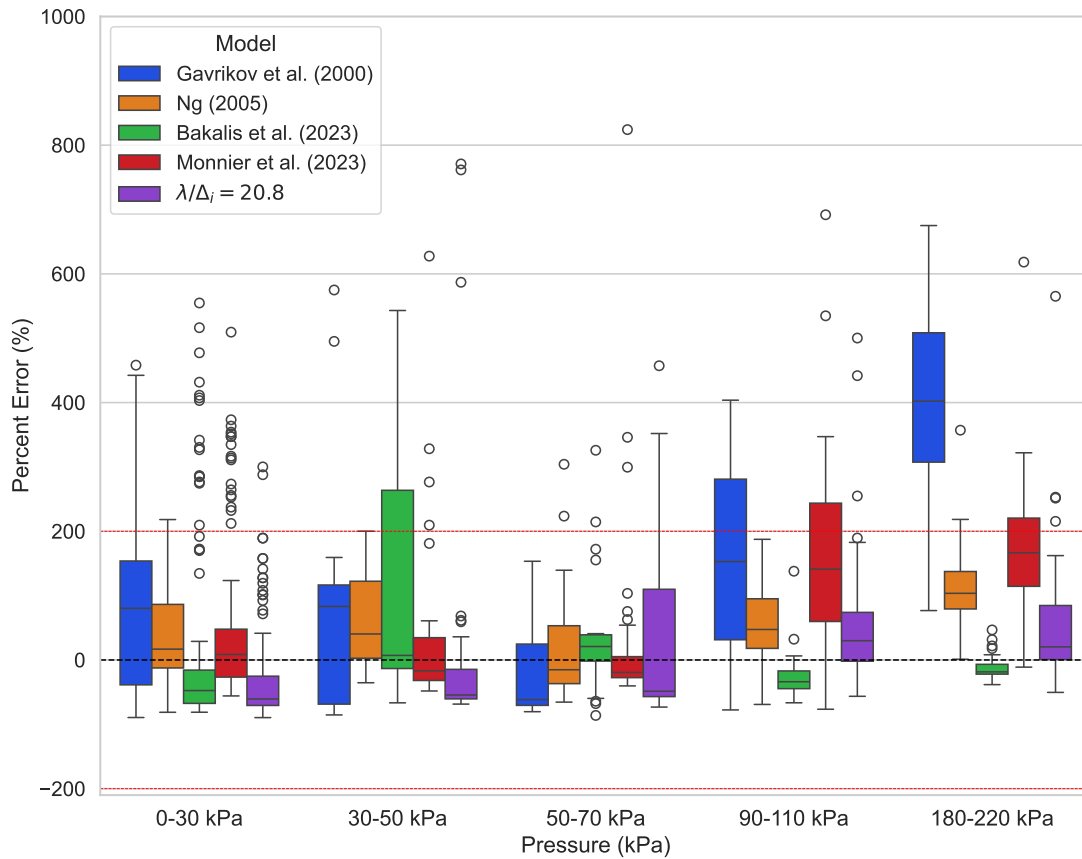


Figure 5.11 – Box plot of model accuracy to experimental and published binary and ternary mixtures comprised of hydrogen, methane, and carbon monoxide by pressure

Examining the performance of the same models against the ternary fuel dataset (Fig. 5.6 and 5.11) provides a controlled subset analysis. The histograms in Fig. 5.6 reveal a similar left-skewed error distribution, with the majority of errors in the 10–100% range and occasional outliers. In both cases, all the models seemingly perform within the $\pm 200\%$ range except for Gavrikov *et al.* at high pressures. Since the cells are smaller at high pressures, small changes in measurements cascade into larger percentage error when compared to the predicted values. This may bias the trends seen at high pressure as well which is why cell size distributions are more representative and less susceptible to measurement errors.

A critical difference is found in this study between reporting methods for detonation cell size. Most literature sources report only the average cell size, while this study attempts to capture the full distribution of cell sizes on a single foil. This difference has substantial implications for model validation. By reporting only the mean cell size, literature studies effectively remove the inherent variability in cell size measurements and the distributions seen for a given experimental soot foil. This can lead to artificially reduced error estimates when comparing to model predictions, as the averaging process removes extreme variations

that the models fail to capture. Moreover, this study found it imperative to report a distribution of cell size which should then be used to provide a range of predicted values showcasing the inherent variability in actual detonations.

5.2.2 Future Work in Statistical Detonation Cell Size Modelling

The comparison of experimental detonation cell size against existing models has uncovered several strong points but also areas of improvement to providing a first-order prediction. The prediction models tested are relatively simple to implement and use calculable initial parameters that can be obtained without having to run experiments. They are not computationally intensive and present the user with a single value of cell size based on the empirical correlations made from the calibrated dataset. However, the study also finds that these models may be misleading to the actual nature of detonation cells seen experimentally. Table 4.2 clearly shows that an average cell size is not representative of the actual distribution seen on one soot foil. While it is laborious to measure every cell on a foil, it is beneficial to visualize the range and frequency of these measurements. This should also be translated to cell models where a distribution, or at least a range, is given instead of one value. This would be beneficial to designing physical applications of detonations where a predicted distribution could be used to design critical dimensions more accurately. By systematically analyzing the statistical behavior of model errors and linking them to fundamental detonation dynamics, this study provides a comprehensive assessment of the strengths and limitations of existing detonation cell size models across different fuel mixtures and operating conditions.

5.3 RMC Detonation Channel

The cell sizes obtained at RMC can be compared to the well-established published data. Fig. 5.12 shows the RMC tests superimposed with the literature data for stoichiometric hydrogen-oxygen.

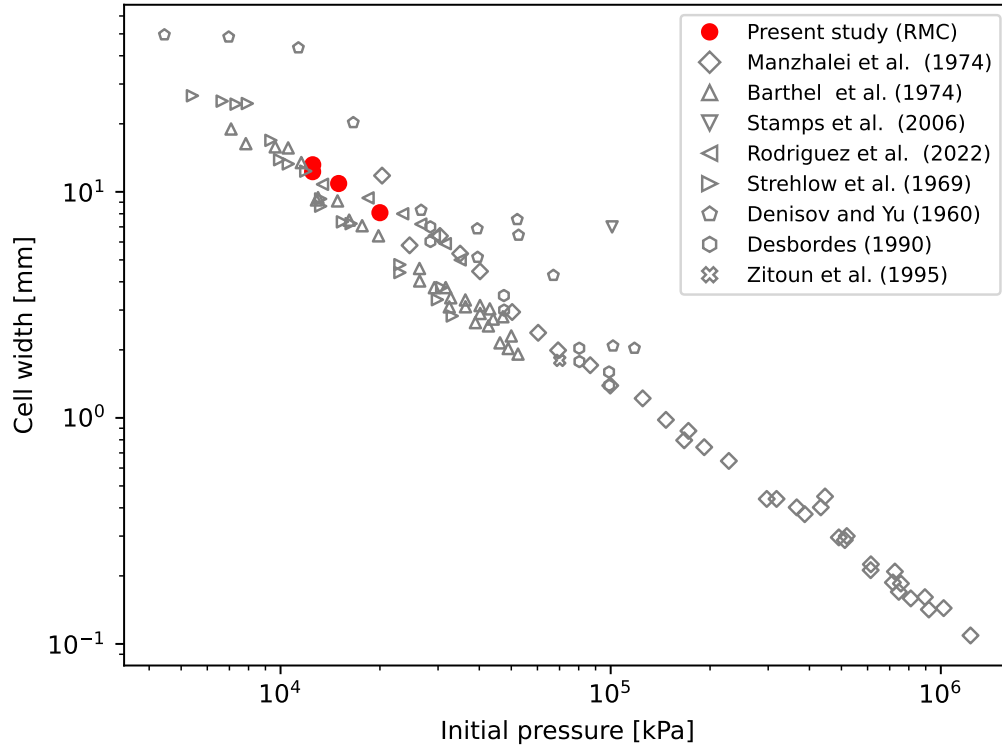


Figure 5.12 – Initial pressure vs cell width for stoichiometric hydrogen-oxygen mixtures, including literature data and preliminary RMC channel data. References: Manzhalei *et al.* (1974) [63], Barthel *et al.* (1974) [50], Stamps *et al.* (2006) [51], Rodriguez *et al.* (2022) [46], Strehlow *et al.* (1969) [52], Denisov and Yu (1960) [53], Desbordes (1990) [54], Zitoun *et al.* (1995) [55].

Fig. 5.12 shows that the cell sizes measured for the present study at RMC agree with the published data accurately. While more data can be obtained in the future, this shows that the RMC channel can produce a detonation and the results are valid for comparison with other channels. Additionally, the RMC channel is the only rectangular channel in Fig. 5.12, showing that channel geometry did not have a significant role in affecting the cell size at these pressures and mixture compositions.

The pressure transducer traces in Fig. 4.4 show an average velocity of 99% the CJ velocity as calculated by SDToolBox [61]. Moreover, the v_N pressure was calculated to be 3150 kPa which is similar to the peaks seen in the data. This further confirms that the experiment resulted in a successful CJ detonation.

Chapter 6

Conclusions

This study conducted experiments in detonation channels for multi-fuel mixtures comprised of hydrogen, methane, and carbon monoxide at a range of pressures. These experiments were performed in a cylindrical detonation channel at ENSMA and measurements of cell size distributions were taken from sooted foils. The results, along with existing binary fuel data, were compared to existing empirical detonation cell size models to evaluate their accuracy on new data.

The experimental results show average cell sizes ranging from 1.8 mm in high pressure hydrogen rich mixtures to 47.5 mm in lower pressure mixtures with high proportion of carbon monoxide. More importantly, the analysis shows that there is a significant variation in cell size on a foil and a distribution is more representative of the experiment. However, for some of the trials, especially at lower pressures, there are not a statistically significant number of cells measured to present a distribution. Comparing the ternary fuel trends to existing binary fuel literature data shows good agreement and consistent trends with pressure. The inaugural testing of the RMC detonation channel with stoichiometric hydrogen-oxygen presents cell sizes in concurrence with literature data.

Comparing the cell size to prediction models shows several important trends and conclusions. The ratio of λ/Δ_1 varies from 11.5-32.3 for the multi-fuel mixtures analyzed, which does not provide a simple correlation without having to test each mixture. The *ex post facto* model using $\lambda/\Delta_1 = 20.8$, based on the average of this study's scaling factors, shows a fairly accurate prediction for the experiment's mixtures, though does not extend well to literature data. The semi-empirical models of Gavrikov *et al.*, Ng, Bakalis *et al.*, and Monnier *et al.* are based on calculable initial chemical and thermodynamic conditions. Across the range of data, Bakalis *et al.*'s ANN model is the most accurate and consistently provides a prediction within the 200% of generally accepted measurement error for cell size, and often below the 50% variability measured between the two researchers. All models struggle more with higher pressure predictions and binary mixtures without hydrogen showing that the empirical correlations are calibrated on specific existing data.

The study presents several important considerations for evaluating multi-fuel mixtures for physical applications. First, it is important to consider the cell size distribution rather than an average which is more representative of actual detonation experiments and can help train models. Second, the prevalence of low pressure data has intrinsically made models more accurate at subatmospheric pressures; however, most modern detonation applications like pipelines and RDEs operate at superatmospheric pressures. Third, the growing interest in sustainable and alternative fuels comprised of multiple constituent fuels warrants research in these mixtures and further evaluation of cell size modelling.

Chapter 7

Recommendations

Building on the conclusions of this thesis, several key recommendations can be made to further improve the understanding of detonation cell size behavior in multi-fuel mixtures and to enhance the predictive capabilities of current models. The experimental work and model evaluation undertaken here highlight both the promise and the limitations of existing approaches, particularly in the context of emerging applications involving sustainable and complex fuel blends.

First, there is a pressing need to expand the dataset of high-pressure and multi-fuel mixture experiments. The study found that existing models often struggle to accurately predict detonation cell sizes for hydrogen-deficient and high-pressure mixtures, largely due to the abundance of subatmospheric data in existing literature. Since most real-world detonation applications, such as those in RDEs and pipeline safety, occur at elevated pressures, the lack of comprehensive data in this regime presents a critical gap. A targeted campaign to gather additional cell size measurements for ternary or more complex fuel blends at elevated pressures would enable both the calibration and validation of future models in a more representative space.

Second, low-pressure experiments should be repeated using the RMC rectangular detonation channel to acquire additional cell size data and achieve statistically significant distributions consistent with the log-normal fits observed at higher pressures. The current results confirm that the RMC channel yields hydrogen-oxygen cell size measurements in good agreement with literature values from cylindrical geometries, validating its use despite the difference in cross-section.

Third, the study reveals that model accuracy varies depending on the chemical kinetic mechanism used for kinetic and thermodynamic calculations such as induction length. This suggests that the semi-empirical models should be tested using multiple chemical mechanisms to evaluate their sensitivity to underlying mechanism assumptions. By testing models with different appropriate chemical mechanisms, it may be possible to improve prediction fidelity and identify which mechanisms are most appropriate for certain mixtures.

Finally, future work should aim to develop a new class of predictive models that can estimate the detonation cell size of multi-component fuel mixtures based on the properties of their constituent fuels. Such a model could, for instance, use known binary or pure fuel behavior to infer the effective behavior of a ternary mixture, providing a path toward predictive design without requiring complete experimental characterization of every possible blend. This would represent a substantial advancement in the field, enabling greater flexibility in fuel formulation and reducing the experimental burden required to support emerging propulsion technologies.

These recommendations highlight the need for a concerted effort in high-pressure testing, model refinement, and data expansion to support the safe and efficient application of detonation systems using modern and alternative fuels.

References

- [1] K. I. Shchelkin and Y. K. Troshin, *Gasdynamics of combustion*. National Aeronautics and Space Administration, 1964, vol. 231.
- [2] A. Gavrikov, A. Efimenko, and S. Dorofeev, “A model for detonation cell size prediction from chemical kinetics”, *Combustion and Flame*, vol. 120, no. 1, pp. 19–33, Jan. 2000, ISSN: 00102180. DOI: 10.1016/S0010-2180(99)00076-0.
- [3] H. D. Ng, “The effect of chemical reaction kinetics on the structure of gaseous detonations”, Ph.D. dissertation, McGill University, Canada, 2005.
- [4] G. Bakalis, M. Valipour, J. Bentahar, L. Kadem, H. Teng, and H. D. Ng, “Detonation cell size prediction based on artificial neural networks with chemical kinetics and thermodynamic parameters”, *Fuel Communications*, vol. 14, p. 100084, Mar. 2023, ISSN: 26660520. DOI: 10.1016/j.jfueco.2022.100084.
- [5] V. Monnier, P. Vidal, V. Rodriguez, and R. Zitoun, “From graph theory and geometric probabilities to a representative width for three-dimensional detonation cells”, *Combustion and Flame*, vol. 256, p. 112996, Oct. 2023, ISSN: 00102180. DOI: 10.1016/j.combustflame.2023.112996.
- [6] Natural Resources Canada. “Energy from hydrogen: the basics”, Government of Canada. (2024), [Online]. Available: <https://natural-resources.canada.ca/our-natural-resources/energy-sources-distribution/clean-fuels/energy-from-hydrogen-the-basics/23025> (visited on 03/18/2024).
- [7] S. O. Restrepo, J. Denninger, M. Adams, R. Thelen, and A. Adams, “Composition analysis of hydrogen-enriched natural gas by high-pressure benchtop NMR spectroscopy with a low-cost flow-through cell design”, *International Journal of Hydrogen Energy*, vol. 66, pp. 604–611, May 2024, ISSN: 03603199. DOI: 10.1016/j.ijhydene.2024.04.119.
- [8] National Grid and Atlantic Hydrogen Inc., *Hydrogen-enriched natural gas*, 2009.
- [9] Z. Wang, J. Yang, Z. Li, and Y. Xiang, “Syngas composition study”, *Frontiers of Energy and Power Engineering in China*, vol. 3, no. 3, pp. 369–372, Sep. 2009, ISSN: 1673-7393, 1673-7504. DOI: 10.1007/s11708-009-0044-7.

- [10] M. Herout, J. Malaták, L. Kučera, and T. Dlabaja, “Biogas composition depending on the type of plant biomass used”, *Research in Agricultural Engineering*, vol. 57, no. 4, pp. 137–143, Dec. 31, 2011, ISSN: 12129151, 18059376. DOI: 10.17221/41/2010-RAE.
- [11] L. Jin, H. Zhao, M. Wang, B. Wei, and H. Hu, “Effect of temperature and simulated coal gas composition on tar production during pyrolysis of a subbituminous coal”, *Fuel*, vol. 241, pp. 1129–1137, Apr. 2019, ISSN: 00162361. DOI: 10.1016/j.fuel.2018.12.093.
- [12] A. W. Golubkov, S. Scheickl, R. Planteu, G. Voitic, H. Wiltsche, C. Stangl, G. Fauler, A. Thaler, and V. Hacker, “Thermal runaway of commercial 18650 li-ion batteries with LFP and NCA cathodes – impact of state of charge and overcharge”, *RSC Advances*, vol. 5, no. 70, pp. 57171–57186, 2015, ISSN: 2046-2069. DOI: 10.1039/C5RA05897J.
- [13] A. W. Golubkov, D. Fuchs, J. Wagner, H. Wiltsche, C. Stangl, G. Fauler, G. Voitic, A. Thaler, and V. Hacker, “Thermal-runaway experiments on consumer li-ion batteries with metal-oxide and olivin-type cathodes”, *RSC Adv.*, vol. 4, no. 7, pp. 3633–3642, 2014, ISSN: 2046-2069. DOI: 10.1039/C3RA45748F.
- [14] J. H. S. Lee, *The Detonation Phenomenon*. New York: Cambridge University Press, 2008.
- [15] Y. N. Denisov, “Pulsating and spinning detonation of gaseous mixtures in tubes”, in *Dokl. Akad. Nauk SSSR*, vol. 125, 1959, pp. 110–113.
- [16] V. V. Mitrofanov and R. I. Soloukhin, “The multifront detonation diffraction”, in *Doklady Akademii Nauk*, Russian Academy of Sciences, vol. 159, 1964, pp. 1003–1006.
- [17] I. Moen, S. Murray, D. Bjerketvedt, A. Rinnan, R. Knystautas, and J. Lee, “Diffraction of detonation from tubes into a large fuel-air explosive cloud”, *Symposium (International) on Combustion*, vol. 19, no. 1, pp. 635–644, Jan. 1982, ISSN: 00820784. DOI: 10.1016/S0082-0784(82)80238-5.
- [18] I. Moen, “Influence of cellular regularity on the behavior of gaseous detonations”, *Dynamics of explosions*, vol. 106, pp. 220–243, 1986.
- [19] D. Desbordes, C. Gueraud, L. Hamada, and H. Presles, “Failure of the classical dynamic parameters relationships in highly regular cellular detonation systems”, *Progress in Astronautics and Aeronautics*, vol. 153, pp. 347–347, 1993.
- [20] B. A. Rankin, M. L. Fotia, A. G. Naples, C. A. Stevens, J. L. Hoke, T. A. Kaemming, S. W. Theuerkauf, and F. R. Schauer, “Overview of performance, application, and analysis of rotating detonation engine technologies”, *Journal of Propulsion and Power*, vol. 33, no. 1, pp. 131–143, Jan. 2017, ISSN: 0748-4658, 1533-3876. DOI: 10.2514/1.B36303.
- [21] K. Kailasanath, “Recent developments in the research on rotating-detonation-wave engines”, in *55th AIAA Aerospace Sciences Meeting*, Grapevine, Texas: American Institute of Aeronautics and Astronautics, Jan. 9, 2017, ISBN: 978-1-62410-447-3. DOI: 10.2514/6.2017-0784.

- [22] J. Li, S. Yao, Y. Lei, J. Yu, Y. Zhou, and W. Zhang, “Experimental investigation of rotating detonation engine fueled by liquid ethanol and oxygen-enriched air”, *Experimental Thermal and Fluid Science*, vol. 167, p. 111–149, Aug. 2025, ISSN: 08941777. DOI: 10.1016/j.expthermflusci.2025.111494.
- [23] S. M. Jones and D. E. Paxson, “Potential benefits to commercial propulsion systems from pressure gain combustion”, in *49th AIAA / ASME / SAE / ASEE Joint Propulsion Conference*, San Jose, CA: American Institute of Aeronautics and Astronautics, Jul. 14, 2013, ISBN: 978-1-62410-222-6. DOI: 10.2514/6.2013-3623.
- [24] J. A. Nicholls, H. Wilkinson, R. B. Morrison, and R. S. B. Ong, “Intermittent detonation as a thrust-producing mechanism: quarterly progress report no. 1.”, Engineering Research Institute, University of Michigan, Tech. Rep., 1954.
- [25] B. V. Voytsekhovskiy, “Stationary spin detonation”, *Doklady Akademii Nauk USSR (Proceedings of the Academy of Sciences USSR)*, vol. 129, pp. 1254–1256, 5 1960.
- [26] J. A. Nicholls and R. E. Cullen, “The feasibility of a rotating detonation wave rocket motor”, Air Force Flight Test Center, Edwards Air Force Base, California, Technical Report, Apr. 1964.
- [27] J. A. Nicholls, R. E. Cullen, and K. W. Ragland, “Feasibility studies of a rotating detonation wave rocket motor.”, *Journal of Spacecraft and Rockets*, vol. 3, no. 6, pp. 893–898, Jun. 1966, ISSN: 0022-4650, 1533-6794. DOI: 10.2514/3.28557.
- [28] F. A. Bykovskii and V. V. Mitrofanov, “Detonation combustion of a gas mixture in a cylindrical chamber”, *Combustion, Explosion, and Shock Waves*, vol. 16, no. 5, pp. 570–578, 1981, ISSN: 0010-5082, 1573-8345. DOI: 10.1007/BF00794937.
- [29] F. A. Bykovskii and E. F. Vedernikov, “Continuous detonation combustion of an annular gas-mixture layer”, *Combustion, Explosion, and Shock Waves*, vol. 32, no. 5, pp. 489–491, Sep. 1996, ISSN: 0010-5082, 1573-8345. DOI: 10.1007/BF01998570.
- [30] M. L. Fotia, F. Schauer, T. Kaemming, and J. Hoke, “Experimental study of the performance of a rotating detonation engine with nozzle”, *Journal of Propulsion and Power*, vol. 32, no. 3, pp. 674–681, May 2016, ISSN: 0748-4658, 1533-3876. DOI: 10.2514/1.B35913.
- [31] M. L. Fotia, J. Hoke, and F. Schauer, “Experimental performance scaling of rotating detonation engines operated on gaseous fuels”, *Journal of Propulsion and Power*, vol. 33, no. 5, pp. 1187–1196, Sep. 2017, ISSN: 0748-4658, 1533-3876. DOI: 10.2514/1.B36213.
- [32] A. Lentsch, R. Bec, L. Serre, F. Falempin, D. Daniau, D. Piton, A. Prigent, G. Cantains, R. Zitoun, D. Desbordes, F. Jouot, and I. Gokalp, “Overview of current french activities on PDRE and continuous detonation wave rocket engines”, in *AIAA/CIRA 13th International Space Planes and Hypersonics Systems and Technologies Conference*, Capua, Italy: American Institute of Aeronautics and Astronautics, May 16, 2005, ISBN: 978-1-62410-068-0. DOI: 10.2514/6.2005-3232.
- [33] F. A. Bykovskii, S. A. Zhdan, E. F. Vedernikov, and Y. A. Zholobov, “Continuous and pulsed detonation of a coal-air mixture”, *Doklady Physics*, vol. 55, no. 3, pp. 142–144, Mar. 2010, ISSN: 1028-3358, 1562-6903. DOI: 10.1134/S1028335810030092.

- [34] F. A. Bykovskii, S. A. Zhdan, E. F. Vedernikov, and Y. A. Zholobov, “Detonation of a coal-air mixture with addition of hydrogen in plane-radial vortex chambers”, *Combustion, Explosion, and Shock Waves*, vol. 47, no. 4, pp. 473–482, Jul. 2011, ISSN: 0010-5082, 1573-8345. DOI: 10.1134/S0010508211040113.
- [35] F. A. Bykovskii, S. A. Zhdan, E. F. Vedernikov, and Y. A. Zholobov, “Continuous spin detonation of a coal-air mixture in a flow-type plane-radial combustor”, *Combustion, Explosion, and Shock Waves*, vol. 49, no. 6, pp. 705–711, Nov. 2013, ISSN: 0010-5082, 1573-8345. DOI: 10.1134/S0010508213060105.
- [36] W. Wu, Y. Wang, W. Han, G. Wang, M. Zhang, and J. Wang, “Experimental research on solid fuel pre-combustion rotating detonation engine”, *Acta Astronautica*, vol. 205, pp. 258–266, Apr. 2023. DOI: 10.1016/j.actaastro.2023.02.007.
- [37] H. Xu, C. Weng, and Q. Zheng, “Experimental study on the aluminum powder rotating detonation engine”, *Proceedings of the 28th ICDERS Conference*, Jun. 2022.
- [38] H. Xu, X. Ni, X. Su, B. Xiao, Y. Luo, F. Zhang, C. Weng, and Q. Zheng, “Experimental investigation on the application of the coal powder as fuel in a rotating detonation combustor”, *Applied Thermal Engineering*, vol. 213, p. 118 642, Aug. 2022, ISSN: 13594311. DOI: 10.1016/j.applthermaleng.2022.118642.
- [39] V. Yogeshkumar, N. Rathi, and P. A. Ramakrishna, “Solid fuel rich propellant development for use in a ramjet to propel an artillery shell”, *Defence Science Journal*, vol. 70, no. 3, pp. 329–335, Apr. 24, 2020, ISSN: 0976-464X, 0011-748X. DOI: 10.14429/dsj.70.15061.
- [40] N. Kubota, Y. Yano, K. Miyata, T. Kuwahara, M. Mitsuno, and I. Nakagawa, “Energetic solid fuels for ducted rockets (II)”, *Propellants, Explosives, Pyrotechnics*, vol. 16, no. 6, pp. 287–292, Dec. 1991, ISSN: 0721-3115, 1521-4087. DOI: 10.1002/prep.19910160606.
- [41] S. Ringuette, C. Dubois, and R. Stowe, “On the optimization of GAP-based ducted rocket fuels from gas generator exhaust characterization”, *Propellants, Explosives, Pyrotechnics*, vol. 26, pp. 118–124, 2001. DOI: 10.1002/1521-4087(200106)26:3<118::AID-PREP118>3.0.CO;2-0.
- [42] F. A. Bykovskii, S. A. Zhdan, and E. F. Vedernikov, “Continuous spin detonations”, *Journal of Propulsion and Power*, vol. 22, no. 6, pp. 1204–1216, Nov. 2006, ISSN: 0748-4658, 1533-3876. DOI: 10.2514/1.17656.
- [43] T. Shan, P. Zhang, Z. Wang, and X. Zhu, “Insights into extreme thermal runaway scenarios of lithium-ion batteries fire and explosion: a critical review”, *Journal of Energy Storage*, vol. 88, p. 111 532, May 2024, ISSN: 2352152X. DOI: 10.1016/j.est.2024.111532.
- [44] M. Held, M. Tuchschnid, M. Zennegg, R. Figi, C. Schreiner, L. D. Mellert, U. Welte, M. Kompatscher, M. Hermann, and L. Nachef, “Thermal runaway and fire of electric vehicle lithium-ion battery and contamination of infrastructure facility”, *Renewable and Sustainable Energy Reviews*, vol. 165, p. 112 474, Sep. 2022, ISSN: 13640321. DOI: 10.1016/j.rser.2022.112474.

- [45] B. Zhang, L. Pang, X. Shen, and Y. Gao, “Measurement and prediction of detonation cell size in binary fuel blends of methane/hydrogen mixtures”, *Fuel*, vol. 172, pp. 196–199, May 2016, ISSN: 00162361. DOI: 10.1016/j.fuel.2016.01.034.
- [46] V. Rodriguez, V. Monnier, P. Vidal, and R. Zitoun, “Non-dimensionalized distances and limits for the transition of deflagration to detonation”, *Shock Waves*, vol. 32, no. 5, pp. 417–425, Jul. 2022, ISSN: 0938-1287, 1432-2153. DOI: 10.1007/s00193-022-01088-0.
- [47] Y. Hou, X. Liu, M. Lei, X. Lv, X. Yu, X. Yan, and J. Yu, “Detonation behaviors in stoichiometric CH₄-h₂-o₂ under different initial pressures conditions”, *Fuel*, vol. 349, p. 128746, Oct. 2023, ISSN: 00162361. DOI: 10.1016/j.fuel.2023.128746.
- [48] J. M. Austin and J. E. Shepherd, “Detonations in hydrocarbon fuel blends”, *Combustion and Flame*, vol. 132, pp. 73–90, 2003. DOI: 10.1016/S0010-2180(02)00422-4.
- [49] L.-Q. Wang, H.-H. Ma, Z.-W. Shen, Y.-F. Cheng, and D.-G. Chen, “Detonation behaviors of syngas-oxygen in round and square tubes”, *International Journal of Hydrogen Energy*, vol. 43, no. 31, pp. 14775–14786, Aug. 2018, ISSN: 03603199. DOI: 10.1016/j.ijhydene.2018.05.163.
- [50] H. O. Barthel, “Predicted spacings in hydrogen-oxygen-argon detonations”, *The Physics of Fluids*, vol. 17, no. 8, pp. 1547–1553, 1974.
- [51] D. W. Stamps, S. E. Slezak, and S. R. Tieszen, “Observations of the cellular structure of fuel-air detonations”, *Combustion and Flame*, vol. 144, no. 1, pp. 289–298, Jan. 2006, ISSN: 00102180. DOI: 10.1016/j.combustflame.2005.06.016.
- [52] R. A. Strehlow, R. E. Maurer, and S. Rajan, “Transverse waves in detonations. spacing in the hydrogen-oxygen system.”, *AIAA Journal*, vol. 7, no. 2, pp. 323–328, 1969. DOI: <https://doi.org/10.2514/3.5093>.
- [53] Y. N. Denisov, “Structure of gaseous detonation in tubes”, *Z. Tekh. Fiz.*, vol. 450, 1960.
- [54] D. Desbordes, “Aspects stationnaires et transitoires de la détonation dans les gaz: relation avec la structure cellulaire du front”, Ph.D. dissertation, Poitiers, 1990.
- [55] R. Zitoun, D. Desbordes, C. Guerraud, and B. Deshaies, “Direct initiation of detonation in cryogenic gaseous h₂-o₂ mixtures”, *Shock Waves*, vol. 4, no. 6, pp. 331–337, 1995.
- [56] S. Abid, G. Dupré, and C. Paillard, “Oxidation of gaseous unsymmetrical dimethylhydrazine at high temperatures and detonation of UDMH/O₂ mixtures”, *Progress in Astronautics and Aeronautics*, vol. 153, pp. 162–162, 1993.
- [57] M. Pedley, C. Bishop, F. Benz, C. Bennett, and R. McClenagan, “Hydrazine vapor detonations”, in *International Colloquium on Dynamics of Explosions and Reactive Systems*, 1988.
- [58] Y. B. Zeldovich, “On the theory of detonation propagation in gaseous systems”, *Zh. Eksp. Teor. Fiz*, vol. 10, no. 5, pp. 542–568, 1940.

- [59] J. Von Neumann, “Theory of detonation waves”, *John von Neumann, collected works*, vol. 6, pp. 203–218, 1942.
- [60] W. Döring, “On detonation processes in gases”, *Ann. phys*, vol. 43, no. 421-436, p. 9, 1943.
- [61] S. Kao, J. Ziegler, N. Bitter, B. Schmidt, J. Lawson, and J. Shepherd, “SDToolbox: numerical tools for shock and detonation wave modelling”, CalTech, GALCIT Report FM2018.001, 2023.
- [62] H. Ng, Y. Ju, and J. Lee, “Assessment of detonation hazards in high-pressure hydrogen storage from chemical sensitivity analysis”, *International Journal of Hydrogen Energy*, vol. 32, no. 1, pp. 93–99, Jan. 2007, ISSN: 03603199. DOI: 10.1016/j.ijhydene.2006.03.012.
- [63] V. I. Manzhalei, V. V. Mitrofanov, and V. A. Subbotin, “Measurement of inhomogeneities of a detonation front in gas mixtures at elevated pressures”, *Combustion, Explosion and Shock Waves*, vol. 10, no. 1, pp. 89–95, 1974.
- [64] Y. Chen, B. Liu, Y. Zhang, D. Zhang, S. T. Revankar, W. Tian, S. Qiu, and G. Su, “Effects of nitrogen and carbon monoxide on the detonation of hydrogen-air gaseous mixtures”, *Nuclear Engineering and Design*, vol. 343, pp. 1–10, Mar. 2019, ISSN: 00295493. DOI: 10.1016/j.nucengdes.2018.12.014.
- [65] J. Crane, X. Shi, and H. Wang, “A comparison of methane and natural gas detonation limit behaviors”, in *AIAA Scitech 2020 Forum*, Orlando, FL: American Institute of Aeronautics and Astronautics, Jan. 6, 2020, ISBN: 978-1-62410-595-1. DOI: 10.2514/6.2020-0445.
- [66] J. Crane, X. Shi, R. Xu, and H. Wang, “Natural gas versus methane: ignition kinetics and detonation limit behavior in small tubes”, *Combustion and Flame*, vol. 237, p. 111719, Mar. 2022, ISSN: 00102180. DOI: 10.1016/j.combustflame.2021.111719.
- [67] G. Ciccarelli, J. L. Boccio, T. Ginsberg, and H. Tagawa, “The influence of initial temperature on flame acceleration and deflagration-to-detonation transition”, *Twenty-Sixth Symposium (International) on Combustion/The Combustion Institute*, vol. 26, no. 2, pp. 2973–2979, 1996. DOI: 10.1016/S0082-0784(96)80140-8.
- [68] S. S.-M. Lau-Chapdelaine, J. Loiseau, R. Stowe, and P. Brousseau, “Force accounting methodology for airbreathing high-speed missiles: basic thermodynamic calculations of glycidyl azide polymer as a fuel for a detonation engine”,
- [69] M. Plaster, J. Lee, R. Mcclenagan, J. Shepherd, and F. Benz, “Detonation of cryogenic gaseous hydrogen-oxygen mixtures”, 1991.
- [70] G. Dupre, R. Knystautas, and J. Lee, “Near-limit propagation of detonation in tubes”, *Progress in Astronautics and Aeronautics*, vol. 106, pp. 244–259, 1986.
- [71] J. Lee, R. Knystautas, and C. Chan, “Turbulent flame propagation in obstacle-filled tubes”, *Symposium (International) on Combustion*, vol. 20, no. 1, pp. 1663–1672, Jan. 1985, ISSN: 00820784. DOI: 10.1016/S0082-0784(85)80662-7.

- [72] J. E. Shepherd, “Chemical kinetics of hydrogen-air-diluent detonations”, in *Dynamics of Explosions, American Institute of Aeronautics and Astronautics*, J. R. Bowen *et al.*, Eds., vol. 106, New York: AIAA, 1986, pp. 263–293.
- [73] J. Li, Z. W. Zhao, A. Kazakov, and F. L. Dryer, “An updated comprehensive kinetic model of hydrogen combustion”, *International Journal of Chemical Kinetics*, vol. 36, pp. 566–575, 2004.
- [74] A. Konnov, “Detailed reaction mechanism for small hydrocarbons combustion. release 0.5”, 2000.
- [75] J. E. Shepherd and S. R. Tieszen, “Detonation cellular structure and image processing”, Sandia National Labs., Albuquerque, NM (USA), Jan. 1986.
- [76] M. Kaneshige and J. E. Shepherd, “Detonation database”, GALCIT, Technical Report FM97-8, Jul. 1997, See also the electronic hypertext version at http://www.galcit.caltech.edu/detn_db/html/.
- [77] H. D. Ng, M. I. Radulescu, A. J. Higgins, N. Nikiforakis, and J. H. S. Lee, “Numerical investigation of the instability for one-dimensional chapman–jouguet detonations with chain-branching kinetics”, *Combustion Theory and Modelling*, vol. 9, no. 3, pp. 385–401, Aug. 2005, ISSN: 1364-7830, 1741-3559. DOI: 10.1080/13647830500307758.
- [78] G. Bakalis and H. D. Ng, “Detonation cell size prediction using artificial neural networks (ANNs) for hydrogen / hydrocarbon / ammonia / nitrous oxide mixtures”, *Energies*, vol. 17, no. 7, p. 1747, Apr. 5, 2024, ISSN: 1996-1073. DOI: 10.3390/en17071747.
- [79] A. A. Vasil’ev, “Cell size as the main geometric parameter of a multifront detonation wave”, *Journal of Propulsion and Power*, vol. 22, no. 6, pp. 1245–1260, 2006. DOI: 10.2514/1.20348.
- [80] A. Vasil’ev, “Dynamic parameters of detonation”, in *Shock Waves Science and Technology Library, Vol. 6* (Shock Wave Science and Technology Reference Library), F. Zhang, Ed., Shock Wave Science and Technology Reference Library. Berlin, Heidelberg: Springer, 2012, vol. 6. DOI: 10.1007/978-3-642-22967-1_4.
- [81] H. O. Barthel, “Reaction zone-shock front coupling in detonations”, *The Physics of Fluids*, vol. 15, no. 1, pp. 43–50, 1972.
- [82] K. Chiu and J. Lee, “A simplified version of the barthel model for transverse wave spacings in gaseous detonation”, *Combustion and Flame*, vol. 26, pp. 353–361, 1976.
- [83] R. Strehlow, “Multi-dimensional detonation wave structure”, *Astronautica Acta*, vol. 15, pp. 345–357, 1970.
- [84] E. A. Lundstrom and A. K. Oppenheim, “On the influence of non-steadiness on the thickness of the detonation wave”, *Proceedings of the Royal Society of London. A. Mathematical and Physical Sciences*, vol. 310, no. 1503, pp. 463–478, Jun. 10, 1969, ISSN: 0080-4630. DOI: 10.1098/rspa.1969.0087.
- [85] A. A. Vasil’ev and Y. A. Nikolaev, “The model of cell of multifront gaseous detonation”, *Combustion, Explosion, and Shock Waves*, vol. 12, no. 5, pp. 744–754, 1976.

- [86] A. A. Vasil'ev, M. E. Topchian, and V. Y. Ulianitsky, "Influence of initial temperature on parameters of gaseous detonation", *Combustion, Explosion, and Shock Waves*, vol. 15, no. 6, pp. 149–152, 1979.
- [87] A. A. Vasiljev and J. A. Nikolaev, "Closed theoretical model of a detonation cell", *Acta Astronautica*, vol. 5, no. 11-12, pp. 983–996, 1978.
- [88] A. A. Vasil'ev, Y. A. Nikolaev, and V. Y. Ulianitsky, "Calculation of parameters of cell of multifront gaseous detonation", *Combustion, Explosion, and Shock Waves*, vol. 13, no. 3, pp. 404–408, 1977, (in Russian).
- [89] J. Crane, X. Shi, J. T. Lipkowicz, A. M. Kempf, and H. Wang, "Geometric modeling and analysis of detonation cellular stability", *Proceedings of the Combustion Institute*, vol. 38, no. 3, pp. 3585–3593, 2021. DOI: 10.1016/j.proci.2020.06.278.
- [90] K. Malik, M. Żbikowski, and A. Teodorczyk, "Detonation cell size model based on deep neural network for hydrogen, methane and propane mixtures with air and oxygen", *Nuclear Engineering and Technology*, vol. 51, no. 2, pp. 424–431, Apr. 2019, ISSN: 17385733. DOI: 10.1016/j.net.2018.11.004.
- [91] S. Siatkowski, K. Wacko, and J. Kindracki, "Predicting detonation cell size of bio-gas–oxygen mixtures using machine learning models", *Shock Waves*, vol. 34, no. 2, pp. 129–137, Apr. 2024, ISSN: 0938-1287, 1432-2153. DOI: 10.1007/s00193-024-01164-7.
- [92] G. J. Sharpe and M. I. Radulescu, "Statistical analysis of cellular detonation dynamics from numerical simulations: one-step chemistry", *Combustion Theory and Modelling*, vol. 15, no. 5, pp. 691–723, Oct. 2011, ISSN: 1364-7830, 1741-3559. DOI: 10.1080/13647830.2011.558594.
- [93] J. Shepherd, I. Moen, S. Murray, and P. Thibault, "Analyses of the cellular structure of detonations", *Symposium (International) on Combustion*, vol. 21, no. 1, pp. 1649–1658, Jan. 1988, ISSN: 00820784. DOI: 10.1016/S0082-0784(88)80398-9.
- [94] D. C. Montgomery and G. C. Runger, *Applied Statistics and Probability for Engineers*, 7th ed. John Wiley & Sons, 2021, ISBN: 9781119492443.
- [95] P. Virtanen, R. Gommers, T. E. Oliphant, M. Haberland, T. Reddy, D. Cournapeau, E. Burovski, P. Peterson, W. Weckesser, J. Bright, S. J. van der Walt, M. Brett, J. Wilson, K. J. Millman, N. Mayorov, A. R. J. Nelson, E. Jones, R. Kern, E. Larson, C. J. Carey, Í. Polat, Y. Feng, E. W. Moore, J. VanderPlas, D. Laxalde, J. Perktold, R. Cimrman, I. Henriksen, E. A. Quintero, C. R. Harris, A. M. Archibald, A. H. Ribeiro, F. Pedregosa, P. van Mulbregt, and SciPy 1.0 Contributors, "SciPy 1.0: Fundamental Algorithms for Scientific Computing in Python", *Nature Methods*, vol. 17, pp. 261–272, 2020. DOI: 10.1038/s41592-019-0686-2.
- [96] W. G. Cochran, "Some methods for strengthening the common X2 tests", *Biometrics*, vol. 10, pp. 417–451, 4 1954. DOI: 10.2307/3001616.
- [97] R. B. D'Agostino and M. A. Stephens, *Goodness-of-Fit Techniques* (Statistics: Textbooks and Monographs). New York: Marcel Dekker, 1986, vol. 68, ISBN: 9780824774875.

- [98] U.S. National Institute of Standards and Technology. “1.3.6.6.9. lognormal distribution”. Accessed: 2025-04-13. (2020), [Online]. Available: <https://www.itl.nist.gov/div898/handbook/eda/section3/eda3669.htm>.
- [99] B. Zhang, H. D. Ng, and J. H. Lee, “Measurement and relationship between critical tube diameter and critical energy for direct blast initiation of gaseous detonations”, *Journal of Loss Prevention in the Process Industries*, vol. 26, no. 6, pp. 1293–1299, Nov. 2013, ISSN: 09504230. DOI: 10.1016/j.jlp.2013.07.011.
- [100] PCB Piezotronics, Inc. “High frequency icp[®] pressure sensor - model 113b21”. Accessed May 2025. (2023), [Online]. Available: <https://www.pcb.com/products?m=113B21>.
- [101] PCB Piezotronics, Inc. “Introduction to piezoelectric pressure sensors”. Application Note AP-Pressure-001, Accessed May 2025. (2021), [Online]. Available: <https://www.pcb.com/resources/technical-information/introduction-to-pressure-sensors>.
- [102] Mechanical and Aerospace Engineering (Combustion Research). “The San Diego mechanism - version 2016-12-14 chemical-kinetic mechanisms for combustion applications”, University of California, San Diego. (2016), [Online]. Available: <https://web.eng.ucsd.edu/mae/groups/combustion/mechanism.html>.
- [103] J. M. Austin and J. E. Shepherd, “Carbon monoxide detonations”, *Shock Waves*, vol. 4, pp. 331–337, Apr. 1995. DOI: 10.1007/BF01413875.
- [104] C. K. Westbrook and P. A. Urtiew, “Use of chemical kinetics to predict critical parameters of gaseous detonations”, *Combustion, Explosion and Shock Waves*, vol. 19, no. 6, pp. 753–766, 1983.
- [105] R. G. Budynas and J. K. Nisbett, *Mechanical Engineering Design*, 9th ed. McGraw-Hill, 2011.
- [106] Swagelok. “Swagelok products”. (2024), [Online]. Available: <https://www.swagelok.com/en> (visited on 08/08/2024).
- [107] C. Brown, R. Jordan, and D. Tucholski, “Furnace co emissions under normal and compromised vent conditions”, The United States Consumer Product Safety Commission, Washington, D.C., Oct. 2000.
- [108] National Fire Protection Association, *National Fuel Gas Code, 2018 Edition*. Quincy, Massachusetts; Washington, DC: National Fire Protection Association; American Gas Association, 2017.
- [109] Office of Transportation and Air Quality, “Light-duty vehicles and light-duty trucks: clean fuel fleet exhaust emission standards”, United States Environmental Protection Agency, Mar. 2016.
- [110] Government of Ontario. “Current occupational exposure limits for ontario workplaces under regulation 833”. (2024), [Online]. Available: <https://www.ontario.ca/page/current-occupational-exposure-limits-ontario-workplaces-under-regulation-833> (visited on 08/08/2024).

- [111] Ministry of Municipal Affairs and Housing, *2024 building code compendium volume 1*, May 29, 2024.
- [112] McMaster-Carr. “Wall-mount hazardous location fume exhauster”. (Aug. 8, 2024), [Online]. Available: <https://www.mcmaster.com/1951K7/> (visited on 08/08/2024).
- [113] National Defence, *A-GA-135-001/AA-001 Flight Safety for the Canadian Armed Forces*. Jul. 2015.

Appendix A

Experimental and Literature Data

Table A.1 – Cell width and detonation velocity data for experimental results of this study and literature data for mixtures comprised of H₂, CH₄, CO [76]

T_1 [K]	P_1 [Pa]	Mixture (mole basis)	$\lambda_{\text{avg}}^{\text{max}}_{\text{min}}$ [mm]	Velocity [m/s]	Ref
291.2	49990	0.08 H ₂ + 0.25 CH ₄ + 0.08 CO + 0.58 O ₂	8.39 ^{19.7} _{2.84}	2331	
291.1	200000	0.08 H ₂ + 0.25 CH ₄ + 0.08 CO + 0.58 O ₂	2.86 ^{4.63} _{1.86}	2418	
291.1	200000	0.08 H ₂ + 0.25 CH ₄ + 0.08 CO + 0.58 O ₂	2.85 ^{4.17} _{1.63}	2418	
291.5	100020	0.08 H ₂ + 0.25 CH ₄ + 0.08 CO + 0.58 O ₂	5.57 ^{14.6} _{2.45}	2373	
291.1	99990	0.08 H ₂ + 0.25 CH ₄ + 0.08 CO + 0.58 O ₂	4.39 ^{8.02} _{2.19}	2382	
290.4	20030	0.08 H ₂ + 0.25 CH ₄ + 0.08 CO + 0.58 O ₂	32.1 ⁵⁰ _{16.6}	2258	
290.7	100050	0.08 H ₂ + 0.25 CH ₄ + 0.08 CO + 0.58 O ₂	6.23 ^{12.8} _{2.76}	-	
290.7	200020	0.19 H ₂ + 0.19 CH ₄ + 0.10 CO + 0.52 O ₂	1.78 ^{4.72} _{0.42}	2431	
290.8	100020	0.19 H ₂ + 0.19 CH ₄ + 0.10 CO + 0.52 O ₂	5.46 ^{7.89} _{3.29}	2398	
291.2	100000	0.19 H ₂ + 0.19 CH ₄ + 0.10 CO + 0.52 O ₂	4.34 ^{7.45} _{1.55}	2397	
291.2	20010	0.19 H ₂ + 0.19 CH ₄ + 0.10 CO + 0.52 O ₂	13.8 ^{34.7} _{1.86}	2309	
291.3	50000	0.19 H ₂ + 0.19 CH ₄ + 0.10 CO + 0.52 O ₂	4.15 ^{8.25} _{1.96}	2355	
289.8	20000	0.33 H ₂ + 0.11 CH ₄ + 0.11 CO + 0.44 O ₂	12.1 ^{26.4} _{3.26}	2352	
289.9	200010	0.33 H ₂ + 0.11 CH ₄ + 0.11 CO + 0.44 O ₂	-	2471	
290.6	100020	0.33 H ₂ + 0.11 CH ₄ + 0.11 CO + 0.44 O ₂	3.25 ^{4.93} _{1.92}	2435	
289.9	100060	0.33 H ₂ + 0.11 CH ₄ + 0.11 CO + 0.44 O ₂	4.58 ^{6.5} _{2.99}	2442	
290.2	50030	0.33 H ₂ + 0.11 CH ₄ + 0.11 CO + 0.44 O ₂	4.27 ^{7.42} _{1.97}	2387	
290.2	200060	0.22 H ₂ + 0.11 CH ₄ + 0.22 CO + 0.44 O ₂	2.87 ^{4.25} _{1.61}	2299	
290.5	100070	0.22 H ₂ + 0.11 CH ₄ + 0.22 CO + 0.44 O ₂	4.45 ^{6.35} _{2.55}	2265	
290.5	50000	0.22 H ₂ + 0.11 CH ₄ + 0.22 CO + 0.44 O ₂	5.78 ^{10.7} _{3.03}	2224	
290.5	100050	0.22 H ₂ + 0.11 CH ₄ + 0.22 CO + 0.44 O ₂	4.21 ^{7.37} _{0.574}	2257	
289.8	20060	0.22 H ₂ + 0.11 CH ₄ + 0.22 CO + 0.44 O ₂	22.2 ^{65.1} _{10.2}	2170	
290.0	200020	0.11 H ₂ + 0.11 CH ₄ + 0.33 CO + 0.44 O ₂	5.5 ^{10.2} _{2.39}	2161	
290.1	99980	0.11 H ₂ + 0.11 CH ₄ + 0.33 CO + 0.44 O ₂	5.33 ^{13.6} _{1.86}	2126	

T_1 [K]	P_1 [Pa]	Mixture (mole basis)	$\lambda_{\text{avg}}^{\text{max}} _{\text{min}}$ [mm]	Velocity [m/s]	Ref
290.2	50040	0.11 H ₂ + 0.11 CH ₄ + 0.33 CO + 0.44 O ₂	10.1 ^{22.4} _{4.94}	2086	
290.3	100000	0.11 H ₂ + 0.11 CH ₄ + 0.33 CO + 0.44 O ₂	6.7 ^{10.8} _{3.95}	2129	
290.7	20010	0.11 H ₂ + 0.11 CH ₄ + 0.33 CO + 0.44 O ₂	41.8 ^{60.4} _{12.4}	2043	
290.5	20040	0.10 H ₂ + 0.19 CH ₄ + 0.19 CO + 0.52 O ₂	49.9 ^{81.9} _{14.2}	2173	
290.6	200010	0.10 H ₂ + 0.19 CH ₄ + 0.19 CO + 0.52 O ₂	3.21 ^{5.92} _{1.04}	2298	
291.1	99990	0.10 H ₂ + 0.19 CH ₄ + 0.19 CO + 0.52 O ₂	6.32 ^{11.5} _{2.39}	2263	
291.3	100100	0.10 H ₂ + 0.19 CH ₄ + 0.19 CO + 0.52 O ₂	5.67 ^{10.8} _{3.23}	2272	
290.5	50020	0.10 H ₂ + 0.19 CH ₄ + 0.19 CO + 0.52 O ₂	11.3 ^{24.4} _{6.68}	2229	
291.0	20000	0.22 CH ₄ + 0.22 CO + 0.56 O ₂	38.3 ^{75.6} _{10.3}	2124	
291.6	50060	0.22 CH ₄ + 0.22 CO + 0.56 O ₂	13.6 ^{26.5} _{5.95}	2190	
291.2	200000	0.22 CH ₄ + 0.22 CO + 0.56 O ₂	4.58 ^{7.36} _{2.13}	2254	
291.3	100000	0.22 CH ₄ + 0.22 CO + 0.56 O ₂	8.34 ^{11.5} _{1.34}	2216	
291.5	100010	0.22 CH ₄ + 0.22 CO + 0.56 O ₂	8.55 ^{13.2} _{5.37}	2214	
291.6	20070	0.13 CH ₄ + 0.40 CO + 0.47 O ₂	35.7 ^{54.1} _{22.3}	1950	
291.6	50060	0.13 CH ₄ + 0.40 CO + 0.47 O ₂	47.5 ^{59.6} _{36.9}	1992	
291.8	200010	0.13 CH ₄ + 0.40 CO + 0.47 O ₂	6.32 ¹¹ _{2.93}	2080	
291.8	19990	0.13 CH ₄ + 0.40 CO + 0.47 O ₂	-	2010	
292.1	100010	0.13 CH ₄ + 0.40 CO + 0.47 O ₂	17.2 ^{29.4} _{6.62}	2047	
291.9	100000	0.13 CH ₄ + 0.40 CO + 0.47 O ₂	11.6 ^{18.4} _{3.85}	2038	
292.3	200000	0.29 CH ₄ + 0.10 CO + 0.62 O ₂	2.97 ^{4.97} _{1.61}	2369	
291.3	20040	0.29 CH ₄ + 0.10 CO + 0.62 O ₂	35.3 ⁴⁴ _{20.3}	2228	
291.5	50020	0.29 CH ₄ + 0.10 CO + 0.62 O ₂	11.8 ^{26.7} _{4.77}	2288	
290.7	100010	0.29 CH ₄ + 0.10 CO + 0.62 O ₂	5.77 ^{9.66} _{2.9}	2339	
290.8	100040	0.29 CH ₄ + 0.10 CO + 0.62 O ₂	5.51 ^{10.5} ₃	2336	
293.3	20000	0.67 H ₂ + 0.33 O ₂	8.09 ^{18.6} _{2.59}	2702	
293.3	14998	0.67 H ₂ + 0.33 O ₂	10.9 ^{22.4} _{4.48}	2706	
291.5	12515	0.67 H ₂ + 0.33 O ₂	13.2 ^{23.3} _{4.71}	2626	
293.0	12507	0.67 H ₂ + 0.33 O ₂	12.3 ^{24.6} _{5.09}	2634	
293.0	10031	1 CH ₄ + 2 H ₂ + 3 O ₂	35 ²⁰ ₅₀		[45]
293.0	13030	1 CH ₄ + 2 H ₂ + 3 O ₂	31.1 ^{25.2} _{36.7}		[45]
293.0	17011	1 CH ₄ + 2 H ₂ + 3 O ₂	25 ^{16.5} _{33.5}		[45]
293.0	20010	1 CH ₄ + 2 H ₂ + 3 O ₂	16.9 ^{15.4} _{25.4}		[45]
293.0	22027	1 CH ₄ + 2 H ₂ + 3 O ₂	19.8 ^{14.2} ₂₃		[45]
293.0	26008	1 CH ₄ + 2 H ₂ + 3 O ₂	16.6 ¹⁰ _{18.5}		[45]
293.0	29990	1 CH ₄ + 2 H ₂ + 3 O ₂	10.2 ^{8.66} _{11.9}		[45]
293.0	6016	1 CH ₄ + 1 H ₂ + 2.50 O ₂	73.8 ^{55.7} _{91.8}		[45]
293.0	7988	1 CH ₄ + 1 H ₂ + 2.50 O ₂	78.5 ⁵¹ ₁₀₆		[45]
293.0	10061	1 CH ₄ + 1 H ₂ + 2.50 O ₂	46.9 ^{46.6} _{46.9}		[45]
293.0	12993	1 CH ₄ + 1 H ₂ + 2.50 O ₂	39.3 ^{34.9} ₄₃		[45]
293.0	17037	1 CH ₄ + 1 H ₂ + 2.50 O ₂	26.1 ^{23.8} _{28.4}		[45]
293.0	20020	1 CH ₄ + 1 H ₂ + 2.50 O ₂	25.6 ^{23.3} _{28.2}		[45]
293.0	22042	1 CH ₄ + 1 H ₂ + 2.50 O ₂	20.7 ^{20.7} _{20.7}		[45]

T_1 [K]	P_1 [Pa]	Mixture (mole basis)	$\lambda_{\text{avg}}^{\text{max}} _{\text{min}}$ [mm]	Velocity [m/s]	Ref
293.0	27048	1 CH ₄ + 1 H ₂ + 2.50 O ₂	19.3 ^{19.3} _{19.3}		[45]
293.0	29980	1 CH ₄ + 1 H ₂ + 2.50 O ₂	16.4 ^{16.4} _{16.7}		[45]
293.0	10041	1 CH ₄ + 4 H ₂ + 4 O ₂	33.2 ^{30.7} _{35.6}		[45]
293.0	12997	1 CH ₄ + 4 H ₂ + 4 O ₂	19.1 ^{17.1} ₂₁		[45]
293.0	17023	1 CH ₄ + 4 H ₂ + 4 O ₂	15.3 ^{13.5} _{16.8}		[45]
293.0	22069	1 CH ₄ + 4 H ₂ + 4 O ₂	11.6 ^{10.1} _{13.1}		[45]
293.0	26045	1 CH ₄ + 4 H ₂ + 4 O ₂	9.08 ^{9.08} _{9.08}		[45]
293.0	30020	1 CH ₄ + 4 H ₂ + 4 O ₂	7.43 ^{7.43} _{7.43}		[45]
293.0	10031	1 CH ₄ + 2 H ₂ + 3 O ₂	35 ²⁰ ₅₀		[45]
293.0	13030	1 CH ₄ + 2 H ₂ + 3 O ₂	31.1 ^{25.2} _{36.7}		[45]
293.0	17011	1 CH ₄ + 2 H ₂ + 3 O ₂	25 ^{16.5} _{33.5}		[45]
293.0	20010	1 CH ₄ + 2 H ₂ + 3 O ₂	16.9 ^{15.4} _{25.4}		[45]
293.0	22027	1 CH ₄ + 2 H ₂ + 3 O ₂	19.8 ^{14.2} ₂₃		[45]
293.0	26008	1 CH ₄ + 2 H ₂ + 3 O ₂	16.6 ¹⁰ _{18.5}		[45]
293.0	29990	1 CH ₄ + 2 H ₂ + 3 O ₂	10.2 ^{8.66} _{11.9}		[45]
293.0	6016	1 CH ₄ + 1 H ₂ + 2.50 O ₂	73.8 ^{55.7} _{91.8}		[45]
293.0	7988	1 CH ₄ + 1 H ₂ + 2.50 O ₂	78.5 ⁵¹ ₁₀₆		[45]
293.0	10061	1 CH ₄ + 1 H ₂ + 2.50 O ₂	46.9 ^{46.6} _{46.9}		[45]
293.0	12993	1 CH ₄ + 1 H ₂ + 2.50 O ₂	39.3 ^{34.9} ₄₃		[45]
293.0	17037	1 CH ₄ + 1 H ₂ + 2.50 O ₂	26.1 ^{23.8} _{28.4}		[45]
293.0	20020	1 CH ₄ + 1 H ₂ + 2.50 O ₂	25.6 ^{23.3} _{28.2}		[45]
293.0	22042	1 CH ₄ + 1 H ₂ + 2.50 O ₂	20.7 ^{20.7} _{20.7}		[45]
293.0	27048	1 CH ₄ + 1 H ₂ + 2.50 O ₂	19.3 ^{19.3} _{19.3}		[45]
293.0	29980	1 CH ₄ + 1 H ₂ + 2.50 O ₂	16.4 ^{16.4} _{16.7}		[45]
293.0	10041	1 CH ₄ + 4 H ₂ + 4 O ₂	33.2 ^{30.7} _{35.6}		[45]
293.0	12997	1 CH ₄ + 4 H ₂ + 4 O ₂	19.1 ^{17.1} ₂₁		[45]
293.0	17023	1 CH ₄ + 4 H ₂ + 4 O ₂	15.3 ^{13.5} _{16.8}		[45]
293.0	22069	1 CH ₄ + 4 H ₂ + 4 O ₂	11.6 ^{10.1} _{13.1}		[45]
293.0	26045	1 CH ₄ + 4 H ₂ + 4 O ₂	9.08 ^{9.08} _{9.08}		[45]
293.0	30020	1 CH ₄ + 4 H ₂ + 4 O ₂	7.43 ^{7.43} _{7.43}		[45]
294.0	23950	0.50 H ₂ + 0.50 CH ₄ + 1.25 O ₂	16.9		[46]
294.0	24350	0.75 H ₂ + 0.25 CH ₄ + 0.88 O ₂	11.4		[46]
294.0	27600	0.75 H ₂ + 0.25 CH ₄ + 0.88 O ₂	10.5		[46]
294.0	32200	0.75 H ₂ + 0.25 CH ₄ + 0.88 O ₂	8.7		[46]
294.0	12000	0.50 H ₂ + 0.50 CH ₄ + 1.25 O ₂	31.9		[46]
294.0	11410	0.50 H ₂ + 0.50 CH ₄ + 1.25 O ₂	33.7		[46]
294.0	12200	0.25 H ₂ + 0.75 CH ₄ + 1.62 O ₂	41.6		[46]
294.0	11900	0.25 H ₂ + 0.75 CH ₄ + 1.62 O ₂	42.6		[46]
294.0	23670	0.75 H ₂ + 0.25 CH ₄ + 0.88 O ₂	18.4		[46]
294.0	14660	0.50 H ₂ + 0.50 CH ₄ + 1.25 O ₂	26.1		[46]
294.0	15200	0.25 H ₂ + 0.75 CH ₄ + 1.62 O ₂	32.5		[46]
294.0	14140	0.25 H ₂ + 0.75 CH ₄ + 1.62 O ₂	35.3		[46]

T_1 [K]	P_1 [Pa]	Mixture (mole basis)	$\lambda_{\text{avg}}^{\text{min}}$ [mm]	Velocity [m/s]	Ref
294.0	22140	0.75 H ₂ + 0.25 CH ₄ + 0.88 O ₂	12.8		[46]
294.0	18970	0.50 H ₂ + 0.50 CH ₄ + 1.25 O ₂	20.7		[46]
294.0	18520	0.50 H ₂ + 0.50 CH ₄ + 1.25 O ₂	21.2		[46]
294.0	21670	0.25 H ₂ + 0.75 CH ₄ + 1.62 O ₂	23.8		[46]
294.0	21160	0.25 H ₂ + 0.75 CH ₄ + 1.62 O ₂	24.4		[46]
300.0	100000	9 CH ₄ + 1 H ₂ + 18.50 O ₂	4.6		[47]
300.0	100000	9 CH ₄ + 1 H ₂ + 18.50 O ₂	4.3		[47]
300.0	100000	9 CH ₄ + 1 H ₂ + 18.50 O ₂	4		[47]
300.0	100000	4 CH ₄ + 1 H ₂ + 8.50 O ₂	4.5		[47]
300.0	100000	4 CH ₄ + 1 H ₂ + 8.50 O ₂	4		[47]
300.0	100000	4 CH ₄ + 1 H ₂ + 8.50 O ₂	3.5		[47]
300.0	100000	2.33 CH ₄ + 1 H ₂ + 5.17 O ₂	4.2		[47]
300.0	100000	2.33 CH ₄ + 1 H ₂ + 5.17 O ₂	3.6		[47]
300.0	100000	2.33 CH ₄ + 1 H ₂ + 5.17 O ₂	3		[47]
300.0	100000	1 CH ₄ + 1 H ₂ + 2.50 O ₂	2.7		[47]
300.0	100000	1 CH ₄ + 1 H ₂ + 2.50 O ₂	2.5		[47]
300.0	100000	1 CH ₄ + 1 H ₂ + 2.50 O ₂	2.3		[47]
300.0	200000	9 CH ₄ + 1 H ₂ + 18.50 O ₂	2.4		[47]
300.0	200000	9 CH ₄ + 1 H ₂ + 18.50 O ₂	2.2		[47]
300.0	200000	9 CH ₄ + 1 H ₂ + 18.50 O ₂	2.1		[47]
300.0	200000	4 CH ₄ + 1 H ₂ + 8.50 O ₂	2.3		[47]
300.0	200000	4 CH ₄ + 1 H ₂ + 8.50 O ₂	2.1		[47]
300.0	200000	4 CH ₄ + 1 H ₂ + 8.50 O ₂	1.9		[47]
300.0	200000	2.33 CH ₄ + 1 H ₂ + 5.17 O ₂	2.2		[47]
300.0	200000	2.33 CH ₄ + 1 H ₂ + 5.17 O ₂	2		[47]
300.0	200000	2.33 CH ₄ + 1 H ₂ + 5.17 O ₂	1.8		[47]
300.0	200000	1 CH ₄ + 1 H ₂ + 2.50 O ₂	1.5		[47]
300.0	200000	1 CH ₄ + 1 H ₂ + 2.50 O ₂	1.3		[47]
300.0	200000	1 CH ₄ + 1 H ₂ + 2.50 O ₂	1		[47]
300.0	300000	9 CH ₄ + 1 H ₂ + 18.50 O ₂	1.5		[47]
300.0	300000	9 CH ₄ + 1 H ₂ + 18.50 O ₂	1.3		[47]
300.0	300000	9 CH ₄ + 1 H ₂ + 18.50 O ₂	1.1		[47]
300.0	300000	4 CH ₄ + 1 H ₂ + 8.50 O ₂	1.2		[47]
300.0	300000	4 CH ₄ + 1 H ₂ + 8.50 O ₂	1		[47]
300.0	300000	4 CH ₄ + 1 H ₂ + 8.50 O ₂	0.8		[47]
300.0	300000	2.33 CH ₄ + 1 H ₂ + 5.17 O ₂	1		[47]
300.0	300000	2.33 CH ₄ + 1 H ₂ + 5.17 O ₂	0.9		[47]
300.0	300000	2.33 CH ₄ + 1 H ₂ + 5.17 O ₂	0.8		[47]
300.0	300000	1 CH ₄ + 1 H ₂ + 2.50 O ₂	0.9		[47]
300.0	300000	1 CH ₄ + 1 H ₂ + 2.50 O ₂	0.8		[47]
300.0	300000	1 CH ₄ + 1 H ₂ + 2.50 O ₂	0.7		[47]
295.0	100000	0.33 O ₂ + 0.03 H ₂ + 0.63 CO	5 ₇ ²		[48]

T_1 [K]	P_1 [Pa]	Mixture (mole basis)	$\lambda_{\text{avg}}^{\text{max}}_{\text{min}}$ [mm]	Velocity [m/s]	Ref
298.0	7945	1 CO + 1 H ₂ + 1 O ₂	50.5		[49]
298.0	10137	1 CO + 1 H ₂ + 1 O ₂	39.2		[49]
298.0	12808	1 CO + 1 H ₂ + 1 O ₂	20.5		[49]
298.0	12808	1 CO + 1 H ₂ + 1 O ₂	20.5		[49]
298.0	15000	1 CO + 1 H ₂ + 1 O ₂	19.9		[49]
298.0	14932	1 CO + 1 H ₂ + 1 O ₂	18.8		[49]
298.0	19863	1 CO + 1 H ₂ + 1 O ₂	14.9		[49]
298.0	19726	1 CO + 1 H ₂ + 1 O ₂	14		[49]
298.0	20000	1 CO + 1 H ₂ + 1 O ₂	13		[49]
298.0	24932	1 CO + 1 H ₂ + 1 O ₂	11.9		[49]
298.0	24932	1 CO + 1 H ₂ + 1 O ₂	11.3		[49]
298.0	24932	1 CO + 1 H ₂ + 1 O ₂	10.6		[49]
298.0	30000	1 CO + 1 H ₂ + 1 O ₂	8.83		[49]
298.0	30000	1 CO + 1 H ₂ + 1 O ₂	8.15		[49]
298.0	29932	1 CO + 1 H ₂ + 1 O ₂	7.55		[49]
298.0	34932	1 CO + 1 H ₂ + 1 O ₂	6.96		[49]
298.0	34932	1 CO + 1 H ₂ + 1 O ₂	6.96		[49]
298.0	34932	1 CO + 1 H ₂ + 1 O ₂	6.96		[49]
298.0	39932	1 CO + 1 H ₂ + 1 O ₂	5.77		[49]
298.0	39932	1 CO + 1 H ₂ + 1 O ₂	5.77		[49]
298.0	39932	1 CO + 1 H ₂ + 1 O ₂	5.77		[49]
298.0	45068	1 CO + 1 H ₂ + 1 O ₂	5.52		[49]
298.0	45068	1 CO + 1 H ₂ + 1 O ₂	5.52		[49]
298.0	45068	1 CO + 1 H ₂ + 1 O ₂	4.41		[49]
298.0	50068	1 CO + 1 H ₂ + 1 O ₂	4.58		[49]
298.0	50068	1 CO + 1 H ₂ + 1 O ₂	4.58		[49]
298.0	50068	1 CO + 1 H ₂ + 1 O ₂	4.58		[49]
298.0	55000	1 CO + 1 H ₂ + 1 O ₂	3.73		[49]
298.0	55000	1 CO + 1 H ₂ + 1 O ₂	3.73		[49]
298.0	55000	1 CO + 1 H ₂ + 1 O ₂	3.73		[49]
298.0	60068	1 CO + 1 H ₂ + 1 O ₂	3.56		[49]
298.0	60068	1 CO + 1 H ₂ + 1 O ₂	3.56		[49]
298.0	60068	1 CO + 1 H ₂ + 1 O ₂	3.56		[49]
298.0	9874	2 CO + 1 H ₂ + 1.50 O ₂	38.5		[49]
298.0	12823	2 CO + 1 H ₂ + 1.50 O ₂	27		[49]
298.0	14811	2 CO + 1 H ₂ + 1.50 O ₂	24.9		[49]
298.0	19817	2 CO + 1 H ₂ + 1.50 O ₂	19.3		[49]
298.0	19817	2 CO + 1 H ₂ + 1.50 O ₂	17.5		[49]
298.0	24823	2 CO + 1 H ₂ + 1.50 O ₂	14		[49]
298.0	24960	2 CO + 1 H ₂ + 1.50 O ₂	12.6		[49]
298.0	29897	2 CO + 1 H ₂ + 1.50 O ₂	11.3		[49]
298.0	29966	2 CO + 1 H ₂ + 1.50 O ₂	10.7		[49]

T_1 [K]	P_1 [Pa]	Mixture (mole basis)	$\lambda_{\text{avg}}^{\text{max}}_{\text{min}}$ [mm]	Velocity [m/s]	Ref
298.0	29829	2 CO + 1 H ₂ + 1.50 O ₂	10.1		[49]
298.0	34834	2 CO + 1 H ₂ + 1.50 O ₂	8.97		[49]
298.0	34971	2 CO + 1 H ₂ + 1.50 O ₂	8.5		[49]
298.0	35246	2 CO + 1 H ₂ + 1.50 O ₂	8.79		[49]
298.0	39977	2 CO + 1 H ₂ + 1.50 O ₂	7.26		[49]
298.0	39977	2 CO + 1 H ₂ + 1.50 O ₂	6.55		[49]
298.0	39977	2 CO + 1 H ₂ + 1.50 O ₂	6.55		[49]
298.0	44983	2 CO + 1 H ₂ + 1.50 O ₂	6.73		[49]
298.0	44983	2 CO + 1 H ₂ + 1.50 O ₂	6.08		[49]
298.0	44983	2 CO + 1 H ₂ + 1.50 O ₂	5.6		[49]
298.0	50057	2 CO + 1 H ₂ + 1.50 O ₂	5.43		[49]
298.0	50057	2 CO + 1 H ₂ + 1.50 O ₂	5.43		[49]
298.0	50057	2 CO + 1 H ₂ + 1.50 O ₂	5.43		[49]
298.0	55063	2 CO + 1 H ₂ + 1.50 O ₂	5.07		[49]
298.0	55063	2 CO + 1 H ₂ + 1.50 O ₂	5.07		[49]
298.0	54926	2 CO + 1 H ₂ + 1.50 O ₂	5.43		[49]
298.0	60069	2 CO + 1 H ₂ + 1.50 O ₂	4.01		[49]
298.0	60069	2 CO + 1 H ₂ + 1.50 O ₂	4.01		[49]
298.0	60069	2 CO + 1 H ₂ + 1.50 O ₂	4.01		[49]
298.0	9832	3 CO + 1 H ₂ + 2 O ₂	42.9		[49]
298.0	12997	3 CO + 1 H ₂ + 2 O ₂	27.6		[49]
298.0	14882	3 CO + 1 H ₂ + 2 O ₂	28.5		[49]
298.0	14882	3 CO + 1 H ₂ + 2 O ₂	28.5		[49]
298.0	19865	3 CO + 1 H ₂ + 2 O ₂	26.6		[49]
298.0	19865	3 CO + 1 H ₂ + 2 O ₂	26.6		[49]
298.0	20000	3 CO + 1 H ₂ + 2 O ₂	23.4		[49]
298.0	24916	3 CO + 1 H ₂ + 2 O ₂	17.5		[49]
298.0	24916	3 CO + 1 H ₂ + 2 O ₂	16.1		[49]
298.0	24916	3 CO + 1 H ₂ + 2 O ₂	16.1		[49]
298.0	30034	3 CO + 1 H ₂ + 2 O ₂	12.4		[49]
298.0	30034	3 CO + 1 H ₂ + 2 O ₂	11.3		[49]
298.0	30034	3 CO + 1 H ₂ + 2 O ₂	11.3		[49]
298.0	34882	3 CO + 1 H ₂ + 2 O ₂	11		[49]
298.0	35152	3 CO + 1 H ₂ + 2 O ₂	10		[49]
298.0	35152	3 CO + 1 H ₂ + 2 O ₂	10		[49]
298.0	39933	3 CO + 1 H ₂ + 2 O ₂	8.06		[49]
298.0	39933	3 CO + 1 H ₂ + 2 O ₂	8.06		[49]
298.0	40000	3 CO + 1 H ₂ + 2 O ₂	10.2		[49]
298.0	45051	3 CO + 1 H ₂ + 2 O ₂	9.34		[49]
298.0	44983	3 CO + 1 H ₂ + 2 O ₂	7.07		[49]
298.0	44983	3 CO + 1 H ₂ + 2 O ₂	7.07		[49]
298.0	50101	3 CO + 1 H ₂ + 2 O ₂	7.14		[49]

T_1 [K]	P_1 [Pa]	Mixture (mole basis)	$\lambda_{\text{avg}} _{\text{min}}^{\text{max}}$ [mm]	Velocity [m/s]	Ref
298.0	50034	3 CO + 1 H ₂ + 2 O ₂	6.44		[49]
298.0	50034	3 CO + 1 H ₂ + 2 O ₂	6.44		[49]
298.0	54949	3 CO + 1 H ₂ + 2 O ₂	6.58		[49]
298.0	54949	3 CO + 1 H ₂ + 2 O ₂	4.88		[49]
298.0	54949	3 CO + 1 H ₂ + 2 O ₂	4.88		[49]
298.0	60067	3 CO + 1 H ₂ + 2 O ₂	4.38		[49]
298.0	60067	3 CO + 1 H ₂ + 2 O ₂	4.38		[49]
298.0	60067	3 CO + 1 H ₂ + 2 O ₂	4.38		[49]
293.0	20300	0.67 H ₂ + 0.33 O ₂	11.8		[63]
293.0	24600	0.67 H ₂ + 0.33 O ₂	5.8		[63]
293.0	30400	0.67 H ₂ + 0.33 O ₂	6.38		[63]
293.0	35000	0.67 H ₂ + 0.33 O ₂	5.33		[63]
293.0	40200	0.67 H ₂ + 0.33 O ₂	4.45		[63]
293.0	50300	0.67 H ₂ + 0.33 O ₂	2.94		[63]
293.0	60300	0.67 H ₂ + 0.33 O ₂	2.38		[63]
293.0	69300	0.67 H ₂ + 0.33 O ₂	1.99		[63]
293.0	86700	0.67 H ₂ + 0.33 O ₂	1.71		[63]
293.0	99700	0.67 H ₂ + 0.33 O ₂	1.39		[63]
293.0	125000	0.67 H ₂ + 0.33 O ₂	1.22		[63]
293.0	147000	0.67 H ₂ + 0.33 O ₂	0.98		[63]
293.0	172000	0.67 H ₂ + 0.33 O ₂	0.876		[63]
293.0	167000	0.67 H ₂ + 0.33 O ₂	0.796		[63]
293.0	192000	0.67 H ₂ + 0.33 O ₂	0.742		[63]
293.0	228000	0.67 H ₂ + 0.33 O ₂	0.645		[63]
293.0	297000	0.67 H ₂ + 0.33 O ₂	0.438		[63]
293.0	318000	0.67 H ₂ + 0.33 O ₂	0.438		[63]
293.0	366000	0.67 H ₂ + 0.33 O ₂	0.402		[63]
293.0	387000	0.67 H ₂ + 0.33 O ₂	0.375		[63]
293.0	433000	0.67 H ₂ + 0.33 O ₂	0.402		[63]
293.0	446000	0.67 H ₂ + 0.33 O ₂	0.449		[63]
293.0	491000	0.67 H ₂ + 0.33 O ₂	0.296		[63]
293.0	519000	0.67 H ₂ + 0.33 O ₂	0.3		[63]
293.0	512000	0.67 H ₂ + 0.33 O ₂	0.288		[63]
293.0	613000	0.67 H ₂ + 0.33 O ₂	0.212		[63]
293.0	614000	0.67 H ₂ + 0.33 O ₂	0.225		[63]
293.0	726000	0.67 H ₂ + 0.33 O ₂	0.209		[63]
293.0	716000	0.67 H ₂ + 0.33 O ₂	0.187		[63]
293.0	757000	0.67 H ₂ + 0.33 O ₂	0.185		[63]
293.0	746000	0.67 H ₂ + 0.33 O ₂	0.17		[63]
293.0	811000	0.67 H ₂ + 0.33 O ₂	0.159		[63]
293.0	895000	0.67 H ₂ + 0.33 O ₂	0.161		[63]
293.0	920000	0.67 H ₂ + 0.33 O ₂	0.142		[63]

T_1 [K]	P_1 [Pa]	Mixture (mole basis)	$\lambda_{\text{avg}}^{\text{max}} _{\text{min}}$ [mm]	Velocity [m/s]	Ref
293.0	1020000	0.67 H ₂ + 0.33 O ₂	0.144		[63]
293.0	1230000	0.67 H ₂ + 0.33 O ₂	0.109		[63]
298.0	7081	0.67 H ₂ + 0.33 O ₂	19		[50]
298.0	7851	0.67 H ₂ + 0.33 O ₂	16.3		[50]
298.0	9634	0.67 H ₂ + 0.33 O ₂	15.8		[50]
298.0	10545	0.67 H ₂ + 0.33 O ₂	15.6		[50]
298.0	11558	0.67 H ₂ + 0.33 O ₂	13.5		[50]
298.0	12987	0.67 H ₂ + 0.33 O ₂	9.43		[50]
298.0	12845	0.67 H ₂ + 0.33 O ₂	9.21		[50]
298.0	14881	0.67 H ₂ + 0.33 O ₂	9.12		[50]
298.0	16137	0.67 H ₂ + 0.33 O ₂	7.5		[50]
298.0	17667	0.67 H ₂ + 0.33 O ₂	7.08		[50]
298.0	19804	0.67 H ₂ + 0.33 O ₂	6.39		[50]
298.0	26358	0.67 H ₂ + 0.33 O ₂	4.58		[50]
298.0	26389	0.67 H ₂ + 0.33 O ₂	4.03		[50]
298.0	29235	0.67 H ₂ + 0.33 O ₂	3.77		[50]
298.0	31646	0.67 H ₂ + 0.33 O ₂	3.77		[50]
298.0	32771	0.67 H ₂ + 0.33 O ₂	3.4		[50]
298.0	32436	0.67 H ₂ + 0.33 O ₂	3.1		[50]
298.0	36316	0.67 H ₂ + 0.33 O ₂	3.1		[50]
298.0	36296	0.67 H ₂ + 0.33 O ₂	3.32		[50]
298.0	40206	0.67 H ₂ + 0.33 O ₂	3.14		[50]
298.0	43042	0.67 H ₂ + 0.33 O ₂	3.04		[50]
298.0	40236	0.67 H ₂ + 0.33 O ₂	2.9		[50]
298.0	38930	0.67 H ₂ + 0.33 O ₂	2.64		[50]
298.0	42627	0.67 H ₂ + 0.33 O ₂	2.55		[50]
298.0	44066	0.67 H ₂ + 0.33 O ₂	2.74		[50]
298.0	47155	0.67 H ₂ + 0.33 O ₂	2.8		[50]
298.0	49992	0.67 H ₂ + 0.33 O ₂	2.3		[50]
298.0	46213	0.67 H ₂ + 0.33 O ₂	2.15		[50]
298.0	48928	0.67 H ₂ + 0.33 O ₂	2.03		[50]
298.0	52392	0.67 H ₂ + 0.33 O ₂	1.92		[50]
373.0	101000	0.67 H ₂ + 0.33 O ₂	7		[51]
294.0	13400	1 H ₂ + 0.50 O ₂	10.8		[46]
294.0	18410	1 H ₂ + 0.50 O ₂	9.4		[46]
294.0	23440	1 H ₂ + 0.50 O ₂	8		[46]
294.0	26600	1 H ₂ + 0.50 O ₂	7.2		[46]
294.0	29220	1 H ₂ + 0.50 O ₂	6.4		[46]
294.0	31550	1 H ₂ + 0.50 O ₂	5.9		[46]
294.0	35000	1 H ₂ + 0.50 O ₂	5		[46]
293.0	5409	0.67 H ₂ + 0.33 O ₂	26.6		[52]
293.0	6655	0.67 H ₂ + 0.33 O ₂	25.2		[52]

T_1 [K]	P_1 [Pa]	Mixture (mole basis)	$\lambda_{\text{avg}}^{\text{max}} _{\text{min}}$ [mm]	Velocity [m/s]	Ref
293.0	7334	0.67 H ₂ + 0.33 O ₂	24.4		[52]
293.0	7932	0.67 H ₂ + 0.33 O ₂	24.6		[52]
293.0	9350	0.67 H ₂ + 0.33 O ₂	16.9		[52]
293.0	9938	0.67 H ₂ + 0.33 O ₂	13.9		[52]
293.0	10555	0.67 H ₂ + 0.33 O ₂	13.3		[52]
293.0	11923	0.67 H ₂ + 0.33 O ₂	12.4		[52]
293.0	13230	0.67 H ₂ + 0.33 O ₂	9.31		[52]
293.0	13230	0.67 H ₂ + 0.33 O ₂	8.64		[52]
293.0	15398	0.67 H ₂ + 0.33 O ₂	7.37		[52]
293.0	16360	0.67 H ₂ + 0.33 O ₂	7.23		[52]
293.0	22995	0.67 H ₂ + 0.33 O ₂	4.76		[52]
293.0	22995	0.67 H ₂ + 0.33 O ₂	4.4		[52]
293.0	30775	0.67 H ₂ + 0.33 O ₂	3.77		[52]
293.0	29863	0.67 H ₂ + 0.33 O ₂	3.33		[52]
293.0	33125	0.67 H ₂ + 0.33 O ₂	2.82		[52]
293.0	4448	0.67 H ₂ + 0.33 O ₂	49.5		[53]
293.0	6966	0.67 H ₂ + 0.33 O ₂	48.4		[53]
293.0	11326	0.67 H ₂ + 0.33 O ₂	43.4		[53]
293.0	16607	0.67 H ₂ + 0.33 O ₂	20.3		[53]
293.0	26652	0.67 H ₂ + 0.33 O ₂	8.29		[53]
293.0	39441	0.67 H ₂ + 0.33 O ₂	6.87		[53]
293.0	39530	0.67 H ₂ + 0.33 O ₂	5.13		[53]
293.0	52124	0.67 H ₂ + 0.33 O ₂	7.54		[53]
293.0	52591	0.67 H ₂ + 0.33 O ₂	6.43		[53]
293.0	67059	0.67 H ₂ + 0.33 O ₂	4.27		[53]
293.0	101629	0.67 H ₂ + 0.33 O ₂	2.08		[53]
293.0	118040	0.67 H ₂ + 0.33 O ₂	2.03		[53]
293.0	28420	0.67 H ₂ + 0.33 O ₂	7		[54]
293.0	28450	0.67 H ₂ + 0.33 O ₂	6.03		[54]
293.0	80320	0.67 H ₂ + 0.33 O ₂	2.03		[54]
293.0	80420	0.67 H ₂ + 0.33 O ₂	1.77		[54]
293.0	47480	0.67 H ₂ + 0.33 O ₂	3.48		[54]
293.0	47550	0.67 H ₂ + 0.33 O ₂	3		[54]
293.0	98870	0.67 H ₂ + 0.33 O ₂	1.6		[54]
293.0	99000	0.67 H ₂ + 0.33 O ₂	1.39		[54]
293.0	70110	0.67 H ₂ + 0.33 O ₂	1.8		[55]
293.0	6625	0.33 CH ₄ + 0.67 O ₂	85.7		[56]
293.0	7972	0.33 CH ₄ + 0.67 O ₂	70.6		[56]
293.0	9340	0.33 CH ₄ + 0.67 O ₂	55.9		[56]
293.0	12034	0.33 CH ₄ + 0.67 O ₂	40.5		[56]
293.0	13443	0.33 CH ₄ + 0.67 O ₂	35.1		[56]
293.0	615691	0.33 CH ₄ + 0.67 O ₂	0.38		[63]

T_1 [K]	P_1 [Pa]	Mixture (mole basis)	$\lambda_{\text{avg}}^{\text{min}}$ [mm]	Velocity [m/s]	Ref
293.0	598876	0.33 CH ₄ + 0.67 O ₂	0.407		[63]
293.0	405352	0.33 CH ₄ + 0.67 O ₂	0.728		[63]
293.0	352149	0.33 CH ₄ + 0.67 O ₂	0.739		[63]
293.0	305804	0.33 CH ₄ + 0.67 O ₂	0.681		[63]
293.0	306412	0.33 CH ₄ + 0.67 O ₂	0.936		[63]
293.0	207007	0.33 CH ₄ + 0.67 O ₂	1.24		[63]
293.0	156691	0.33 CH ₄ + 0.67 O ₂	1.8		[63]
293.0	152254	0.33 CH ₄ + 0.67 O ₂	1.95		[63]
293.0	101300	0.33 CH ₄ + 0.67 O ₂	2.38		[63]
293.0	101300	0.33 CH ₄ + 0.67 O ₂	2.96		[63]
293.0	81081	0.33 CH ₄ + 0.67 O ₂	2.93		[63]
293.0	60415	0.33 CH ₄ + 0.67 O ₂	3.51		[63]
293.0	40915	0.33 CH ₄ + 0.67 O ₂	6.74		[63]
293.0	37481	0.33 CH ₄ + 0.67 O ₂	12.6		[63]
293.0	6757	0.33 CH ₄ + 0.67 O ₂	95.9		[57]
293.0	8155	0.33 CH ₄ + 0.67 O ₂	75.8		[57]
293.0	9340	0.33 CH ₄ + 0.67 O ₂	53.9		[57]
293.0	10687	0.33 CH ₄ + 0.67 O ₂	44.2		[57]
293.0	12217	0.33 CH ₄ + 0.67 O ₂	40.4		[57]
293.0	13605	0.33 CH ₄ + 0.67 O ₂	35.9		[57]
294.0	15340	1 CH ₄ + 2 O ₂	39.9		[46]
294.0	21220	1 CH ₄ + 2 O ₂	29.8		[46]
294.0	19640	1 CH ₄ + 2 O ₂	31.9		[46]
294.0	26580	1 CH ₄ + 2 O ₂	24.9		[46]
294.0	36070	1 CH ₄ + 2 O ₂	14.9		[46]
300.0	100000	2.33 CH ₄ + 1 H ₂ + 5.17 O ₂	5.3		[47]
300.0	100000	1 CH ₄ + 2 O ₂	4.3		[47]
300.0	100000	1 CH ₄ + 2 O ₂	4.8		[47]
300.0	200000	1 CH ₄ + 2 O ₂	2.8		[47]
300.0	200000	1 CH ₄ + 2 O ₂	2.5		[47]
300.0	200000	1 CH ₄ + 2 O ₂	2.2		[47]
300.0	300000	1 CH ₄ + 2 O ₂	2		[47]
300.0	300000	1 CH ₄ + 2 O ₂	1.8		[47]
300.0	300000	1 CH ₄ + 2 O ₂	1.6		[47]

Appendix B

RMC Detonation Laboratory

The development of the RMC Detonation Laboratory comprised of initial procurement, engineering design, construction, and testing before it could be used to run experiments.

B.1 Detonation Channel and Frame

The first engineering design work comprised of developing the frame that would support the detonation channel, and the caddies that would carry the channel on the frame. Force and stress analyses were calculated analytically for the loading conditions expected. A 3-view model of the detonation channel section is shown in Fig. B.1. The complete detonation channel consists of five of these sections one of which is planned to have a translucent window section to be able to observe the detonation.

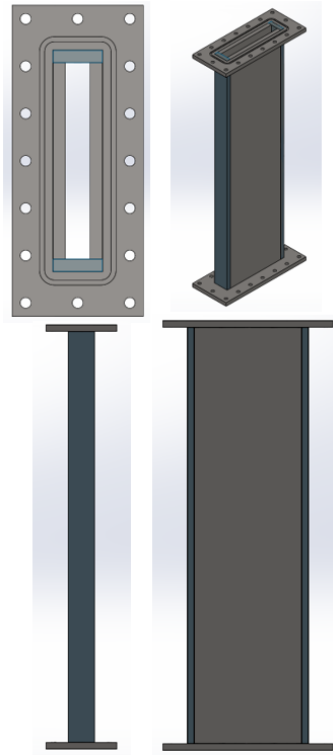


Figure B.1 – CAD model of detonation channel at RMC

To support the detonation channel, a frame was required to be constructed. The key considerations included a simple and cost-effective design which was sturdy, able to support the expected loadings, and easy to adjust and move around as experiments are conducted. The design went through several iterations before the final frame design was selected and materials were procured. The frame was designed to be modular so that each section was independent and could be interchanged. This was due to constraints in machining and transport. As well, the modular design allows easier replacement should sections become damaged. A CAD model was created for the frame sections in Fig. B.2. Calculations were done using concepts from Shigley's Mechanical Engineering Design 9th Edition [105].

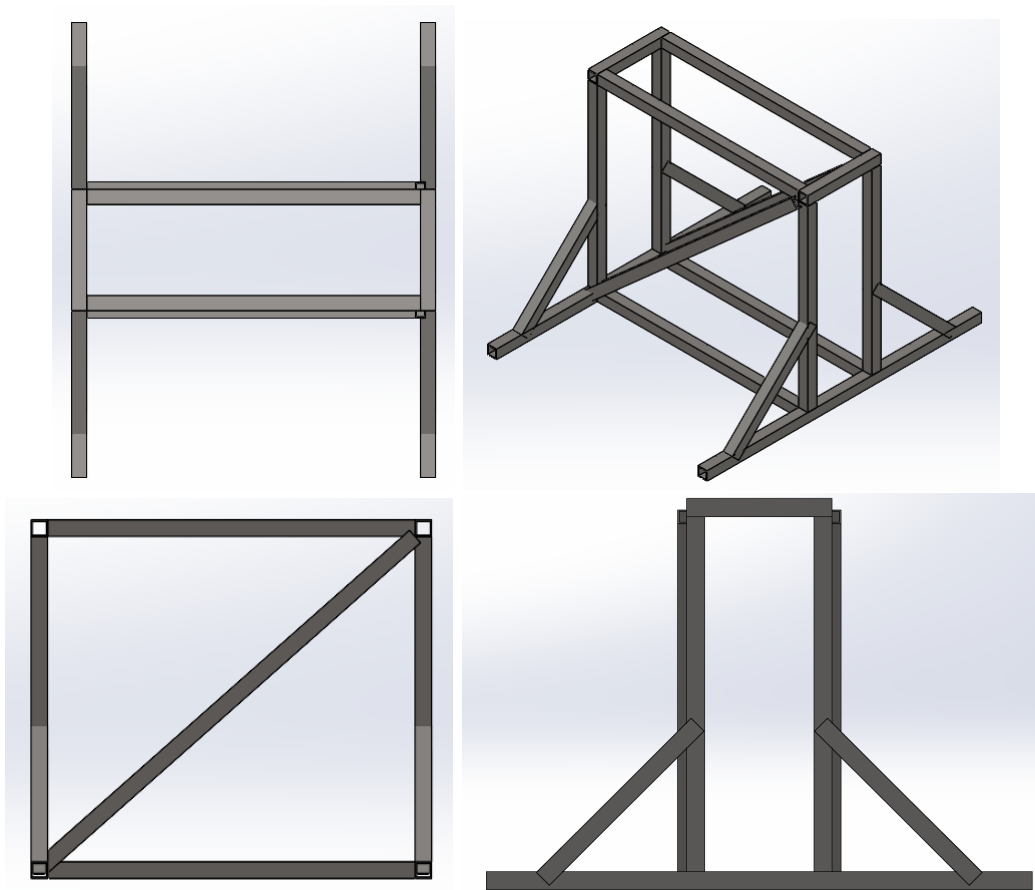


Figure B.2 – CAD model of frame section for detonation channel

To support the channel on the frame, a caddy was required. The goal of the caddy is to be able to roll the detonation channel on the frame and to make adjustments to the apparatus. Therefore, the caddy was required to be sturdy, durable, support the loading expected, and allow access to the instrumentation plugs in the detonation channel. After several iterations, analysis showed that two caddies per section of detonation channel provided the best weight distribution and preferable stress characteristics while keeping costs low. Threaded steel track rollers were selected since the pre-threading would simplify manufacturing and the steel provided high loading in the normal and transverse directions. The caddy design prioritized off-the-shelf parts to reduce the pressure on the manufacturing. As a result, only the threaded bars, handles, and spacer blocks require post-procurement machining, while the threaded rods, rollers, washers, and nuts are purchased off-the-shelf. The CAD model for the caddy is shown in Fig. B.3.

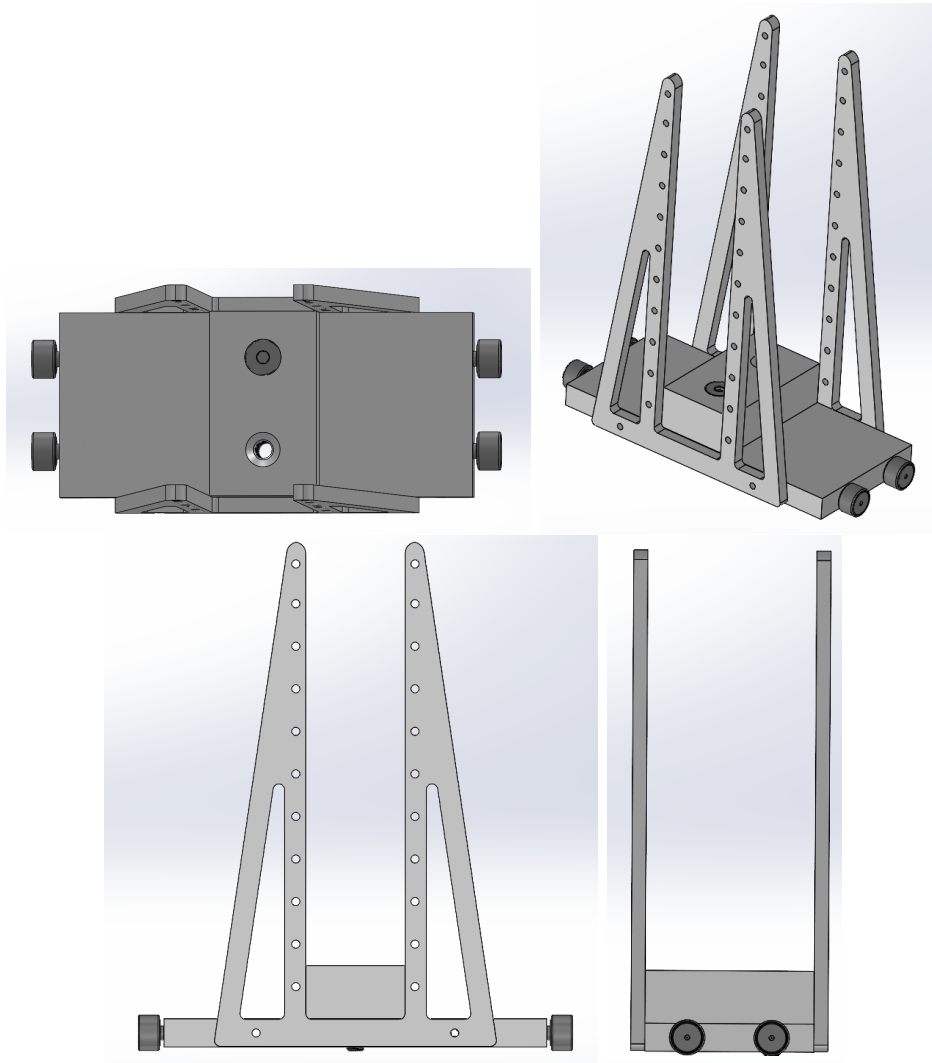


Figure B.3 – CAD model of caddy for detonation channel

The limit loading of the channel was assessed by considering the reflected shock CJ pressure compared with the yield strength of the steel channel. The limit pressure of 3 MPa, based on SolidWorks finite element analysis (FEA) (Fig. B.4), can be achieved with initial mixtures and pressures of $2\text{H}_2 + \text{O}_2$ at 70 kPa, $\text{CH}_4 + 2\text{O}_2$ at 40 kPa, or $2\text{C}_2\text{H}_2 + 5\text{O}_2$ at 40 kPa as examples. The failure mode is predicted to be concentrated at the welded joints. This analysis showed that the channel should be able to support the desired experiments without failure, but ongoing observation should be conducted to ensure the channel is not failing in unforeseen modes.

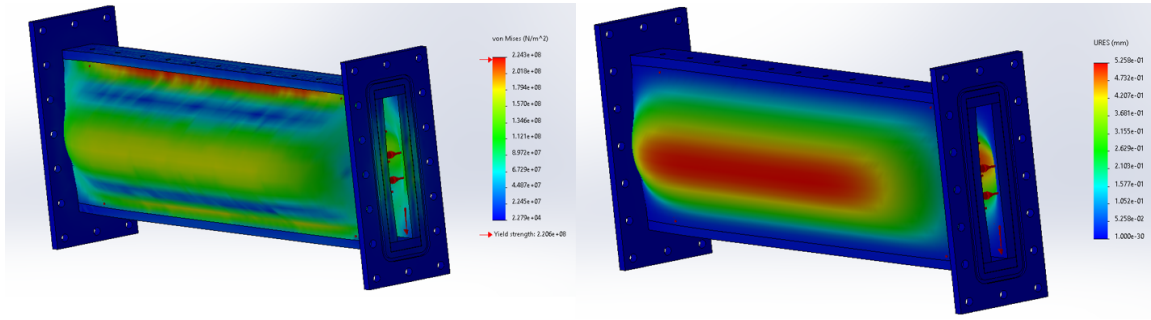


Figure B.4 – Solidworks FEA simulation of RMC detonation channel section with maximum internal loading representing a reflected CJ shock pressure of 3 MPa.

B.2 Mixing Panel and Gas Handling

The mixing panel was also designed specifically for this laboratory with safety in mind featuring high-pressure rated Swagelok tubing and low pipe volumes to prevent the build-up of detonable gases while mixing. The panel is made from a steel plate with cutouts for the valves and the tubing running behind. The schematic is shown in Fig. B.5. The panel is rated to a maximum pressure of 3000 psi (20.6 MPa) [106]. The pure gases are connected via flexible tubing to the left side 1/4" valves. The mixed bottles are stamped to 4500 psi (31.0 MPa) maximum pressure and permanently connected via rigid Swagelok 1/4" OD tubing to the panel on the right side valves. The panel also has ports for Omega pressure transducers and a valve to vent to the room for emergencies. A steel braided 1/2" tube rated to 1800 psi (12.4 MPa) [106] connects the panel to the channel. The vacuum pump is connected via 1/2" reinforced plastic vacuum tubing to the panel using ISO-KF fittings. In operation, one mixed bottle is kept at vacuum to allow an emergency reservoir for detonable gases or combustion products to flow if unable to be exhausted safely. For each mixture tested, the gases are mixed via the diffusive process. In this case, the gases mix due to the random motion of their molecules, following Fick's laws of diffusion. No external force or turbulence is applied, so the mixing occurs slowly as molecules move from regions of higher concentration to lower concentration until equilibrium is reached. For gases with different densities, gravitational effects might slow the mixing process, but eventually, diffusion results in a uniform mixture which is why 24 hours are used to allow the process to take place.

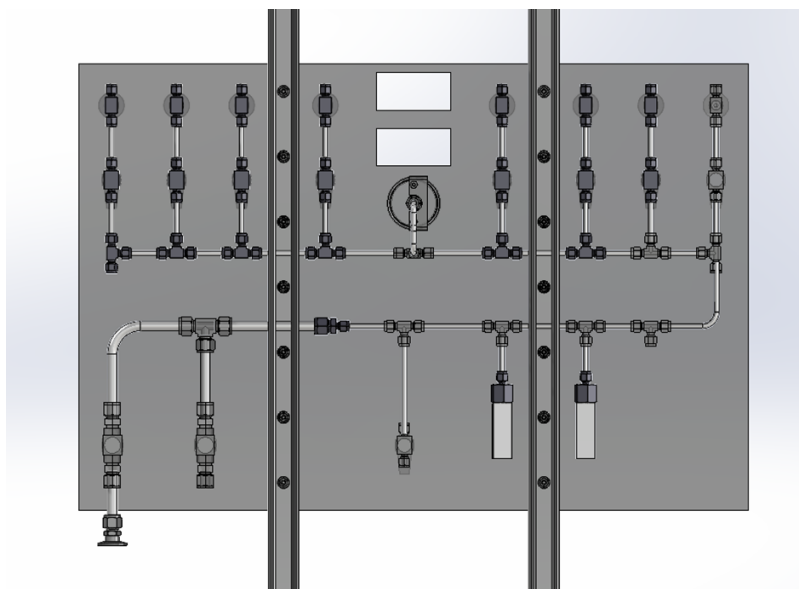


Figure B.5 – Mixing panel schematic for RMC detonation channel

Due to the toxic nature of some gases proposed to work with at the RMC lab, an exhaust system had to be designed. Considerations were made for carbon monoxide impact on personnel, and the flammability limit of highly reactive gases. These engineering considerations were communicated to technicians who installed the infrastructure in the laboratory. First, carbon monoxide, a deadly colourless, odourless, tasteless gas, is a byproduct of incomplete combustion and may be released during experiments. Calculations were performed assuming a conservative estimate where a low pressure (10 kPa) test with stoichiometric carbon monoxide and air was aborted. This would result in 30% by volume of CO being released into the room, which equates to only 24 g or in a 100 m³ room, 0.24 ppm, well within published limits. A household detector alerts the occupants when CO exceeds 11 ppm. Furnaces exhaust an average of 6 ppm in their exhaust [107], and the National Fuel Gas Code allows up to 400 ppm air free CO for furnaces and clothes dryers [108]. A similar study was performed for NO_x which is produced when reacting fuels with air. Simulations show less than 3% of NO in detonation products and trace amounts of other NO_x products; these are well within limits for Canadian and US emission code [109], [110]. Despite these gases being at too low concentrations to inflict harm, outdoor venting was installed in accordance with Ontario Building Code 2024 §9.32.3.13 [111]. The gas exhaust blower was sized such that outside air would dilute an explosive mixture to below its explosive limit. The most reactive fuel that would be tested is stoichiometric acetylene-oxygen with an explosive limit of 2.5% by volume of air. Considering the Edwards 40 vacuum pump extraction of 25 ft³/min, it requires a blower fan with volumetric flow rate of at least 300 ft³/min. Therefore, a suitable blower fan was found which was also rated for flammable gases, vapours, and protects against National Electric Code Class I and II explosions [112]. Procedures require that operators shall use the exhaust fan when running tests so that the vacuum products are exhausted outside.

B.3 Procedure Checklists

In establishing the new laboratory, routine and emergency procedures had to be developed that promoted efficiency of the operation while maximizing safety for personnel and assets. Additionally, all personnel working in the laboratory shall have completed WH-MIS and lab-specific online training and be given an orientation by a qualified member. The complete normal operating procedures as well as abnormal occurrence and critical emergency checklists follow. The checklists were based on risk management and procedure principles from aircrew flight checklists, and safety principles and cultures from adopted from the Royal Canadian Air Force Flight Safety program [113]. The procedures contain consistent wording for each action and include notes, cautions and warnings that guide users. Personal protective equipment is paramount to human safety and is featured in all procedures where required. These checklists, created by the author, can be disseminated to future employees of the lab to ensure safe practices are continued.

NORMAL PROCEDURES

LAB DAY START

1. EXHAUST FAN – ON and CONFIRM
2. VACUUM PUMPS – ON
3. CALCULATE DETONATION PRESSURES, MIXTURES

NOTE

Start state shall have all mixing panel, gas bottle, and channel valves closed. All channel and panel lines at atmospheric pressure.

PREPARING MIXTURE

1. PANEL VAC VALVE – OPEN, CHANNEL-PANEL LINE – OPEN TO PANEL ONLY standby for vacuum reading on digital gauges
2. CHANNEL-PANEL LINE – CLOSE
3. OPEN panel line of desired mixing bottle to VACUUM LINE and BOTTLE
4. MIXED BOTTLE – OPEN

WARNING

To preclude inadvertent addition of gas to channel, ensure the channel-to-panel line is closed on both ends.

5. PANEL VAC VALVE – CLOSED
6. Determine partial pressures of pure gases required for mixture
7. PURE GAS ball valve – OPEN, modulate NEEDLE VALVE and MONITOR PRESSURE gauge
8. PURE GAS valves – CLOSED
9. MIXED BOTTLE – CLOSED
10. PANEL VAC VALVE – OPEN
11. BOTTLE-PANEL LINE – OPEN
12. PANEL VAC VALVE – CLOSED

13. Repeat steps 5-11 for all subsequent pure gases.

CAUTION

If undesired excess gas is added, perform EXCESS GAS

14. ALL VALVES – CLOSED
15. MIXED GAS BOTTLE – CLOSED
16. STANDBY – 24 HRS for mixing

CONDUCTING TEST

1. PANEL VAC VALVE – OPEN
2. CHANNEL VAC VALVE – OPEN
3. CHANNEL-PANEL line – OPEN
4. STANDBY – vacuum reading on pressure gauges
5. Determine desired pressure of mixed gas for test
6. ALL VAC VALVES – CLOSED
7. PPE – DON
8. MIXED GAS BOTTLE – OPEN
9. MIXED GAS BALL valve – OPEN
10. MIXED GAS NEEDLE valve – OPEN slowly and CLOSE when desired pressure reached.
11. MIXED GAS BALL valve – CLOSED
12. MIXED GAS BOTTLE – CLOSED
13. CHANNEL-PANEL LINE – CLOSED
14. Conduct PANEL EXHAUST
15. DATA RECORDER – READY
16. TRIGGER MODE – SET as needed

WARNING

Ensure all personnel are wearing PPE and positioned behind safety shields. Confirm panel and channel valves are closed.

17. INITIATOR – ON
18. INITIATOR – TRIGGER
19. INITIATOR – OFF
20. PPE – DOFF

PANEL EXHAUST

1. EXHAUST FAN – CONFIRM ON
2. CHANNEL-PANEL line – OPEN TO PANEL ONLY
3. PANEL VAC VALVE – OPEN
4. ALL LINES TO MIX BOTTLES – OPEN
5. STANDBY – vacuum reading on pressure gauges
6. CHANNEL-PANEL line – CLOSED
7. ALL VAC VALVES – CLOSED

CHANNEL EXHAUST

1. EXHAUST FAN – CONFIRM ON
2. CHANNEL VAC VALVE – OPEN
3. CHANNEL-PANEL line – OPEN
4. STANDBY – vacuum reading on pressure gauges
5. ALL VAC VALVES – CLOSED
6. CHANNEL-PANEL line – CLOSED

REPLACE SOOT FOIL

CAUTION

Ensure channel is at atmospheric pressure before opening. Do not add air to channel if undetonated mixture remains in channel – perform CHANNEL EXHAUST.

1. CHANNEL-PANEL line – OPEN
2. AIR INTAKE – OPEN
3. PRESSURE – standby for 1 atm
4. CHANNEL-PANEL line – CLOSE
5. AIR INTAKE – CLOSE
6. PPE – DON
7. Channel section BOLTS – REMOVE
8. Slide section to release foil
9. TEST FOIL – REMOVE carefully and preserve
10. NEW FOIL – PLACE
11. Channel section BOLTS – REPLACE and TIGHTEN

12. Conduct CHANNEL EXHAUST

If vacuum is leaking: perform CHANNEL VACUUM SEAL

PREPARE SOOT FOIL

CAUTION

This process shall be carried out in well-ventilated areas only. Use the fume hood in CHEM lab or outdoors.

1. ALUMINUM OR PLASTIC sheets – CUT to desired size
2. FUME HOOD – ON
3. OIL LAMP/BUNSEN BURNER – ADD KEROSENE if required

CAUTION

In event of spill, clean with cloth. After pouring kerosene, replace cap and place away from workspace.

4. BURNER – LIGHT and control flame to produce soot
5. GLOVES – DON
6. FOIL – COAT with soot by moving slowly and evenly over the flame
7. BURNER – EXTINGUISH by removing fuel or air source
8. FUME HOOD – OFF

ABNORMAL OCCURRENCES

EXCESS GAS

If gas is added that exceeds the amount desired while MIXING or CONDUCTING TEST:

1. ALL VALVES – CLOSED

If excess gas in mixing bottles:

2. MIXED GAS BOTTLE – OPEN
3. Conduct PANEL EXHAUST

If excess gas in detonation channel:

2. Conduct CHANNEL EXHAUST

CHANNEL VACUUM SEAL

If the channel does not hold vacuum after opening/closing:

1. SUSPECT SECTION – OPEN
2. FILE faces until smooth
3. CLEAN face with soap and water, DRY
4. O-RING – apply vacuum GREASE and RESEAT
5. Channel section BOLTS – REPLACE and TIGHTEN in star pattern
6. CHANNEL VAC pump – ON, CHANNEL VAC VALVE – OPEN
7. CHANNEL-PANEL line – OPEN
8. STANDBY – vacuum reading on pressure gauges

CRITICAL EMERGENCIES

LAB EVACUATION

1. LAB – EVACUATE
2. ALARM – SOUND
3. YELL “FIRE FIRE FIRE”
4. Assist members to evacuate as needed
5. Walk to MUSTER POINT
6. Meet fire crew on site and advise of any potentially hazardous gases

FIRE

If able prior to evacuating laboratory:

1. GAS VALVES – CLOSE
2. VAC PUMPS – ON
3. EXHAUST FAN – ON
4. EXHAUST FAN VALVE – OPEN
5. IGNITION SOURCES – OFF
6. FIRE EXTINGUISHER – USE as needed

All times perform LAB EVACUATION

DANGEROUS GAS LEAK

Upon hearing CO alarm or detecting leak immediately:

1. SCBA – DON if available, else hold breath
2. GAS VALVES – CLOSE
3. EXHAUST FAN – ON
4. VAC PUMPS – ON
5. VAC PUMP VALVES – OPEN
6. IGNITION SOURCES – OFF
7. Perform LAB EVACUATION

FIRE IN FUME HOOD

1. FUME HOOD – ENSURE ON
2. FLAME – SMOTHER if possible with metal bucket
3. GAS SOURCES – OFF/REMOVE
4. SLIDING GLASS – CLOSE
5. FIRE EXTINGUISHER – USE as needed

If uncontrolled: perform LAB EVACUATION